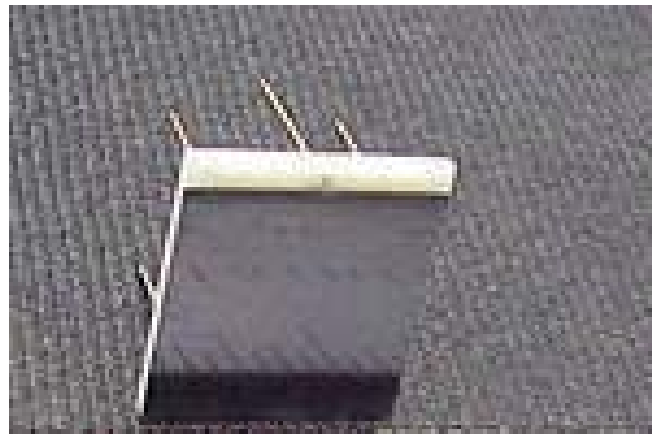
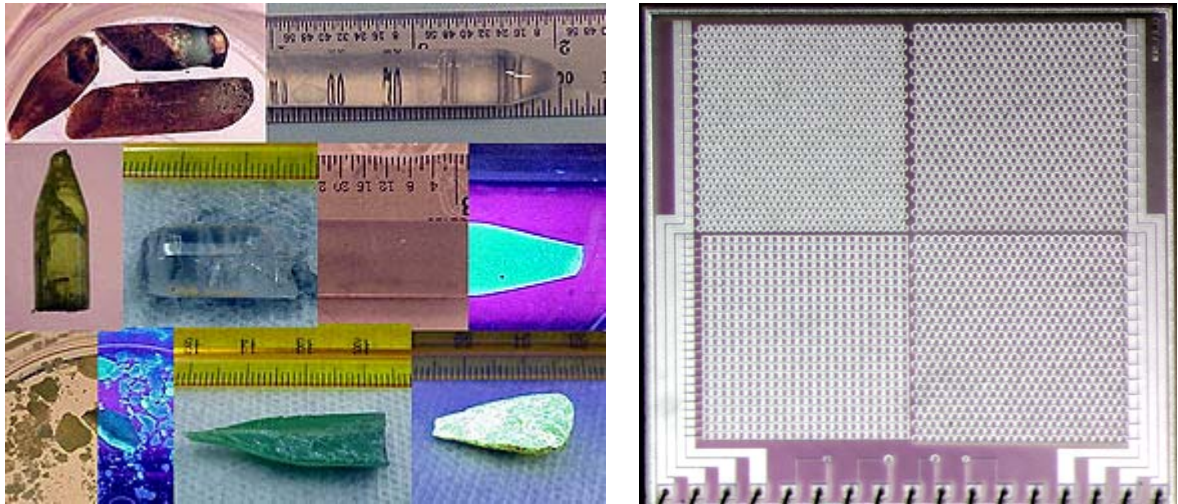


New Scintillation Detectors for PET



Kanai S. Shah

New Scintillation Detectors for PET

Kanai Subodhbhai SHAH

Top left – photographs of RMD’s various new scintillation crystals;
Top right – photograph of a chip with four different designs of RMD’s silicon photomultipliers
Bottom – photograph of RMD’s position sensitive avalanche photodiode

New Scintillation Detectors for PET

Proefschrift

ter verkrijging van de graad van doctor
aan de Technische Universiteit Delft,
op gezag van de Rector Magnificus Prof.ir. K.C.A.M. Luyben
voorzitter van het College voor Promoties,
in het openbaar te verdedigen op dinsdag 19 oktober 2010 om 10:00 uur

door

Kanai Subodhbhai SHAH

Master of Science in Chemical Engineering van de University of Lowell, Massachusetts

geboren te Ahmedabad, India

Dit proefschrift is goedgekeurd door de promotoren:

Prof.dr.ir. C. W.E. van Eijk
Prof. dr. P. Dorenbos

Samenstelling promotiecommissie:

Rector Magnificus	Voorzitter
Prof.dr.ir. C.W.E. van Eijk	Technische Universiteit Delft, promotor
Prof.dr. P. Dorenbos	Technische Universiteit Delft, promotor
Prof.dr. E. Charbon	Technische Universiteit Delft
Prof.dr. P.A. Rodnyi	St. Petersburg State Techn. University
Prof.dr. W.W. Moses	University of California at Berkeley
Prof.dr. H. Löhner	Rijksuniversiteit Groningen
Prof.dr. C.R. Ronda	Universiteit Utrecht
Prof.dr F.M. Mulder	Technische Universiteit Delft, reservelid

© Copyright 2010 by Kanai S. Shah

All rights reserved. No part of this publication may be reproduced, stored in a retrieval system, or transmitted, in any form or by any means, electronic, mechanical, photocopying, recording or otherwise, without the prior permission of the publishers.

Printed in The Netherlands.

ISBN 978-1-4507-3824-8

Thieme Media Services

Postbus 30, 2600 AA Delft

Telefoon: 015 – 215 33 15

Fax: 015 – 212 06 27

To

My Parents & Mashi

Table of Contents

Chapter 1: Introduction	11
1.1 Overview of Scintillators for PET	11
1.2 Overview of Photodetectors for PET:.....	13
1.3 Some Trends in PET Instrumentation.....	13
1.4 Organization of this Thesis	16
Chapter 2: Experimental Methods for Scintillation Studies	19
2.1 Overview.....	19
2.2 Crystal Growth Method:.....	19
2.3 Radioluminescence Measurements	20
2.4 Light Yield and Energy Resolution Measurements.....	21
2.5 Decay Time Measurements.....	22
2.6 Coincidence Timing Resolution Measurements.....	23
2.7 References.....	24
Chapter 3: Cerium Doped Lanthanum Bromide Scintillators	25
3.1 Overview.....	25
3.2 Introduction:	25
3.3 Preparation of LaBr₃:Ce Crystals.....	26
3.4 Scintillation Properties of LaBr₃:Ce.....	27
3.4.1 Light Output and Energy Resolution	27
3.4.2 Emission Spectrum	28
3.4.3 Decay Time.....	28
3.4.4 Coincidence Timing Resolution	29
3.4.5 Proportionality of Response.....	30
3.4.6 Exploration of Scintillation Properties of LaBr ₃ with higher Ce ³⁺ Concentration	31
3.5 Energy Resolution of LaBr₃:Ce.....	33
3.5.1. Energy Resolution Results.....	33
3.5.2. Analysis of 662 keV Energy Resolution:.....	35
3.6 Summary	37
3.7 Current Status of LaBr₃:Ce.....	37
3.8 References.....	38
Chapter 4: Cerium Bromide Scintillators	41
4.1 Overview.....	41

4.2. Introduction	41
4.3. Crystal Growth of CeBr₃	41
4.4. Scintillation Properties of CeBr₃.....	42
4.4.1 Light Output and Energy Resolution	42
4.4.2 Emission Spectrum	43
4.4.3 Decay Time.....	43
4.4.4 Coincidence Timing Resolution	44
4.4.5 Proportionality of Response.....	45
4.5 Energy Resolution of Larger CeBr₃ Crystals.....	46
4.6 Timing Resolution of CeBr₃ Crystals with Energy Gating.....	48
4.7 Study of Other Cerium Halides.....	49
4.7.1 Emission Spectra	49
4.7.2. Decay Time Spectra.....	50
4.7.3. Light Output Measurements	50
4.8. Summary	52
4.9. Current Status.....	53
Chapter 5: Cerium Doped Lutetium Iodide Scintillators	55
5.1 Overview.....	55
5.2. Introduction	55
5.3 Physical Properties and Crystal Growth.....	55
5.4 Scintillation Properties of LuI₃:Ce.....	56
5.4.1. Light Output and Energy Resolution	56
5.4.2. Emission Spectrum	57
5.4.3. Decay Time.....	57
5.4.4. Coincidence Timing Resolution	58
5.4.5. Proportionality of Response.....	59
5.4.6. Effect of Ce ³⁺ Concentration on Scintillation Properties of LuI ₃ :Ce	60
5.6 References:	62
Chapter 6: Elpasolite and Alkaline Earth Halide Scintillators for SPECT.....	63
6.1 Introduction	63
6.2. Detector Requirements for Single Photon Imaging.....	64
6.3. Scintillators for Single Photon Imaging.....	64
6.4 Ce³⁺ doped Elpasolite Scintillators.....	65
6.4.1 Overview	65
6.4.2 Cs ₂ LiLaBr ₆ :Ce (CLLB) Scintillators	68
6.4.2.1. Overview.....	68
6.4.2.2. Scintillation Properties of CLLB Crystals	68
Emission Spectra	68
Decay Time Spectra	69
Light Output.....	70
6.4.2.3. Gamma Ray Detection with CLLB:Ce Scintillators.....	71
Room Temperature CLLB:Ce Energy Resolution Measurements.....	71

Analysis of Energy Resolution of CLLB:Ce Scintillators	72
Coincidence Timing Resolution	73
6.5 Eu^{2+} doped Alkaline Earth Halide Scintillators.....	74
6.5.2 Evaluation of $\text{SrI}_2\text{:Eu}$	75
6.5.2.1. Crystal Growth Aspects	75
6.5.2.2. Scintillation Properties of $\text{SrI}_2\text{:Eu}^{2+}$	75
Emission Spectra	76
Decay Time Spectra	76
3. Light Output Measurements.....	77
Gamma-Ray Energy Resolution.....	78
Proportionality Studies	78
6.5.3. Summary of Scintillation Properties of Other Alkaline Earth Halides.....	79
6.6 References.....	79
Chapter 7: Position Sensitive Avalanche Photodiodes.....	83
7.1 Overview.....	83
7.2 Introduction	83
7.3 Position Sensitive Avalanche Photodiodes	83
7.3.1 Design and Fabrication	83
7.3.2 Operational Scheme for Position Sensing and Energy and Timing Resolution of PSAPD	85
7.3.3 Position Sensing Capabilities.....	86
7.3.4 Simulation Studies	89
7.4 Summary	91
7.5 References.....	91
Chapter 8: Position Sensitive APDs for Small Animal PET.....	93
8.1 Overview.....	93
8.2 Introduction	93
8.3 Position Sensitive Avalanche Photodiodes	94
8.4 Evaluation of PSAPD-LSO PET Detector Modules.....	95
8.4.1 Energy Resolution Measurements	95
8.4.2 Timing Resolution Studies.....	96
8.4.3 Flood Histogram Studies	96
8.4.4 Depth of Interaction Measurements.....	97
8.5 Summary	99
8.6 Current Status: Examples of Small Animal PET Scanners Built with PSAPDs.....	99
8.6.1 MRI Compatible PET Scanner	100
8.6.2 Small Animal PET System with Depth-Encoding Detectors.....	100
8.7 References.....	101
Chapter 9: Solid-State Photomultipliers as Photodetectors for PET.....	105
9.1. Introduction	105
9.2. Layout and fabrication of prototype SSPMs	107
9.3 Basic SSPM Characterization.....	108

9.4. Evaluation of 3x3 mm² SSPMs with LSO/LYSO Crystals for PET	112
Energy Resolution Studies.....	112
Timing Resolution Studies:	113
Depth of Interaction Studies:	114
9.5. Second Generation SSPMs	116
9.6. Study of Position Sensitive SSPMs (PS-SSPMs).....	118
9.7. Micro-Pixel Level Position Sensitive SSPMs	119
9.8. Conclusions.....	121
9.9. References.....	121
Chapter 10: Conclusions and Future Trends	123
Chapter 11: Summary.....	125
Hoofdstuk 11: Samenvatting	129
Acknowledgements.....	133
Curriculum Vitae	135
Selected Recent Publications	135
Recent Presentations	136
Patents.....	137

CHAPTER 1: INTRODUCTION

1.1 OVERVIEW OF SCINTILLATORS FOR PET

Scintillation spectrometers consisting of inorganic scintillation crystals coupled to appropriate optical detectors are one of the most widely used classes of detectors for gamma-ray spectroscopy [Knoll, Kleinknecht, Rodnyi]. An incoming gamma-ray when stopped inside a scintillation crystal deposits its energy within the crystal, and an optical pulse is produced by the scintillator, the amplitude of which is proportional to the energy deposited in the scintillation crystal. This optical pulse emitted by the scintillator can then be detected by optical detectors such as photomultiplier tubes or silicon photodiodes to provide an electronic charge pulse that can be processed with standard nuclear pulse processing electronics. Such scintillation spectrometers are widely used in a number of important applications including nuclear and particle physics research, nuclear non-proliferation monitoring, geophysical exploration, astronomy, non destructive evaluation, material science studies and medical imaging.

In this thesis, an investigation of some new components for gamma-ray scintillation spectroscopy (both scintillators as well as photodetectors) is presented. While the new scintillators and photodetectors discussed in this thesis can be applied to many of the applications mentioned above, the primary focus of this thesis is on the impact of these new detectors on Positron Emission Tomography (PET), a powerful medical imaging modality. Some discussion of new scintillators for single photon emission computed tomography (SPECT) is also included. This thesis is based on the research performed by the author under employment at Radiation Monitoring Devices, Inc. (RMD, Inc., Watertown, MA, USA).

Positron Emission Tomography (PET) is a functional, noninvasive medical imaging technique that provides an image of the distribution of a positron emitting radio-pharmaceutical in the body [Bushberg, Cherry 03]. During PET imaging, a positron emitted by an injected radio-pharmaceutical undergoes annihilation with an electron and this process produces two 511 keV gamma-rays that travel approximately 180 ° from each other. Near-simultaneous detection of these two 511 keV gamma-rays with detectors placed opposite each other constitutes the signal generation process for PET. The availability of short lived positron-emitting isotopes of carbon (^{11}C), nitrogen (^{13}N), oxygen (^{15}O) and especially fluorine (^{18}F) allows most compounds of biological interest to be labeled in trace amounts and introduced into the body for *in vivo* imaging with PET. The distribution of the tracer is imaged dynamically, allowing the rates of biological processes to be calculated using appropriate mathematical models. PET has emerged as an important imaging modality for both clinical diagnosis and medical research [Phelps]. In combination with X-ray computed tomography (CT), PET has been found to be particularly effective in diagnosis as well as treatment of cancer [Townsend].

In addition to its use in clinical imaging studies, the role of PET in imaging of small animals (such as mice and rats) has also been noteworthy [Cherry 01]. PET imaging of small animals is providing better understanding of diseases through development of human disease models in mice and rats. Furthermore, small animal PET imaging has the potential to be very useful in pharmaceutical research and development. The main advantage of PET (unlike autoradiography) in small animal studies is that it provides functional information in a non-

invasive manner, which allows the same animal to be studied repeatedly, a desirable situation in designing longitudinal studies.

For existing PET systems (clinical as well as preclinical), gamma-ray detectors are arranged in a ring configuration to conduct imaging studies. In most existing commercial scanners for clinical and preclinical PET imaging, inorganic scintillators coupled to photomultipliers are used as detectors. Important requirements for the scintillation crystals used in PET systems include:

- fast response,
- high sensitivity,
- high light output,
- high energy resolution,
- high timing resolution, and
- low cost.

High energy resolution is important because it allows rejection of scattered events. High timing resolution is important because it allows rejection of random events. Furthermore, if fast enough scintillators become available, time-of-flight (TOF) information could be utilized to obtain better localization compared to conventional PET. Such localization in TOF-PET can lead to enhanced signal-to-noise ratio in the reconstructed image [Budinger]. **Table 1** provides a comparison of scintillators that are currently used in commercial PET scanners (BGO, LSO and GSO) as well as those that have been used to build PET scanners in past (NaI(Tl) and BaF₂).

Table 1. Properties of Inorganic Scintillators Used for PET

Material	Light Output [Photons/MeV]	Wavelength of Maximum Emission [nm]	Attenuation Length (511 keV) [cm]	Principal Decay Time [ns]
NaI(Tl)	38,000	415	3.3	230
LSO	24,000	420	1.2	40
BGO	8,200	505	1.1	300
GSO	7,600	430	1.5	60
BaF ₂	10,000	220 ^a , 310 ^b	2.3	0.6 ^a , 620 ^b

a-fast component, b-slow component

None of the established scintillators meet all the requirements of PET. BGO, GSO and LSO are commonly used in PET instrumentation due to their high gamma ray stopping efficiency. BGO, however, has low light output and relatively slow response. The light output of GSO is also low, though its response is faster than BGO. LSO is brighter and faster than BGO and GSO, which has made it one of the dominant scintillators for PET. However, LSO also has some drawbacks. Energy resolution of LSO is variable and is limited by its non-proportionality [Dorenbos 95 & 02, Mengesha, Moses 02]. NaI(Tl) has been used in PET designs in past [Adam] in view of its brighter response, lower cost and better energy resolution (compared to LSO, GSO and BGO). However, its slow response and low gamma-ray stopping efficiency limit its performance in 3-D PET imaging. BaF₂ has been considered for PET in past due to its very fast component (0.6 ns decay time) [Moszynski, Wong, Hollander]. However, the

amount of light covered by the fast component of BaF_2 is only about 2000 photons/MeV. The gamma-ray stopping efficiency of BaF_2 is also not very high.

If scintillators with high light output and fast as well as proportional response along with adequate stopping efficiency became available, they would represent a major breakthrough for PET application. Such scintillators would provide energy and timing resolution superior to what is achievable with commercially available scintillators at present and thus, provide improved ability for rejection of scattered and random events. Furthermore, scintillators with bright and fast luminescence may allow institution of new capabilities such as depth-of-interaction (DOI) encoding and time-of-flight data collection in PET. Both of these capabilities would provide improvement in PET image quality [Moses 95, Karp, Budinger]. Based on these considerations, investigation of newer scintillators such as cerium doped lanthanum bromide ($\text{LaBr}_3:\text{Ce}$), cerium bromide (CeBr_3) and cerium doped lutetium iodide ($\text{LuI}_3:\text{Ce}$) is presented in this thesis.

1.2 OVERVIEW OF PHOTODETECTORS FOR PET:

In addition to scintillators, optical detectors that capture the optical pulse from the scintillator upon gamma-ray irradiation and convert it into an electronic one are also an important component of the overall detection configuration used in existing PET scanners. At present, photomultipliers are almost exclusively used in clinical PET scanners. Photomultiplier tubes offer a number of very useful properties such as high amplification gain, very low electronic noise and fast response. They, however, also have some limitations: they are bulky, somewhat fragile, sensitive to magnetic field and have relatively low quantum efficiency. As a result, solid-state photodetectors based on silicon can be considered for PET. Silicon based photodetectors have the potential to offer high optical quantum efficiency and they are generally compact and rugged. Furthermore, most silicon sensors can be operated in high magnetic field which would allow integration of PET with magnetic resonance imaging (MRI), an emerging trend in medical instrumentation [Catana, Schlyer, Grazioso, Judenhofer]. In this thesis, investigation of silicon based photodetectors for PET imaging is presented.

1.3 SOME TRENDS IN PET INSTRUMENTATION

1.3.1 Depth of Interaction Encoding: Conventional PET detectors consist of photomultiplier tubes coupled to carefully segmented arrays of scintillators such as BGO, GSO or LSO. Anger-logic is used in computing the position of scintillation event. These existing detectors in clinical PET systems do not have the capability to encode depth-of-interaction (DOI). As a result, the spatial resolution in these PET systems gets progressively worse as the event locations moves further away (in radial direction) from the center of the field of view. Such parallax error (see **Figure 1**) can be reduced significantly if DOI encoding capability was available in PET modules. Ability to encode depth-of-interaction is particularly important in small animal imaging because if such capability existed, the detector modules can be brought right to the edge of the reconstruction circle. This reduces the number of modules required to build the scanner and thereby reduces the cost as well as complexity of the scanner. In small animal PET imaging, DOI encoding capability also provides possibility for higher sensitivity because thicker scintillation crystals can now be used. A number of approaches are being explored for DOI encoding. This includes the dual ended readout approach proposed by LBNL team where the scintillation array is sandwiched between PMT on one end and a silicon p-i-n photodiode array

on the other end [Moses 95]. Comparison of signal collected at both ends for a given event allows estimation of DOI because the photodetector closer to the event will produce larger signal.

Another method for DOI estimation includes phoswich approach where multiple scintillator layers with differing decay time are used [Seidel]. By measuring the decay time of the measured event, the scintillation layer in which the event was generated can be identified in order to generate DOI information. A combination of scintillator layers such as LSO:Ce, GSO and BGO [Seidel], LSO:Ce and LuYAP [Chung] or even layers of same scintillator, GSO with different Ce concentration (to achieve difference in decay time between layers [Inadama] have been explored to achieve DOI encoding.

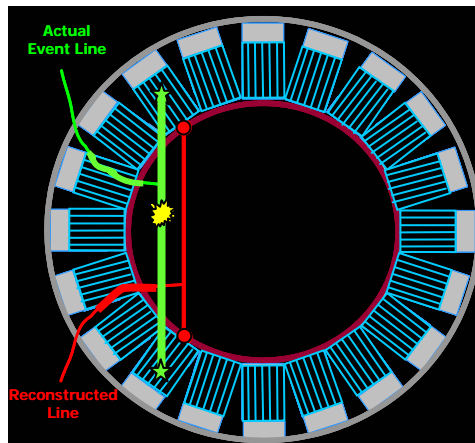


Figure 1. Schematic illustration of parallax error in PET scanners with ring geometry when DOI encoding capability is not available.

Other DOI encoding approaches with continuous scintillators include clustering methods (based on maximum-likelihood) that have been implemented on 8 mm thick scintillation crystals to extract DOI information [Ling] or readout of continuous scintillator with APD array where the event depth in the scintillator is determined from the distribution of the scintillation light over the APD array [Maas].

In this thesis, DOI encoding is demonstrated using LSO array sandwiched between two matching position sensitive avalanche photodiodes (PSAPDs) for PET modules designed for small animal imaging. Similarly, DOI encoding is also demonstrated using silicon photomultipliers (built using CMOS method) that sandwich LSO crystal.

1.3.2 Time-of-Flight PET Imaging: In conventional PET scanners, high timing resolution is desired to reduce the random events within the coincidence window. However, if the timing resolution of the PET detectors is very high, time-of-flight PET imaging can become possible which can lead to significant improvement in overall image quality [Budinger, Mullani, Karp, Moses 07].

Figure 2 provides a comparison of conventional and TOF PET imaging [Moses 03]. As seen in the figure, in case of conventional PET imaging, once a coincidence is established between two

detector elements in a PET ring, equal weight is assigned to all voxels between the two detectors (which represents the line-of-response, LOR) during the image reconstruction [Moses 03]. Thus, statistical noise from an activity in one voxel adds to overall noise along the line-of-response (LOR), which causes large noise amplification during image reconstruction. In case of time-of-flight (TOF) PET (see **Figure 2**), the event is localized to a short distance along the line-of-response, if the timing resolution of the detectors is high enough. Thus, in TOF-PET, only the noise associated to voxels within the localized segment along LOR is included in the reconstructed image, thereby reducing the noise amplification considerably.

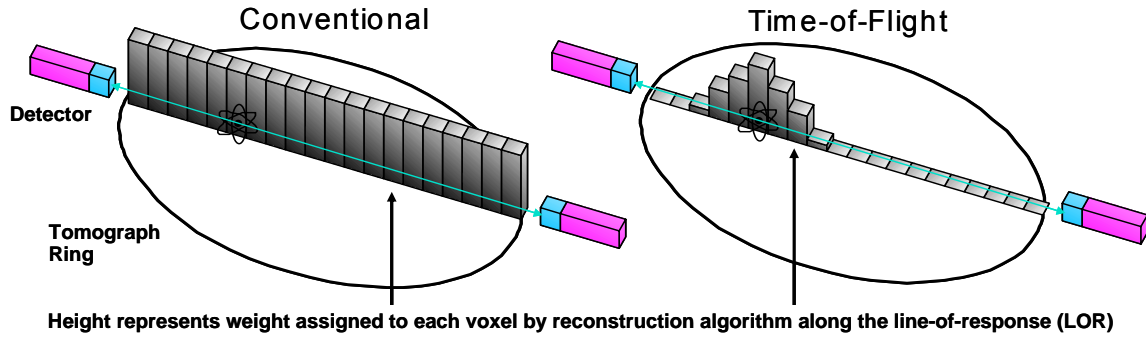


Figure 2. Schematic representation of conventional and time-of-flight PET imaging [Moses 03].

Figure 3 illustrates the extent of noise reduction in the images that can be achieved with time-of-flight PET, which depends strongly on the timing resolution of the detectors used to construct the PET scanner as well as the size of the object (or patient) being imaged [Moses 99]. For timing resolution of Δt , the distribution of activity is localized to distance Δx along the line-of-response (see **Figure 3**) and the relationship between these parameters can be expressed as $\Delta x = \Delta t \cdot c / 2$, where c is the speed of light.

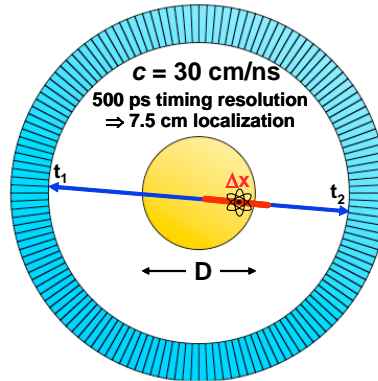


Figure 3. Schematic diagram of localization and variance reduction in TOF-PET [Moses 99]. Timing resolution of Δt allows an event to be localized within Δx ($= \Delta t \cdot c / 2$). The variance reduction in TOF-PET can be expressed as $D / \Delta x$, where D is the object diameter (or patient size). For a heavy patient ($D = 37.5$ cm), variance reduction with TOF-PET can be ~ 5 , if timing resolution is 500 ps.

The approximate variance reduction in TOF-PET can be expressed as $D/\Delta x$, where D is the object diameter (or patient size) [Moses 07]. Thus, the improvement associated with TOF-PET is amplified for heavier patients, where better image quality is desired most. If timing resolution of 500 ps (FWHM) is achieved with PET detectors, an event is localized within 7.5 cm. Taking case of a heavy patient ($D = 37.5$ cm), the variance reduction achieved with TOF-PET is ~ 5 , which is very attractive. Thus, it is clear that achieving timing resolution of about 500 ps or better is essential in exploiting the advantage offered by TOF-PET. To achieve such high timing resolution, fast and bright scintillators are required.

1.4 ORGANIZATION OF THIS THESIS

This thesis is organized in the following fashion: In **chapter 2**, techniques for growing $\text{LaBr}_3\text{:Ce}$, CeBr_3 , and $\text{LuI}_3\text{:Ce}$ crystals are discussed and an overview of methods used to measure scintillation performance of these compositions is provided. Basic scintillation properties as well as energy and timing resolution of $\text{LaBr}_3\text{:Ce}$, CeBr_3 and $\text{LuI}_3\text{:Ce}$ scintillators are presented in **chapters 3, 4 and 5**, respectively. These chapters are based on (or adapted from) prior publications and presentations covering these compositions. In **chapter 6**, characteristics of the new elpasolite and alkaline earth halide scintillators are covered, particularly from the viewpoint of SPECT imaging. This chapter is based on prior presentations, reports and publications covering these compositions.

In **chapters 7 and 8**, silicon avalanche photodiodes with position sensitivity are discussed with **chapter 8** focusing on investigation of these devices for small animal PET imaging. Both these chapters are based on prior publications. In **chapter 9**, silicon photomultipliers (SiPMs) built using CMOS processing are discussed for PET. This chapter is based on prior presentations, a provisional U.S. patent application and research progress reports submitted to U.S. federal agencies. Conclusions and summary are presented in **chapters 10 and 11**, respectively

References:

- L.E. Adam, Karp JS, Daube-Witherspoon ME, Smith RJ. *Performance of a Whole-Body PET Scanner Using Curve-Plate NaI(Tl) Detectors*. J Nucl Med 48: 1821-1830, (2001).
- Budinger TF. *Time-of-flight positron emission tomography: status relative to conventional PET*. J. Nucl. Med. 24: 73-78, 1983.
- J.T. Bushberg, J.A. Seibert, E.M. Leidholdt, and J.M. Boone, **The Essential Physics of Medical Imaging**, Williams and Wilkins, (1994).
- C. Catana C, Wu Y, Judenhofer M, Pichler B, Cherry S. A PSAPD-Based System for Simultaneous Multi-Slice PET and MRI. In: Molecular Imaging and Biology, 82, (2006).
- SR Cherry, JA Sorenson, ME Phelps: **Physics in Nuclear Medicine**, Third Edition, W.B. Saunders, Philadelphia, (2003).
- Cherry, S. R. and Gambhir, S. S., Use of positron emission tomography in animal research, *ILAR J* 42, 219-232, 2001.
- Chung, YH et. al., Optimization of Dual Layer Phoswich Detector Consisting of LSO and LuYAP for Small Animal PET, IEEE Trans. Nuc. Sci., V.52(1), p. 217, (2005)

- P. Dorenbos, *Light output and energy resolution of Ce^{3+} doped scintillators*, Nucl. Instr. and Meth., V. 486, p. 208, (2002).
- P. Dorenbos, *et. al.*, *Non-Proportionality in the Scintillation Response and the Energy Resolution Obtainable with Scintillation Crystals*, IEEE Trans. Nuc. Sci., 42(6), p. 2190, (1995).
- R. Grazioso, R. Ladebeck, M. Schmand, R. Krieg, APD-Based PET for Combined PET-MR Imaging, Proc. Intl. Soc. Mag. Res. Med., Vol.13, (2005).
- Hollander, R. W.; Schotanus, P.; van Eijk, C. W. E., Recent developments for a BaF_2 /TMAE PET-camera, Nuclear Instruments and Methods in Physics Research Section A, Volume 283, Issue 3, p. 448-453, (1989)
- Inadama, N., *et. al.*, A Depth of Interaction Detector for PET with GSO Crystals Doped with Different Amounts of Ce, IEEE Trans. Nuc. Sci., V49(3), p. 629, (2002).
- M.S. Judenhofer, C. Catana, B.K. Swann, S.B. Siegel, W-I Jung, R.E. Nutt, S.R. Cherry, C.D. Claussen, and B.J. Pichler, PET/MR Images Acquired with a Compact MR-compatible PET Detector in a 7-T Magnet, Radiology;244:807-814, 2007
- Ling, T., Lewellen, T.K., Miyaoka, R.S., Investigation of Depth of Interaction Decoding for a Continuous Crystal Detector, IEEE NSS Conference Record, p. 3012, (2006).
- J. S. Karp, A. Kuhn, A. E. Perkins, S. Surti, M. E. Werner, *et al.* Characterization of a time-of-flight PET scanner based on lanthanum bromide. Proceedings of The IEEE 2005 Nuclear Science Symposium, pp. M4-8, (Edited by B. Yu), San Juan, Puerto Rico, (2005).
- K. Kleinknecht, **Detectors for Particle Radiation**, 2nd Edition, Cambridge University Press, Cambridge, U.K. (1998).
- G. Knoll, **Radiation Detection and Measurement**, 3rd Ed., John Wiley and Sons, (1999).
- Maas, MC, *et. al.*, Experimental Characterization of Monolithic-Crystal Small Animal PET Detectors Read Out by APDs, IEEE Trans. Nuc. Sci., V53(2), p. 1071, (2006)
- W. Mengesha, T. D. Taulbee, B. D. Rooney, *et al.*, *Light yield nonproportionality of $CsI(Tl)$, $CsI(Na)$, and YAP*, IEEE Trans. Nucl. Sci., vol. 45, pp. 456-461, (1998).
- W.W. Moses, Recent Advances and Future Advances in time-of-flight PET, Nuclear Instruments in Physics Research A, V 580, Issue 2, pp. 919-924, (2007).
- W. W. Moses, Time of flight in PET revisited, IEEE Trans. Nucl. Sci., vol. NS-50, pp. 1325-1330, (2003).
- W.W. Moses, *Current trends in scintillator detector and materials*, Nucl. Inst. and Meth. A-487, pp. 123-128, (2002).
- W. W. Moses and S. E. Derenzo, Prospects for time-of-flight PET using LSO scintillator, IEEE Trans. Nucl Sci., vol. NS-46, pp. 474-478, (1999).
- W.W. Moses, *et al.* A room temperature LSO/PIN photodiode PET detector module that measures depth of interaction, IEEE Trans Nucl Sci 42: 1085-1089, (1995).
- M. Moszynski, Allemand R, *et. al.*, Further study of scintillation counters with BaF_2 crystals for Time-of-Flight Positron Tomography in medicine, Nucl. Instru. Meth. A 226: 534- 541, (1984).
- Mullani NA, Markham J, Ter-Pogossian MM. "Feasibility of time-of-flight reconstruction in positron emission tomography." Journal of Nuclear Medicine. 1980; 21(11):1095-7.
- Phelps, M. E. *Positron emission tomography provides molecular imaging of biological processes*, Proc Natl Acad Sci, 97(16), 9226-9233, (2000).

- P. A. Rodnyi, **Physical Processes in Inorganic Scintillators**, CRC Press, New York, (1997)
- D. Schlyer, P. Vaska, C. Woody, D. Tomasi, S. Southehal, S. Solis-Najera, S. Stoll, J. Pratte, S. Junnarkar, S. Krishnamoorthy, M. Purschke, S. Park, S. Maramraju, A. Kriplani, First images from the BNL simultaneous PET/MRI scanner, J Nucl Med.; 48 (Supplement 2):89P, (2007)
- Seidel, J.; Vaquero, J.J.; Siegel, S.; Gandler, W.R.; Green, M.V., Depth identification accuracy of a three layer phoswich PETdetector module, Nuclear Science, IEEE Transactions on, Volume 46, Issue 3, Page(s):485 – 490. Jun 1999
- D W Townsend, T Beyer, A combined PET/CT scanner: the path to true image fusion, British Journal of Radiology 75, S24-S30, (2002)
- Wong, Wai-Hoi; Mullani, Nizar A.; Wardworth, Gary; Hartz, Ross K.; Bristow, David, Characteristics of Small Barium Fluoride (BaF_2) scintillator for high intrinsic resolution Time-of-Flight Positron Emission Tomography, IEEE Trans. Nuc. Sci., Volume 31, Issue 1, Feb. Page(s):381 – 386, 1984

CHAPTER 2: EXPERIMENTAL METHODS FOR SCINTILLATION STUDIES

2.1 OVERVIEW

In this chapter, experimental techniques used for scintillation studies are discussed. First, the methods used to grow crystals of $\text{LaBr}_3\text{:Ce}$, CeBr_3 and $\text{LuI}_3\text{:Ce}$ are presented. The techniques used in measuring emission spectra, decay time spectra and light output of various scintillators are then covered.

2.2 CRYSTAL GROWTH METHOD:

The scintillation materials investigated in this research ($\text{LaBr}_3\text{:Ce}$, CeBr_3 , $\text{LuI}_3\text{:Ce}$ and other related mixed halides) all melt congruently at relatively low temperatures (below 1100°C). As a result, crystals of these compositions can be grown directly from the melt using processes such as Bridgman and Czochralski [Brice]. Melt based crystal growth processes are very widely used in the field of scintillation materials and most commercial scintillators (including NaI:Tl and CsI:Tl) are grown using melt based Bridgman and Czochralski methods.

To grow crystals of $\text{LaBr}_3\text{:Ce}$, CeBr_3 , $\text{LuI}_3\text{:Ce}$ and other related mixed halides, Bridgman method with vertical orientation of crucible was used in this research (see **Figure 1**). In view of relatively low melting points of the chosen materials (below 1100°C), quartz crucibles were used. Ultra-dry starting powders of the host composition as well as the activator in appropriate ratio were loaded in quartz ampoules, which were then sealed. For growth of $\text{LaBr}_3\text{:Ce}$, the constituents inside the ampoule would be ultra-dry LaBr_3 and CeBr_3 . These ampoules were then dropped through a vertical Bridgman furnace that has two zones (see **Figure 1**). The upper zone of the furnace was kept above the melting point of all the constituents placed inside the ampoule. This allowed the constituents to mix well and react in the molten phase to form. The lower zone of the furnace was kept below the melting point of the synthesized compound. As a result, the crystals of the desired composition were formed as the ampoule entered the lower zone. Important process parameters for successful crystal growth were temperature gradients in the furnace, crucible design, growth-rate and cooling rate for the grown crystal. Crystals were mostly grown in ampoules with 1 cm diameter for evaluation purposes (for example, a photograph of a $\text{LaBr}_3\text{:Ce}$ crystal is shown in **Figure 2**). These crystals were taken out of the ampoule and processed. These crystals were cut

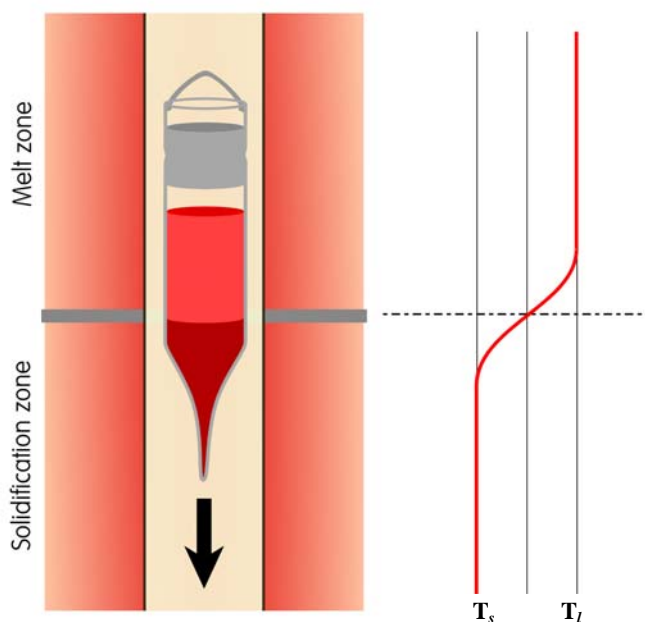


Figure 1. Schematic of Bridgman crystal growth setup used for growth of $\text{LaBr}_3\text{:Ce}$, CeBr_3 , $\text{LuI}_3\text{:Ce}$ and related materials.

using a diamond coated wire saw and the surfaces exposed as a result of these cuts were polished using non-aqueous slurries (due to hygroscopic nature of the chosen compositions) prepared by mixing mineral oil with SiO_2 , CeO , or Al_2O_3 ($< 1 \mu\text{m}$ grit size). In some instances, these crystals were packaged to prevent long exposure to moisture. These crystals were then evaluated using techniques discussed in the following section.

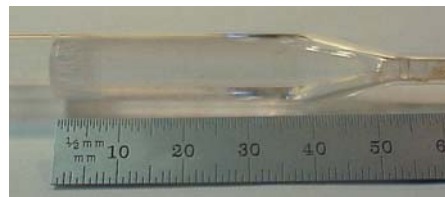


Figure 2. Photograph of a Bridgman grown $\text{LaBr}_3:\text{Ce}$ crystal (1 cm diameter crystal with >2.5 cm length).

2.3 RADIOLUMINESCENCE MEASUREMENTS

Radioluminescence measures the spectral distribution of the light emitted by a scintillator upon excitation with an X-ray source. A typical setup used for radioluminescence measurements includes an X-ray source, a monochromator, a photodetector and control electronics. A schematic representation of a radioluminescence setup is shown in **Figure 3**.

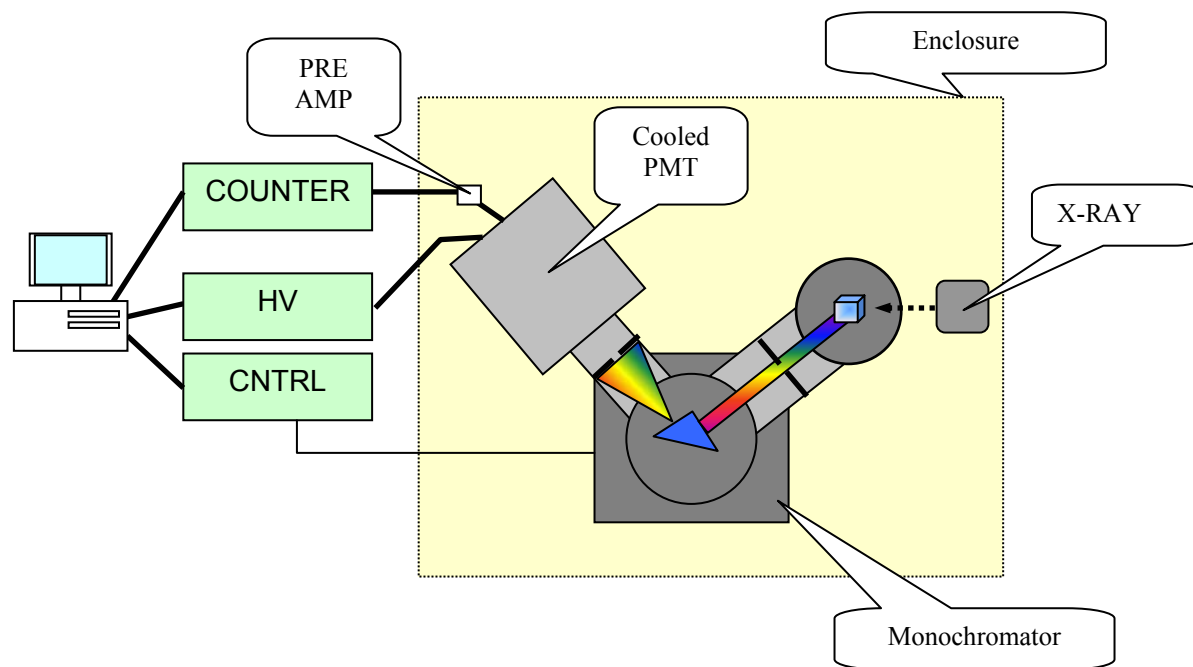


Figure 3. Schematic representation of a setup used for measuring radioluminescence of a scintillator.

The X-rays are generated by a Philips X-ray generator with a copper target. The typical lamp voltage and current settings are 40 kV and 20 mA, though they are often varied to accommodate various scintillator samples. The X-rays irradiate a scintillation crystal placed in a sample chamber. The chamber has a beryllium entrance window. The scintillation crystal is placed on a stand that also can hold a small mask, if necessary, to irradiate only part of the sample. The experiments with the mask are useful when comparing the emission intensities of different materials. The light produced by the excited sample is collected through the slits by a McPherson 302 monochromator. The grating in the monochromator disperses the light that is then detected by a light detector on the other side of the monochromator. Usually, the slits are set to 2 mm, leading to the 8 nm resolution for the system. Photomultipliers are used as a light

detector. Depending on the spectral range of interest a Hamamatsu R2059 or Burle C31034 PMTs are used. The former has a bialkali photocathode and is more sensitive in the ultraviolet and visible region (180-650 nm), while the later has a GaAs:Cs-O photocathode and is sensitive in the 300 to 900 nm range. The photomultipliers are placed in a housing that uses dry ice to cool them, in order to reduce dark counts. The data collection system works in the photon counting mode. Thus the output of a photomultiplier is connected through a small Ortec VT120 preamplifier to a photon counter (Stanford Research, SR400). The counter is controlled by a PC computer. The computer also controls the monochromator. A typical run collects the counts for 1 second at each scanned wavelength. The monochromator step is usually 1 nm. Longer collection times are used if the emission has low intensity.

2.4 LIGHT YIELD AND ENERGY RESOLUTION MEASUREMENTS

For light output and energy resolution measurements, pulse height spectra are recorded with scintillator directly attached to a photomultiplier tube. The scintillator is typically wrapped in Teflon tape on all sides, except the attached face. The Teflon reflects the light towards the photomultiplier tube. A Teflon lined cap can be used as a reflector as well. The sample typically is attached using silicon grease that improves the optical coupling between the crystal and photomultiplier tube. The current setup at RMD uses a Hamamatsu R6233 photomultiplier tube with a bialkali photocathode, though other PMTs (such as Hamamatsu's R2059 or Hamamatsu's R6233S) are also used. The signal produced by the tube is first collected by a preamplifier (Canberra, 2005) that initially integrates, amplifies and shapes it. This signal is then sent to a spectroscopy amplifier (Canberra, 2022). The amplifier allows for adjustments of gain and shaping time. The shaping time for a given scintillation sample is chosen on the basis of its decay time. For slow scintillation pulses, longer shaping time needs to be used to collect as many photons as possible. The shaping time can be set from 0.5 to 12 microseconds. The signal from the amplifier is then fed to an ADC (Canberra) and then an MCA card (Canberra, M100) in a personal computer that collects the data as shown in **Figure 4**.

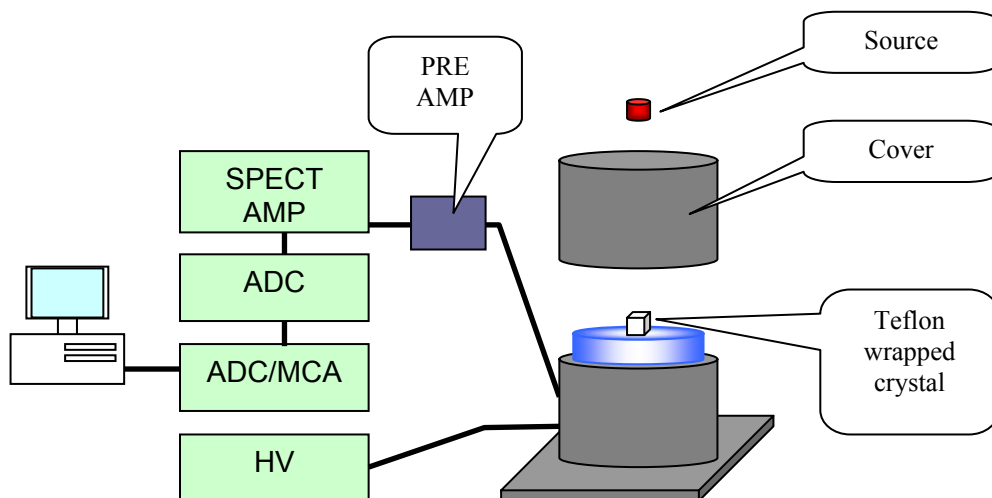


Figure 4. Experimental setup used for light yield and energy resolution measurements.

From the measured pulse height spectrum for given gamma-ray irradiation, the characteristics photopeak(s) are identified. From Gaussian fit to each peak, its mean amplitude

and its broadening are estimated to compute its energy resolution, which is reported usually as percentage-FWHM.

Using such pulse height measurements, it is also possible to estimate the light yield of a given scintillator. The experiment involves acquiring a pulse height spectrum with the scintillator being investigated using an isotopic source (such as ^{137}Cs that emits 662 keV gamma-rays). Next, a pulse height spectrum for the same isotope is acquired using a well established scintillator with known light yield (for example, BGO which emits 8,200 photons/MeV). The measurements are performed using the same settings. If different amplifier gains are used, the spectra are scaled accordingly. By comparing the photopeak positions for the investigated sample and the reference sample, the light yield of the investigated sample can be estimated from the known light yield of the reference sample after taking into account the difference in the quantum efficiency of the PMT over the spectral emission of the investigated sample and the reference sample. The following expression can be used to estimate the light yield of the investigated sample:

$$LY = \frac{p_s}{p_r} \times \frac{qe_r}{qe_s} \times LY_r,$$

where p_s and p_r are respective photopeak positions (s for the investigated sample, r for the reference sample), qe_s and qe_r are respective quantum efficiency values, and LY_r is the light yield of the reference BGO crystal (in photons / MeV). The result represents the light yield of the investigated sample in photons per 1 MeV of the incident gamma-ray energy.

2.5 DECAY TIME MEASUREMENTS

The simplest way to measure a decay time curve of scintillation is to record the trace on a digital oscilloscope, such as TDS 220 from Tektronix as illustrated in **Figure 5**.

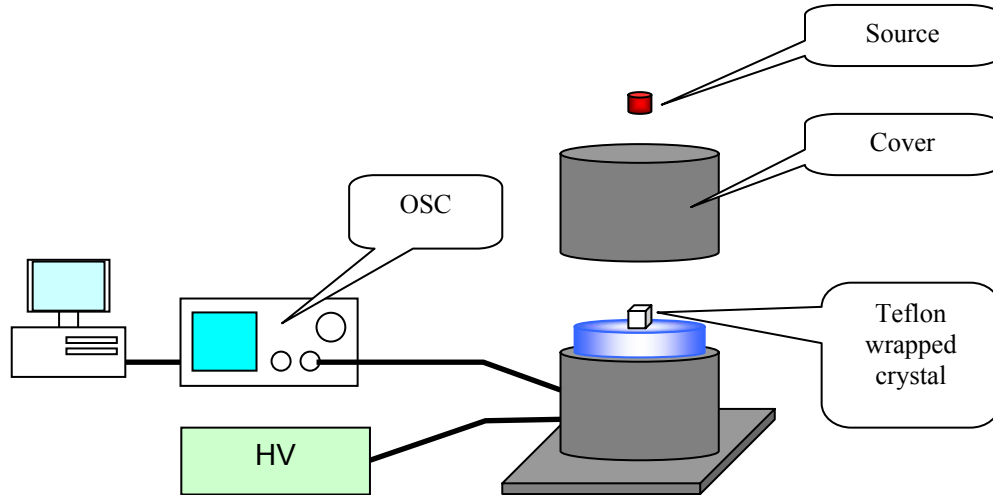


Figure 5. Experimental setup used to measure scintillator decay time using a fast, digital oscilloscope.

In this experiment the crystal is attached to a PMT (such as Hamamatsu's R2059) and irradiated by gamma particles from a radioactive source. The output of the PMT is directly connected to the scope. A 50 Ohm input impedance is necessary to preserve fast components of the scintillation pulse. Higher impedance will lead to integration of the signal as the result will

be determined by the RC time constant of the setup rather than the intrinsic scintillation pulse. The settings on the scope need to be adjusted to accommodate the decay time constant and the signal strength. Single traces or averaged pulses can then be collected and transmitted from the scope to a personal computer. The data is fitted to a sum of exponentials and a time independent background to estimate decay time constant(s) for the investigated sample. The main advantage of this method is in its simplicity. A single trace can be collected within seconds. On the other hand for low intensity emission it can be quite difficult to collect decay spectra. Also, the resolution is limited by the scope. While decay times are usually slow enough to be reliably captured, rise time features are often too fast and are limited by the scope – PMT setup.

Another method that has been used for decay time measurements has been the delayed coincidence method [Bollinger]. Decay time measurements have been made using the Pulsed X-Ray Facility available at the Lawrence Berkeley National Laboratory (Berkeley, California, USA). The x-ray source is a light-excited x-ray tube that produces 4,000 x-ray photons (mean energy 18.5 keV) per steradian in each 1 ps fwhm pulse, with a 50 kHz repetition rate. The investigated sample is placed in the x-ray beam and its fluorescent emanations are detected with a sapphire-windowed microchannel plate photomultiplier tube (spectral range 150-650 nm, transit time jitter 40 ps fwhm). The time difference between the x-ray pulse and the detected fluorescent emissions is measured using a TAC / ADC combination having 2 ps fwhm resolution, and the decay time spectrum is acquired with the delayed coincidence method [Bollinger]. The total system response time is 60 ps fwhm. The acquired spectrum is fitted to a sum of exponentials (representing rise and decay time components) along with a time independent background. The main advantage of this method is that it allows accurate estimation of very fast components that may be present in the temporal response of the sample.

2.6 COINCIDENCE TIMING RESOLUTION MEASUREMENTS

Timing resolution of various new crystals has been measured using an experimental setup (see **Figure 6**) available at Lawrence Berkeley National Laboratory (Berkeley, California, USA).

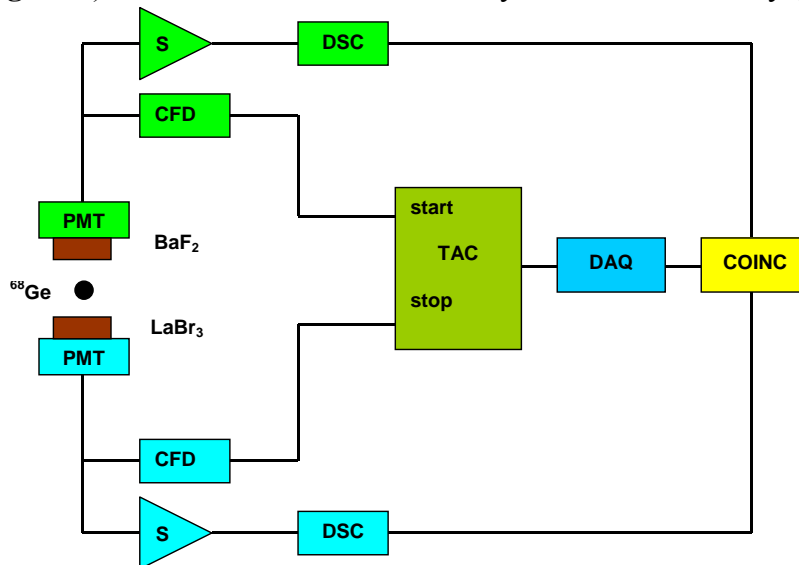


Figure 6. Schematic diagram of setup used to measure coincidence timing resolution of various new scintillators.

This experiment involves irradiating a reference scintillator (BaF_2) and an investigated scintillator (for example, $\text{LaBr}_3\text{:Ce}$), each coupled to a fast PMT (Hamamatsu R-5320) with 511 keV positron annihilation γ -ray pairs (emitted by a ^{68}Ge source). The BaF_2 -PMT detector forms a “start” channel in the timing circuit, while the LaBr_3 -PMT detector forms the “stop” channel. The signal from each detector is processed using two channels of a Tennelec TC-454 CFD that has been modified for use with fast (sub-ns) rise-time PMTs. The time difference between the start and stop signals is digitized with a Tennelec TC-862 TAC and a 16-bit ADC, resulting in a TDC with 7.5 ps per bin resolution. The coincidence timing distribution is acquired in this manner and by performing a Gaussian fit to the spectrum, the coincidence timing resolution (in ns-FWHM or ps-FWHM) is estimated.

In some instances, other experimental approaches have also been used, which are discussed when the corresponding measurements and data analysis is presented.

2.7 REFERENCES

- L. M. Bollinger and G. E. Thomas, “Measurement of the time dependence of scintillation intensity by a delayed-coincidence method”, *Rev. Sci. Instr.*, vol. 32, p. 1044, (1961).
J. C. Brice, **Crystal Growth Processes**, UK: Blackie Halsted Press, 1986.

CHAPTER 3: CERIUM DOPED LANTHANUM BROMIDE SCINTILLATORS

3.1 OVERVIEW

This chapter covers investigation of cerium doped lanthanum halide scintillators. This chapter has been adapted from the following two publications: (i) K.S. Shah *et. al.*, LaBr₃:Ce Scintillators for Gamma-Ray Spectroscopy, IEEE Transactions on Nuclear Science V. 50(6), (2003) and (ii) K.S. Shah *et. al.*, High Energy Resolution Scintillation Spectrometers, IEEE Transactions on Nuclear Science, V 51(5), (2004). These publications cover investigation of some of the basic scintillation properties of LaBr₃ as a function of cerium concentration (up to 5%). Additional results covering the variation of scintillation properties as well as timing resolution at higher cerium concentrations (beyond 5%), which were not available at the time of the publications listed above are included here. Analysis of the energy resolution of LaBr₃:Ce scintillators read out with photomultiplier tubes as well as silicon avalanche photodiodes is included in this chapter.

3.2 INTRODUCTION:

Scintillation spectrometers are widely used in detection and spectroscopy of energetic photons (γ -rays) at room temperature. As mentioned earlier, these detectors are commonly used in nuclear and high energy physics research, medical imaging, non-destructive testing, nuclear treaty verification and safeguards, and geological exploration [Knoll, Kleinknecht]. Important requirements for the scintillation crystals used in these applications include high light output, high stopping efficiency, fast response, low cost, good linearity, and minimal afterglow. These requirements cannot be met by any of the commercially available scintillators.

Scintillation crystals such as NaI(Tl) and CsI:Tl provide high light output and are available in large sizes that are required in many of the mentioned applications. However, the energy resolution of these scintillators is poor, about 6 to 7% (FWHM) at 662 keV gamma ray energy (¹³⁷Cs source). This energy resolution is much worse than the predicted value of about 3 to 4% (FWHM) at 662 keV for these scintillators coupled to photomultiplier tubes (based on photoelectron statistics). Furthermore, even small crystals of these scintillators provide poor energy resolution, which indicates that factors such as non-uniformity and crystal quality do not completely account for the degradation of their energy resolution. The prevailing hypothesis for the degradation of the energy resolution of these common scintillators such as NaI(Tl), Cs(Tl), LSO and others is non-proportionality [Moses 02, Dorenbos 95 & 02, Mengesha]. It has been observed that for many inorganic scintillators the light emitted per unit energy is not constant but depends on the energy of the excitation electrons [Dorenbos 95, Mengesha]. The pulse height for a scintillation spectrometer for each gamma ray event is caused by multiple excitation electrons of varying energy. Furthermore, for gamma ray events with the same energy, the energy of cascading excitation electrons can vary. As a result, for scintillators that are non-proportional, additional broadening occurs beyond what would be expected based on counting statistics. Thus, in order to obtain high energy resolution with scintillators, high light output as well as high proportionality is required.

In this chapter, we report on a relatively new scintillator, Ce³⁺ doped LaBr₃ [van Loef 01] which satisfies both these requirements and as a result provides high energy resolution. One of the important aspects of the research presented in this chapter is the investigation of scintillation

properties of LaBr_3 as a function of Ce^{3+} concentration (0.5% to 30% on molar basis). The results, discussed in detail in this chapter, indicate that timing response of $\text{LaBr}_3\text{:Ce}$ improves considerably as the Ce^{3+} concentration is increased [Shah 03]. This behavior can be exploited for applications such as positron emission tomography that require fast response and high timing resolution.

3.3 PREPARATION OF $\text{LaBr}_3\text{:Ce}$ CRYSTALS

LaBr_3 crystals have hexagonal (UCl_3 type) structure with P63/m space group and their density is 5.1 g/cm^3 . The compound melts congruently at 783°C and therefore its crystals can be grown using melt based methods such as Bridgman and Czochralski. This is fortunate because these melt based processes are well suited for growth of large volume crystals [Brice]. In the research reported in this chapter, vertical Bridgman method has been used for growing $\text{LaBr}_3\text{:Ce}$ crystals.

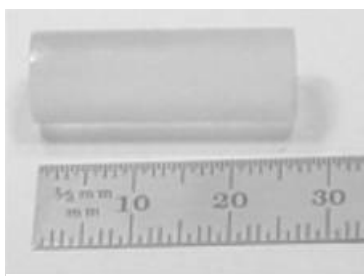


Figure 1. Photograph of an RMD grown $\text{LaBr}_3\text{:Ce}$ crystal (about 2 cm^3 in size).

Quartz ampoules were used as crucibles and ultra-dry LaBr_3 and CeBr_3 powders (99.99%, Alfa/Aesar) were loaded in such ampoules, which were then sealed. These ampoules were then dropped through the vertical Bridgman furnace that has two zones. The upper zone of the furnace was kept at temperature of 850°C , which is above the melting point of LaBr_3 and CeBr_3 . This allowed the constituents to mix well and react in the molten phase to form $\text{LaBr}_3\text{:Ce}$. The lower zone of the furnace was kept at 700°C or lower (which is below the melting point of LaBr_3 and CeBr_3). As a result, $\text{LaBr}_3\text{:Ce}$ crystals were formed as the ampoule entered the lower zone. LaBr_3 crystals with volume greater than 2 cm^3 were grown in this manner. **Figure 1** shows a photograph of a $\text{LaBr}_3\text{:Ce}$ crystal grown by the Bridgman method. Initial growth runs were performed with Ce^{3+} concentration of 0.5% (on molar basis). In the later runs, the amount of CeBr_3 in the feed material was adjusted to produce LaBr_3 samples with other Ce^{3+} concentration (0.2%, 0.5%, 1.3% and 5%) in order to study the effects of variation in cerium concentration on the scintillation properties of LaBr_3 .

The grown crystals were removed from the quartz ampoule and then cut and polished using non-aqueous slurries (due to hygroscopic nature of LaBr_3) prepared by mixing mineral oil with Al_2O_3 grit. The crystals were then packaged to prevent long exposure to moisture. This involved encapsulating the crystal in an epoxy (Epoxy STYCAST#1266 Value23LV Titanium Oxide and EPO-TEK 301 between the crystal and window) with a thin quartz window (0.5 mm) placed on the crystal face, which would be coupled to an optical sensor. Other packaging schemes were also tried which involved placing a crystal in a metal can with a quartz window on one face. The crystal was attached to the quartz window using optical epoxy (EPO-TEK 301)

and then SiO₂ powder was pressed in the space between the metal can and the crystal. The metal disk was then attached to the top surface to seal the detector.

3.4 SCINTILLATION PROPERTIES OF LaBr₃:Ce

We have performed characterization of the scintillation properties of LaBr₃ crystals grown by the Bridgman process. This investigation involved measurement of the light output, the emission spectrum, and the fluorescent decay time of the crystals. Variation of these scintillation properties with Ce³⁺ concentration was analyzed. Energy and timing resolution of LaBr₃:Ce crystals were also measured.

3.4.1 Light Output and Energy Resolution

The light output of LaBr₃:Ce crystals was measured by comparing their response and the response of a calibrated BGO scintillator to the same isotope (662 keV γ -rays, ¹³⁷Cs source, see **Figure 2**). These measurements involved optical coupling of a LaBr₃:Ce sample to a photomultiplier tube (with multi-alkali S-20 photocathode), irradiating the scintillator with 662 keV photons and recording the resulting pulse height spectrum. In order to maximize light collection, LaBr₃:Ce crystals were wrapped in reflective, white Teflon tape on all faces (except the one coupled to a photomultiplier (PMT)). An index matching silicone fluid was also used at the PMT-scintillator interface. A pulse height spectrum was recorded with a LaBr₃:Ce crystal (~1 cm³ size, 0.5% Ce). This experiment was then repeated with a calibrated BGO scintillator (which had light output of 8000 photons/MeV). **Figure 2** shows pulse height spectra for both LaBr₃:Ce and BGO under ¹³⁷Cs irradiation and amplifier shaping time of 4.0 μ sec. This shaping time is long enough to allow full light collection from both the scintillators. The PMT bias and amplifier gain were the same for both spectra. Based on the recorded photopeak positions for LaBr₃:Ce and BGO, and by taking into account the photocathode quantum efficiency for BGO and LaBr₃:Ce, we estimated light output of LaBr₃:Ce crystal with 0.5% Ce to be about 60,000 photons/MeV.

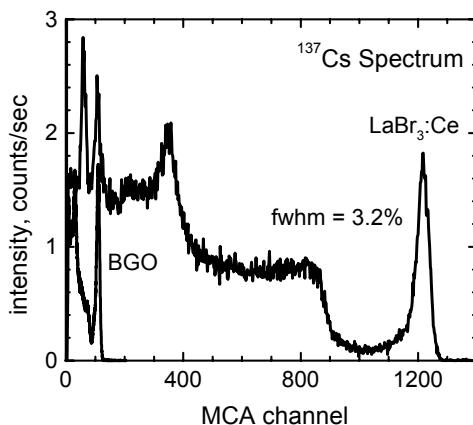


Figure 2. ¹³⁷Cs spectra recorded with LaBr₃:Ce and BGO for comparison.

We also studied variation in light output of LaBr₃:Ce crystals as a function of the cerium concentration in these crystals. Crystals with cerium concentration of 0.2%, 1.3%, and 5% were investigated. Each crystal was coupled to PMT and 662 keV γ -ray spectra (¹³⁷Cs source) were

recorded with these crystals under identical operating conditions. Data were collected at shaping time of 4 μ s and the results reported in **Table I**, indicate that all Ce^{3+} concentrations provide high light output. The light output of the sample with 1.3% Ce^{3+} concentration is lower than expected, which is probably due to poorer quality of that crystal as compared to other samples.

The energy resolution of the 662 keV photopeak recorded with $\text{LaBr}_3\text{:Ce}$ scintillator has been measured to be 3.2% full-width at half-maximum (FWHM) at room temperature as shown in **Figure 2**. Such high energy resolution has not been achieved with any of the established inorganic scintillators. It should be noted that the energy resolution obtained with $\text{LaBr}_3\text{:Ce}$ crystals approaches the energy resolution of room temperature semiconductor detectors such as CdTe and CdZnTe of similar size. We have also characterized a $\text{LaBr}_3\text{:Ce}$ crystal (coupled to a PMT) using other gamma ray energies such as 511 keV (^{22}Na source) and 122 keV (^{57}Co source) and have found its energy resolution to be 3.6% (FWHM) and 6.8% (FWHM), respectively, at room temperature.

3.4.2 Emission Spectrum

We measured the emission spectrum of the $\text{LaBr}_3\text{:Ce}$ scintillators. The $\text{LaBr}_3\text{:Ce}$ samples were excited with radiation from a Philips X-ray tube having a copper target. The scintillation light was passed through a McPherson monochromator and detected by a Hamamatsu R2059 photomultiplier tube with a quartz window. **Figure 3** shows the normalized emission spectra for $\text{LaBr}_3\text{:Ce}$ samples with 0.2, 0.5, 1.3, and 5% Ce concentrations. As seen in the figure, emission peaks at 360 and 380 nm, which are characteristic for Ce^{3+} luminescence, are present for all four cerium concentrations.

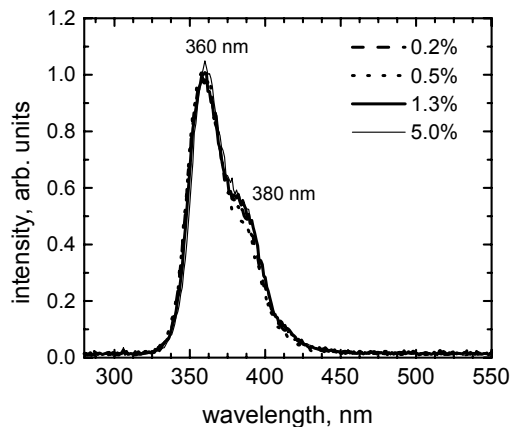


Figure. 3. Emission spectra measured for $\text{LaBr}_3\text{:Ce}$ crystals with four different Ce^{3+} concentrations.

3.4.3 Decay Time

The fluorescent decay times of $\text{LaBr}_3\text{:Ce}$ samples (doped with 0.2, 0.5, 1.3 and 5% Ce) were measured using the delayed coincidence method [Bollinger]. Decay time measurements were made at the LBNL Pulsed X-Ray Facility. The x-ray source is a light-excited x-ray tube that produces 4,000 x-ray photons (of mean energy 18.5 keV) per steradian in each 1 ps FWHM pulse, with a 50 kHz repetition rate. The $\text{LaBr}_3\text{:Ce}$ samples were placed in the x-ray beam and

their fluorescent emanations were detected with a sapphire-windowed microchannel plate photomultiplier tube (spectral range 150-650 nm, transit time jitter 40 ps FWHM). The time difference between the x-ray pulse and the detected fluorescent emissions was measured using a TAC/ADC combination having 2 ps FWHM resolution. The total system response time is 60 ps FWHM. The decay time spectrum for each LaBr₃:Ce sample was measured up to 430 ns after x-ray exposure in this manner and was fitted to the sum of exponentials and a time-independent background. The fit results are shown in **Figure 4** and **Table I**. As seen in the table, all samples independent of Ce³⁺ concentration show very fast principal decay constant (≤ 25 ns). These results are consistent with the emission spectra shown in **Figure 3** where Ce³⁺ luminescence appears to be the primary scintillation component. Some evidence of rise time (in <1 to >5 ns range) was also observed in these studies. The light output, optical emission, and decay time data for all four Ce³⁺ concentrations in LaBr₃ are summarized in **Table I**.

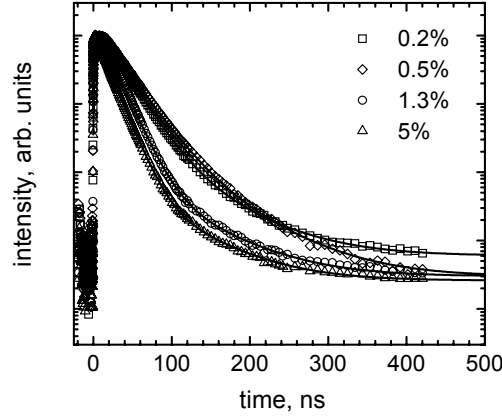


Figure 4. Decay time spectra for LaBr₃ crystals with 0.2, 0.5, 1.3, and 5% Ce³⁺ concentrations, along with multi-exponential fits to the measured data.

TABLE I
SCINTILLATION PROPERTIES OF LaBr₃:Ce WITH DIFFERENT Ce³⁺
CONCENTRATIONS (0.2 TO 5% RANGE)

Ce ³⁺ Concentration (%)	Light Output (Photons/MeV)	Rise Time (ns)	Decay Times (ns)
0.2	60,700	3.5	23 ns (93.4%), 66 ns (6.6%)
0.5	60,000	3.4	26 ns (93%), 66 ns (7%)
1.3	47,000	2.9	16.5 ns (97%), 66 ns (3%)
5	55,300	0.7	15 ns (97%), 63 ns (3%)

3.4.4 Coincidence Timing Resolution

Coincidence timing resolution of LaBr₃:Ce crystals with various Ce³⁺ concentrations has been measured. This experiment involved irradiating a BaF₂ and LaBr₃:Ce scintillators, each coupled to a fast PMT (Hamamatsu R-5320, operated at -2000V) with 511 keV positron annihilation γ -ray pairs (emitted by a ⁶⁸Ga source). The BaF₂-PMT detector formed a “start”

channel in the timing circuit, while the LaBr₃-PMT detector formed the “stop” channel. The signal from each detector was processed using two channels of a Tennelec TC-454 CFD that had been modified for use with fast (sub-ns) rise-time PMTs. The time difference between the start and stop signals was digitized with a Tennelec TC-862 TAC and a 16-bit ADC, resulting in a TDC with 7.5 ps per bin resolution. Data were accumulated until the coincidence timing distribution had approximately 10,000 counts in the maximum bin. **Figure 5** shows a coincidence timing resolution plot acquired in this manner with LaBr₃:Ce crystal having 5% Ce³⁺ concentration and the timing resolution was measured to be 260 ps (FWHM).

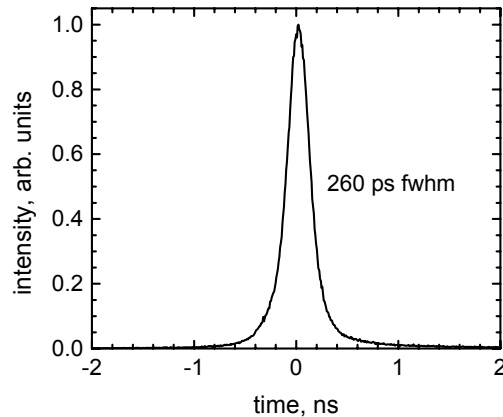


Figure 5. Timing resolution spectrum measured for a LaBr₃:Ce (5% Ce³⁺) crystal in coincidence with a BaF₂ crystal.

Similar measurements were also made with LaBr₃:Ce crystals having 0.2%, 0.5%, and 1.3% Ce³⁺ concentrations placed in the “stop” channel, and the coincidence timing resolution was measured to be 450 ns, 390 ns, and 320 ps (FWHM), respectively. The timing resolution for two BaF₂ detectors in coincidence with each other was measured to be 240 ps (FWHM) in this study. Overall, these results confirm that LaBr₃:Ce is well suited for applications requiring fast response, high count-rates, and good timing resolution.

3.4.5 Proportionality of Response

We have evaluated the proportionality of response (or linearity) of LaBr₃:Ce scintillators. Non-proportionality (as a function of energy) in light yield can be one of the important reasons for degradation in energy resolution of established scintillators such as NaI(Tl) and CsI(Tl) [Dorenbos 95]. As a result, we have measured light output of LaBr₃:Ce under excitation from isotopes such as ²⁴¹Am (60 keV γ -rays), ⁵⁷Co (122 keV γ -rays), ²²Na (511 keV and 1275 keV γ -rays) and ¹³⁷Cs (662 keV γ -rays). A LaBr₃:Ce crystal (0.5% Ce) was wrapped in Teflon tape and coupled to a PMT. Pulse height measurements were performed using standard NIM equipment with the scintillator exposed to different isotopes. Same settings were used for PMT and pulse processing electronics for each isotope. From the measured peak position and the known γ -ray energy for each isotope, the light output (in photons/MeV) at each γ -ray energy was estimated. The data points were then normalized with respect to the light output value at 662 keV energy and the results (shown in **Figure 6**) indicate that LaBr₃:Ce is a very proportional scintillator. Over the energy range from 60 to 1275 keV, the non-proportionality in light yield is about 6%

for LaBr₃:Ce, which is substantially better than that for many established scintillators. For example, over the same energy range, the non-proportionality is about 35% for LSO and about 20% for NaI(Tl) and CsI(Tl) [Guillot-Noel]. The higher proportionality of LaBr₃:Ce is one of the important reasons (in conjunction with its high light output) behind the high energy resolution of this scintillator.

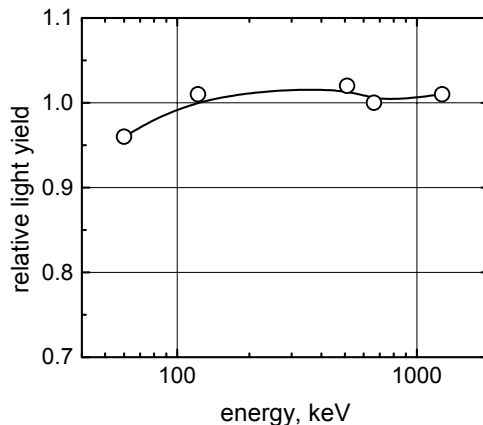


Figure 6. Proportionality in light yield as a function of γ -ray energy measured for LaBr₃:Ce at room temperature.

Overall, these measurements clearly indicate that LaBr₃:Ce is a promising scintillator. It has high light output, fast response and shows good energy and timing resolution. Our studies indicate that these properties are maintained as the crystal volume is increased.

3.4.6 Exploration of Scintillation Properties of LaBr₃ with higher Ce³⁺ Concentration

The trends observed in **Figure 4** and **Table 1** clearly indicate that the temporal response of LaBr₃:Ce becomes faster as the Ce³⁺ concentration in the crystals is increased. Due to this improvement in the temporal response, the coincidence timing resolution of LaBr₃:Ce also improved at the higher Ce³⁺ concentration. In view of this observation, the investigation of scintillation properties of LaBr₃:Ce was continued by growing a new set of crystals with varying Ce³⁺ concentrations (0.5%, 5%, 10%, 20% and 30%, on molar basis). Bridgman method was used to grow these crystals. Light output, emission spectra, and decay time spectra were measured for these crystals (≤ 1 cm³ size) using techniques described in *sections 3.4.1 to 3.4.3*.

The peak emission wavelength showed only slight variation over the entire Ce³⁺ concentration range that was investigated. A slight shift (of ~ 10 nm) towards longer wavelengths was observed for LaBr₃ samples with higher Ce³⁺ concentrations (20 and 30%).

Light output of these newer LaBr₃ samples with wider range of Ce³⁺ concentration was measured by coupling them (unpacked and wrapped in Teflon tape) to a photomultiplier tube (Hamamatsu R2059) and acquiring ¹³⁷Cs pulse height spectra (662 keV gamma-rays). Based on the calibration provided by a BGO crystal, the light output was estimated for various LaBr₃:Ce crystals. The highest light output was recorded for LaBr₃:Ce crystal with 5% Ce in this study and its light output was 70,500 photons/MeV (see **Table 2**). This light output is higher than the value reported in **Table 1**, most likely due to higher crystal quality and crystal processing. The light output of this new batch of LaBr₃ crystals with varying Ce³⁺ concentration (0.5, 5, 10, 20

and 30%) is reported in **Table 2**. As seen in **Table 2**, the light output does not change appreciably with Ce^{3+} concentration and the overall variation in light output over the Ce^{3+} concentration range from 0.5 to 30% is less than 10%.

TABLE II
SCINTILLATION PROPERTIES OF $\text{LaBr}_3\text{:Ce}$ WITH DIFFERENT Ce^{3+}
CONCENTRATIONS (0.5 TO 30% RANGE)

Ce^{3+} Concentration (%)	Light Output (Photons/MeV)	Rise Time (ns)	Decay Times (ns)
0.5	70,100	5	26 ns (92%), 66 ns (8%)
5	70,500	0.9	16 ns (97%), 63 ns (3%)
10	64,500	0.5	16 ns (94%), 55 ns (6%)
20	64,000	0.16	17 ns (95%), 70 ns (5%)
30	69,000	0.2	18.6 ns (97%), 70 ns (3%)

Temporal response of LaBr_3 samples with Ce^{3+} concentration in 0.5 to 30% range was measured using the delayed coincidence method at the LBNL Pulsed X-ray Facility. **Figure 7** shows the temporal response curves for each LaBr_3 sample. Each curve was fitted with a sum of exponentials (rise and decay components) and a time-independent background. **Table 2** provides the fit results, which indicates that while at Ce^{3+} concentrations above 5%, the effective decay time does not improve, the effective risetime continues to become faster at higher Ce^{3+} concentrations. As a result, $\text{LaBr}_3\text{:Ce}$ with higher Ce^{3+} concentration (20 to 30% range) can be expected to provide better performance in applications that require fast timing. The relationship between risetime and Ce^{3+} concentration can be explained using a diffusion model (of self trapped holes or excitons, STH or STE), where the transfer rate ($1/\tau$) is proportional to the activator concentration [Glodo].

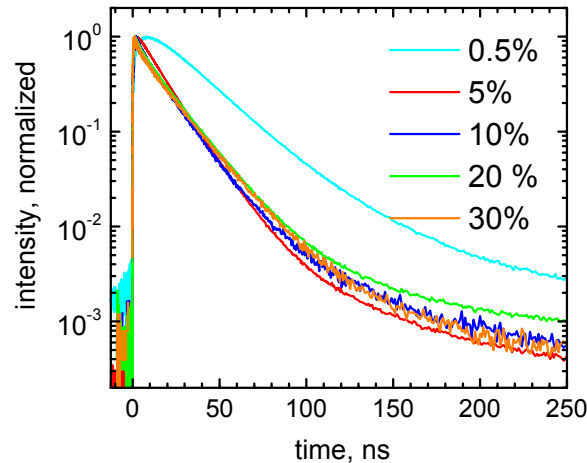


Figure 7. Temporal response of $\text{LaBr}_3\text{:Ce}$ crystals with varying Ce^{3+} concentration.

Coincidence timing resolution of $\text{LaBr}_3\text{:Ce}$ crystals with various Ce^{3+} concentrations in 0.5 to 30% range, operating in coincidence with BaF_2 crystal (1 cm^3 in size) has been measured

using the approach discussed earlier in *section 3.4.4*. The BaF₂ detector formed the “start” channel in the timing setup, while the LaBr₃:Ce detector formed the “stop” channel. Lower level energy threshold of about 250 keV was used for both channels. **Figure 8** shows the coincidence timing resolution results, measured in this manner. Excellent timing resolution of 165 ps (FWHM) was measured for LaBr₃ sample with 30% Ce doping. The timing resolution improves at higher Ce³⁺ concentrations. Since the light output and decay time do not change much at Ce³⁺ doping level above 5%, the improvement in timing resolution can be explained on the basis of the improvement in risetime at higher Ce³⁺ concentrations.

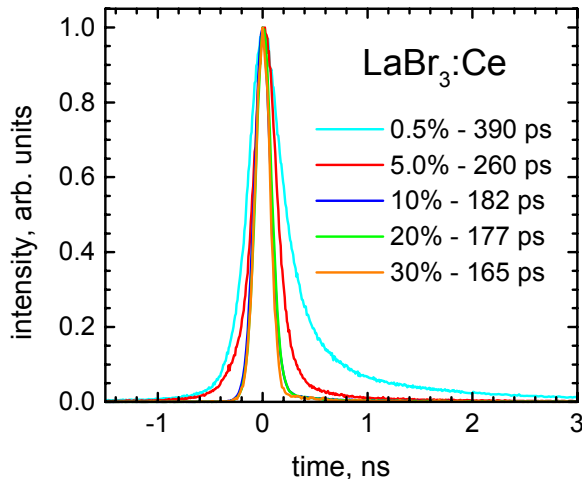


Figure 8. Coincidence timing resolution of LaBr₃ crystals with varying Ce³⁺ concentration.

Overall, these results indicate that LaBr₃ crystals with higher Ce³⁺ concentrations (≥ 5 ns) appear to be promising for fast timing studies including time-of-flight PET. Particularly encouraging is the potential of LaBr₃:Ce to provide timing resolution similar to or better than BaF₂ along with high energy resolution.

3.5 ENERGY RESOLUTION OF LaBr₃:Ce

3.5.1. Energy Resolution Results

Gamma ray spectroscopy has also been performed with LaBr₃:Ce crystals by coupling them to a PMT. The scintillator (1 cm³ in size, 0.5% Ce³⁺) was irradiated with ¹³⁷Cs source (662 keV photons) and the resulting spectrum is shown in **Figure 9**. The energy resolution of the 662 keV photopeak was measured to be 3% FWHM at room temperature. Such high energy resolution has never been achieved with any of the established inorganic scintillators (even in small sizes) at room temperature. **Figure 9** also shows a ¹³⁷Cs spectrum recorded with NaI(Tl). Energy resolution of NaI(Tl) crystal was measured to be 6.7% (FWHM). Thus, the energy resolution of LaBr₃:Ce is ~2 times better than that for typical NaI(Tl) detectors. Higher light output and proportionality of LaBr₃:Ce (compared to NaI(Tl) and other inorganic scintillators) are responsible for high energy resolution obtained with those crystals. It is important to note that energy resolution of LaBr₃:Ce at 662 keV gamma ray energy approaches that of room temperature semiconductor detectors such as CdTe and CdZnTe. Energy spectra of ²²Na and

^{57}Co isotopic sources with the same $\text{LaBr}_3\text{:Ce}$ crystal coupled to a PMT at room temperature are shown in **Figure 10**. The energy resolution of 511 keV photopeak (^{22}Na source) was measured to be 3.5% (FWHM) and that of 122 keV photopeak (^{57}Co source) was measured to be 7% (FWHM).

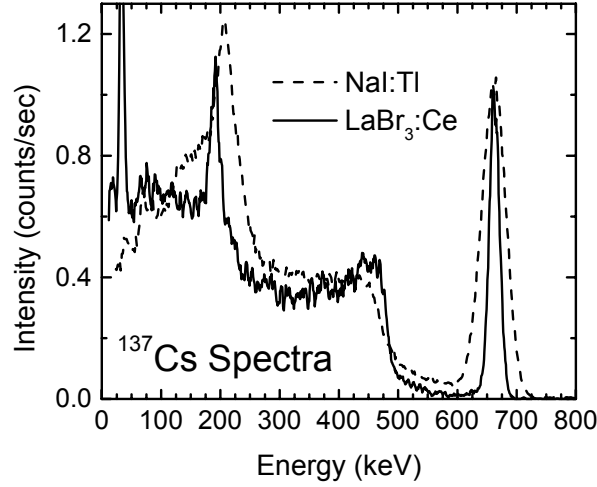


Figure 9. ^{137}Cs energy spectra recorded with a $\text{LaBr}_3\text{:Ce}$ scintillator prepared at RMD and a commercial NaI(Tl) scintillator. The 662 keV peak energy resolution is 3% (FWHM) for $\text{LaBr}_3\text{:Ce}$ and 6.7% (FWHM) for NaI(Tl) at room temperature. A PMT was used to read-out both scintillators.

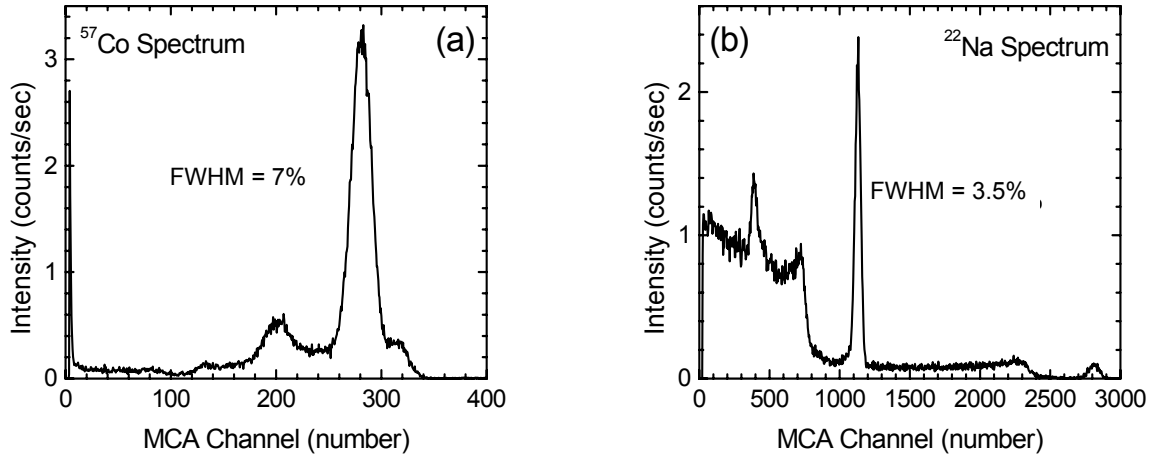


Figure 10. Energy spectra of ^{57}Co and ^{22}Na isotopes collected with a $\text{LaBr}_3\text{:Ce}$ crystal coupled to a PMT. Left panel shows ^{57}Co energy spectrum with the energy resolution of 122 keV peak at 7% (FWHM). Right panel shows ^{22}Na spectrum with the energy resolution of 511 keV photopeak at 3.5% (FWHM).

$\text{LaBr}_3\text{:Ce}$ crystals have also been coupled to RMD's standard, deep-diffused silicon avalanche photodiode (APD, $8 \times 8 \text{ mm}^2$ area) and their energy resolution characteristics have been measured. The APD was cooled to 250 °K in this study in order to minimize dark current and

noise. **Figure 11** shows ^{137}Cs (662 keV photons) and ^{57}Co (122 keV photons) spectra recorded with a $\text{LaBr}_3:\text{Ce}$ crystal ($\sim 1 \text{ cm}^3$ size, 0.5% Ce concentration). The energy resolution of the 662 keV peak is 2.7% (FWHM) while that of 122 keV peak is 7% (FWHM).

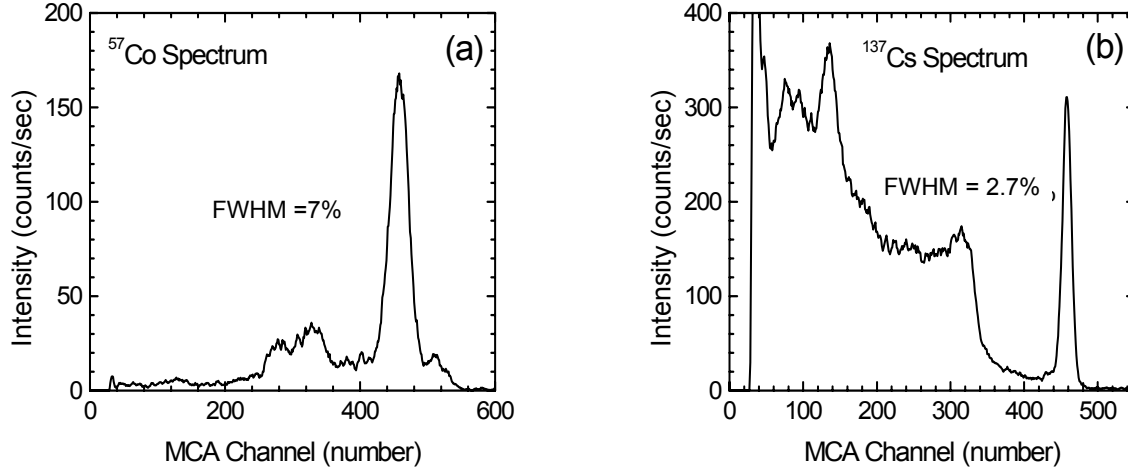


Figure 11. ^{57}Co (left) and ^{137}Cs (right) spectra recorded with a $\text{LaBr}_3:\text{Ce}$ scintillator coupled to a silicon APD at 250 K.

3.5.2. Analysis of 662 keV Energy Resolution:

Using the measured 662 keV energy resolution and noise for LaBr_3 readout with different photodetectors (see **Figures 9 & 11**), an analysis was performed on the various parameters that influence the measured energy resolution. Adapting the framework developed by *van Eijk et. al.*, the overall energy resolution for a scintillation detector can be expressed as [van Eijk]:

$$(\Delta E/E)^2 = R^2 = R_{phe}^2 + R_{sci}^2 + R_{noise}^2 \quad (1)$$

R_{phe} represents the resolution broadening due to the photoelectron statistics (including the excess noise effects, arising from the variance in the photodetector gain). R_{sci} represents broadening effects due to non-ideal nature of scintillators. This parameter includes contribution of effects such as inhomogeneities and nonproportionality. Finally, the electronic noise effects in the scintillation detection system are included in the final term, R_{noise} . For PMT readout, the last term, R_{noise} can be ignored due to PMT's negligible electronic noise contribution, though R_{noise} has to be included in case of APDs. It is possible to estimate the contribution of the first term, R_{phe} , by estimating the number of photoelectrons (N_{phe}) generated in the photodetector for a gamma-ray event in the scintillator. N_{phe} can be estimated using the following expression:

$$N_{phe} \approx N_{ph} \bullet E_\gamma \bullet \eta_{det} \quad (2)$$

where, N_{ph} is the light output of the scintillator (in photons/MeV), which is 70,100 photons/MeV for $\text{LaBr}_3:\text{Ce}$ (as shown in **Table 2**), E_γ is energy of the incident gamma-ray in MeV (0.662 in this case) and η_{det} is the quantum efficiency of the photodetector over the emission spectrum of the scintillator (including the light collection efficiency). Once N_{phe} is known, the resolution broadening due to R_{phe} , representing variance in photoelectron statistics, can be estimated using the traditional Poisson distribution:

$$R_{phe}^2 = (2.36)^2 [ENF/N_{phe}] \quad (3)$$

where, ENF is the excess noise factor of the photodetector (~ 1.15 for PMTs and ~ 2 for deep-diffused APDs). Using this framework, it is possible to estimate N_{phe} and R_{phe} from the known parameters of the scintillator and the photodetectors using equations (2) and (3). Then using the measured values of R_{noise} and R (or $\Delta E/E$), R_{sci} can be back calculated using equation (1). Using this framework, the 662 keV energy resolution of various spectrometers such as NaI(Tl)-PMT, LaBr₃:Ce-PMT and LaBr₃:Ce-APD (see **Figures 9 and 11**) was analyzed and the results are presented in **Table III**.

TABLE III
ANALYSIS OF THE 662 keV ENERGY RESOLUTION OF SCINTILLATOR SPECTROMETERS

Detector	N_{phe} at 662 keV (electrons)	R (%) FWHM	R_{phe} (%) FWHM	R_{sci} (%) FWHM	R_{noise} (%) FWHM
NaI(Tl)-PMT ^a	6,000	6.7	3.2	5.9	0
LaBr ₃ :Ce-PMT ^a	10,670	3	2.4	1.8	0
LaBr ₃ :Ce-Si APD ^b	32,500	2.7	1.9	1.8	0.6

a-room temperature b-cooled to 250 °K

The overall energy resolution R at 662 keV energy was measured to be 6.7% (FWHM) for NaI(Tl) coupled to PMT (as shown in **Figure 9**), while R_{phe} was estimated to be 3.2% (FWHM) using equation (3). R_{sci} was then calculated to be 5.9% (FWHM) from equation (1) by assuming that R_{noise} is negligible for PMT readout. Similar analysis of a LaBr₃:Ce crystal coupled to a PMT has been performed and the results are listed in **Table III**. As shown in **Figure 9**, the energy resolution, R , of LaBr₃:Ce readout with a PMT at 662 keV was measured to be 3% (FWHM). R_{phe} for LaBr₃-PMT detector was calculated from known values of light output (70,100 photons/MeV), the incident γ -ray energy (662 keV) and the PMT quantum efficiency at 360 nm (~ 0.23) to be 2.4% (FWHM). R_{sci} was then estimated to be 1.8% (FWHM). This study illustrates that photoelectron statistics (or R_{phe}) is the main broadening component for LaBr₃:Ce, while non-ideal nature of the scintillator (or R_{sci}) is the dominant component for NaI(Tl) when a PMT is used as an optical detector.

In addition to evaluation of LaBr₃:Ce crystals with PMTs, we have also performed energy resolution measurements with LaBr₃:Ce crystals coupled to an APD as shown in **Figure 11**. The energy resolution of 662 keV photopeak (¹³⁷Cs source) for a LaBr₃:Ce crystal read out by an APD is about 2.7% (FWHM) at 250 °K. The main reason for improvement in the energy resolution obtained with LaBr₃:Ce upon use of an APD for optical readout is its higher quantum efficiency compared to a standard bialkali PMT (by a factor of three) [McClish]. This leads to significant increase in the number of photoelectrons (N_{phe}) produced with Si-diodes as compared to PMTs. We have analyzed the 662 keV spectrum recorded with a LaBr₃:Ce scintillator coupled to an APD using equations (1) to (3) and the results are presented in **Table III**.

The component R_{phe} , which is the dominant one for LaBr₃:Ce and is governed by the photoelectron statistics can be calculated to be about 1.9% (FWHM) for 662 keV interaction in a LaBr₃:Ce crystal coupled to an APD, which compares favorably with R_{phe} of 2.4% (FWHM) estimated for similar gamma ray interaction in LaBr₃:Ce coupled to PMT (see **Table III**). Assuming that the component R_{sci} remains constant for a given LaBr₃:Ce crystal when measured with APDs and PMTs, R_{sci} should be 1.8% (FWHM) for 662 keV gamma-ray interaction in LaBr₃:Ce coupled to an APD. The contribution of the APD noise R_{noise} can then be calculated using (1) to be 0.6% (FWHM) for the 662 keV spectrum shown in **Figure 11** where the overall 662 keV peak resolution is 2.7% (FWHM). It is important to note that the APD was cooled to

250 K in this study to reduce its noise and subsequent measurements of electronic noise, performed by injecting an electronic test pulse in the detection system confirmed that this noise estimation was reasonably accurate [Shah 08].

Ultimately, the choice of the photodetector to be used with LaBr₃:Ce crystals will depend on the demands of the particular experiment. PMTs would be chosen to achieve highest possible energy resolution at room temperature, while in experiments where moderate cooling is acceptable, traditional silicon photodiodes would provide better results. Energy resolution measurements performed using LaBr₃:Ce crystals with 5% Ce³⁺ concentration are similar to those shown in **Figures 9-11**.

3.6 SUMMARY

In our research, we have investigated a relatively new scintillation material, LaBr₃:Ce, for γ -ray detection. Our research concentrated on growth of high quality LaBr₃:Ce crystals using Bridgman method, as well as extensive characterization of the physical, optical, and scintillation properties of these crystals. Overall, these measurements indicate that LaBr₃:Ce is a promising scintillator. It has high light output, fast response and shows good energy and timing resolution. Based on successful performance as gamma ray detector, this new scintillation material can be applied to applications such as medical imaging, nuclear physics, X-ray diffraction, non-destructive evaluation, treaty verification and non-proliferation monitoring, environmental cleaning, and geological exploration. Particularly encouraging is the combination of excellent energy and timing resolution that is provided by LaBr₃:Ce, which makes it attractive for PET studies including time-of-flight PET.

3.7 CURRENT STATUS OF LaBr₃:Ce

The potential of LaBr₃:Ce was clear ever since its discovery at the Delft University of Technology [van Loef 2001] and Saint Gobain Crystals and Detectors (SGC) has been active in commercial production of this material. Initial efforts at SGC focused on producing LaBr₃ with 0.5% Ce doping level. However, the doping level of Ce in LaBr₃ was increased subsequently to 5%, partly based on the results presented here (**Figure 4** and **Table I**) [Mayhugh], which show that when the Ce-doping level is increased to 5%, both the rise-time as well as the decay time are faster without any significant loss in light yield, allowing significant improvement in the timing resolution. Much of the commercial production of LaBr₃ at SGC is now with 5% Ce doping level. Due to LaBr₃'s highly anisotropic crystal structure [Menge], growth of large LaBr₃ crystals has been challenging, though 3" diameter crystals are now being produced at SGC. LaBr₃ (5% Ce doping) crystals produced by SGC are marketed under the trade name of *Brilliance 380*.

Detailed evaluation of LaBr₃ (5% Ce) crystals for time-of-flight PET imaging is being performed at the University of Pennsylvania (U-Penn) by Dr. Joel Karp's team [Karp 08]. Initial evaluation at U-Penn was performed using direct coupling of *Brilliance 380* crystal (4x4x5 mm³) to a PMT (Hamamatsu R4998) to maximize light collection and energy resolution of 4% (FWHM) and timing resolution of 145 ps (FWHM) were achieved for 511 keV gamma-rays [Karp 08]. Next, a PET module based on a 10x10 array of *Brilliance 380* (4x4x30 mm elements) coupled to a 7-element PMT array (Photonis XP20D0) with light guide between the scintillator and PMT arrays was built at U-Penn. For this detector module, energy resolution of 5.1%

(FWHM) and timing resolution of 315 ps (FWHM) were achieved [Karp 08]. For implementation of clinical PET scanner with TOF capability based on $\text{LaBr}_3\text{:Ce}$, Dr. Karp's team has assembled PET modules consisting of 1620 $\text{LaBr}_3\text{:Ce}$ pixels, each with 4x4x30 mm size. This $\text{LaBr}_3\text{:Ce}$ array is readout using an array of 24 PMTs (Photonis XP20D0) with light guide between PMTs and $\text{LaBr}_3\text{:Ce}$ elements. Using such a module design, U-Penn team has assembled a "LaPET Scanner" which consists of 24 such modules (see **Figure 12**). The average timing resolution across the 24 modules of this scanner is 375 ps (FWHM) and the average energy resolution at 511 keV is 7% (FWHM). Phantom measurements conducted with this scanner confirm improvements in lesion contrast and detectability with TOF [Karp 08]. U-Penn team in collaboration with Saint Gobain and RMD is planning evaluation of LaBr_3 crystals and arrays with 30% Ce doping for next generation TOF studies.

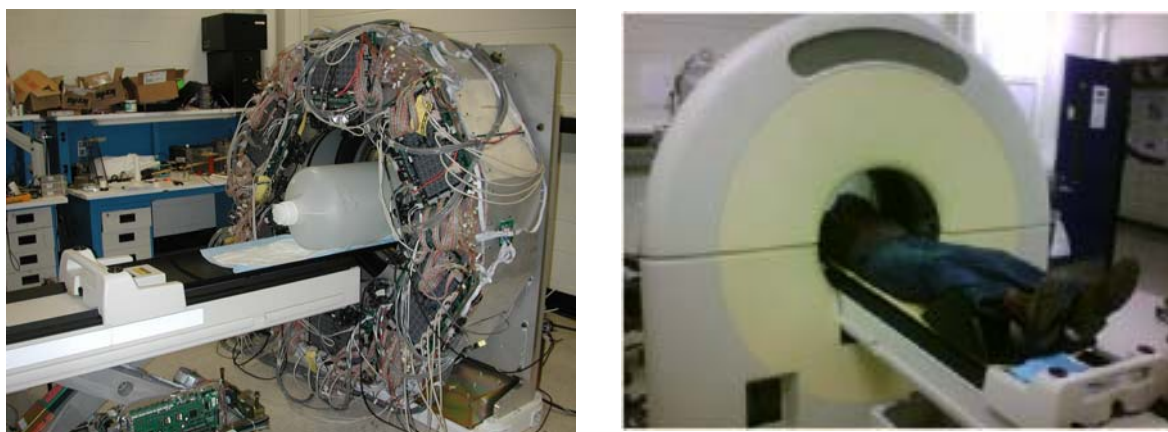


Figure 12. Photographs of U-Penn's "LaPET scanner".

3.8 REFERENCES

- L. M. Bollinger and G. E. Thomas, "Measurement of the time dependence of scintillation intensity by a delayed-coincidence method", *Rev. Sci. Instr.*, vol. 32, p. 1044, (1961).
- J. C. Brice, **Crystal Growth Processes**, UK: Blackie Halsted Press, (1986).
- P. Dorenbos, J. T. M. de Haas, and C. W. E. van Eijk, "Non-proportionality in the scintillation response and the energy resolution obtainable with scintillation crystals", *IEEE Trans. Nucl. Sci.*, vol 42, no. 6, pp. 2190-2202, Dec. (1995).
- P. Dorenbos, *Light output and energy resolution of Ce^{3+} doped scintillators*, Nucl. Instr. and Meth., V. 486, p. 208, (2002).
- J. Glodo, W.W. Moses, W.M. Higgins, E.V.D. van Loef, P. Wong, S.E. Derenzo, M.J. Weber, K.S. Shah, Effect of Ce Concentration on Scintillation Properties of $\text{LaBr}_3\text{:Ce}$, *IEEE Trans. Nuc. Sci.*, V(52), pp. 1805-1808, (2004).
- O. Guillot-Noël, J. C. van't Spijker, J. T. M. de Haas, P. Dorenbos, C. W. E. van Eijk, K. Krämer, and H. U. Güdel, "Scintillation Properties of $\text{RbGd}_2\text{Br}_7\text{:Ce}$ Advantages and Limitations", *IEEE Trans. Nuc. Sci.*, vol. 46, no. 5, pp. 1274-1284, (1999).
- Joel S. Karp, Margaret E. Daube-Witherspoon, Suleman Surti, Amy E. Perkins¹, Chris C.M. Kyba, Mathew E. Werner, Time-of-flight Imaging Performance of a Lanthanum Bromide

- PET Scanner, Presented at the World Molecular Imaging Congress, September 10-13, (2008).
- K. Kleinknecht, **Detectors for Particle Radiation**, 2nd Edition, Cambridge University Press, Cambridge, U.K. (1998).
- G. Knoll, **Radiation Detection and Measurement** (3rd ed.), New York: John Wiley and Sons, Inc., (1999).
- M. Mayhugh, Saint Gobain Crystals and Detectors, Private Communication, June, (2009).
- M. McClish, R. Farrell, K. Vanderpuye, and K.S. Shah, "A Reexamination of Deep Diffused Silicon Avalanche Photodiode Gain and Quantum Efficiency," *IEEE Trans. Nuc. Sci.*, vol. 53, no. 5, pp. 3049-3054 Oct. (2006).
- P. Menge, Performance of Large BriLanCe 380 (lanthanum bromide) scintillators, Presented at SORMA XI, Ann Arbor, MI, May (2006).
- W. Mengesha, T. D. Taulbee, B. D. Rooney, and J. D. Valentine, "Light yield nonproportionality of CsI(Tl), CsI(Na), and YAP," *IEEE Trans. Nucl. Sci.*, vol. 45, pp. 456-461, 1998.
- W.W. Moses, *Current trends in scintillator detector and materials*, Nucl. Inst. and Meth. A-487, pp. 123-128, (2002).
- K. S. Shah, J. Glodo, M. Klugerman, W. W. Moses, S. E. Derenzo, and M. J. Weber, "LaBr₃:Ce Scintillators for Gamma Ray Spectroscopy", *IEEE Trans. Nucl. Sci.* V50(6), pp. 2410-2413, (2003).
- K.S. Shah, High Quantum Efficiency, Fast Detectors for the Readout of Scintillators for Gamma-Ray Detection, DNDO SBIR Phase I Final Report, Grant Number HSHQDC-07-C-00042, Jan, (2008)
- E. V. D. van Loef, P. Dorenbos, C. W. E. van Eijk, K. Krämer, and H. U. Güdel, "High-Energy-Resolution Scintillator: Ce³⁺ Activated LaBr₃", *Appl. Phys. Lett.*, vol. 79, no. 10, pp.1573-1575, (2001).
- C. W. E. van Eijk, P. Dorenbos, E. V. D. van Loef, K. Krämer, H. U. Güdel, "Energy resolution of some new inorganic-scintillator gamma-ray detectors", *Radiation Measurements*, vol. 33, pp. 521-525, (2001).

CHAPTER 4: CERIUM BROMIDE SCINTILLATORS

4.1 OVERVIEW

This chapter covers investigation of cerium bromide scintillators. This chapter is adapted from the following publication: *K.S. Shah et. al., CeBr₃ scintillators for gamma-ray spectroscopy, IEEE Transactions on Nuclear Science V. 52(6), (2005)*. This publication covers investigation of some of the basic scintillation properties of CeBr₃. Additional results covering energy and timing resolution studies of CeBr₃ scintillators as well as scintillation properties of mixed cerium halides, which were not available at the time of submitting the publication listed above are included here. Analysis of the energy resolution of CeBr₃ scintillators read out with photomultiplier tubes is included in this chapter.

4.2. INTRODUCTION

Scintillation spectrometers are widely used in detection and spectroscopy of energetic photons (X-rays and γ -rays) at room temperature. These detectors are commonly used in nuclear and particle physics research, medical imaging, diffraction, non destructive testing, nuclear treaty verification and safeguards, nuclear non-proliferation monitoring, and geological exploration [Knoll, Kleinknecht].

Important requirements for the scintillation crystals used in these applications include high light output, high stopping efficiency, fast response, good proportionality, low cost and availability in large volume. These requirements cannot be met by any of the commercially available scintillators. As a result, there is continued interest in search for new scintillators with enhanced performance [Derenzo, van Eijk, Lecoq, Moses].

In this chapter, properties of a new scintillator, cerium bromide (CeBr₃), are discussed. In this material, Ce³⁺ is an intrinsic constituent as well as a luminescence center for the scintillation process. The γ -ray stopping efficiency of CeBr₃ is significantly higher than that of NaI(Tl), the most common scintillation detector. In our investigation, small crystals of CeBr₃ have been grown using the Bridgman process and their scintillation properties have been characterized. High light output, good proportionality, fast response and excellent energy and timing resolution have been measured for small CeBr₃ crystals. Based on the results, CeBr₃ is very promising for γ -ray spectroscopy and its properties are very similar to those of another recently discovered scintillator, cerium doped lanthanum bromide (LaBr₃:Ce) [van Loef].

4.3. CRYSTAL GROWTH OF CeBr₃

CeBr₃ has hexagonal crystal structure and its density is 5.2 g/cm³. The compound melts congruently at 722 °C and therefore its crystals can be grown using melt based methods such as Bridgman and Czochralski. This is fortunate because these melt-based processes are well suited for growth of large volume crystals [Brice]. In our research, we have used Bridgman method for growing CeBr₃ crystals because this technique is easy to implement, and can provide good indication of the feasibility of producing high quality crystals of CeBr₃ from the melt. Ultra-dry CeBr₃ was used with 99.99% purity. A two zone Bridgman furnace was used with temperature in the hotter zone above the melting point CeBr₃ (722 °C) and that of the cooler zone less than 722 °C. CeBr₃ crystals (<1 cm³) were grown in quartz ampoules using the Bridgman method. Small sections were cut from the solid ingots and polished using non aqueous slurries (due to

hygroscopic nature of CeBr_3) prepared by mixing mineral oil with Al_2O_3 grit. Some crystals were then packaged to prevent long exposure to moisture.

4.4. SCINTILLATION PROPERTIES OF CeBr_3

Scintillation properties of small Bridgman grown CeBr_3 crystals ($\leq 0.3 \text{ cm}^3$) have been characterized. This investigation involved measurement of the light output, the emission spectrum, and the fluorescent decay time of the crystals. Energy and timing resolution of CeBr_3 crystals and their proportionality of response were also measured.

4.4.1 Light Output and Energy Resolution

The light output of CeBr_3 crystals was measured by comparing their response to 662 keV γ -rays (^{137}Cs source) to the response of a calibrated BGO scintillator to the same isotope (see **Figure 1**). This measurement involved optical coupling of a CeBr_3 crystal to a photomultiplier tube (with multi-alkali S-20 photocathode), irradiating the scintillator with 662 keV photons and recording the resulting pulse height spectrum. In order to maximize light collection, the CeBr_3 crystal was wrapped in reflective, white Teflon tape on all faces (except the one coupled to PMT). An index matching silicone fluid was also used at the PMT-scintillator interface. A pulse height spectrum was recorded with a CeBr_3 crystal. This experiment was then repeated with a calibrated BGO scintillator. Comparison of the photopeak position obtained with CeBr_3 for 662 keV photon energy to that with BGO provided estimation of light output for the CeBr_3 crystal.

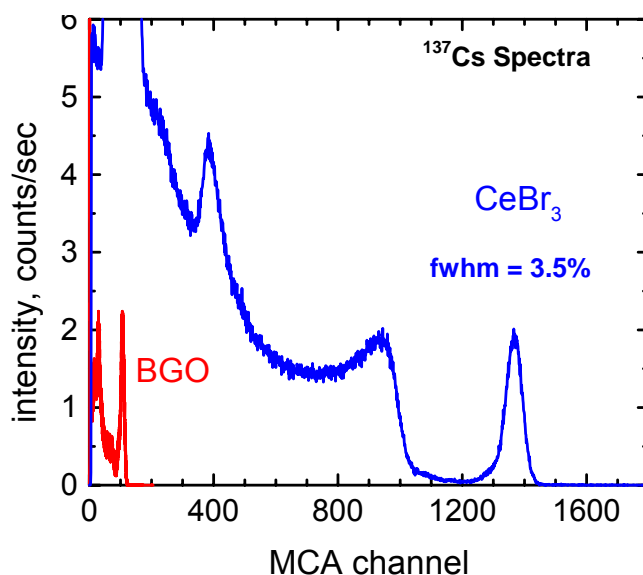


Figure 1. ^{137}Cs spectra collected with CeBr_3 and BGO crystals coupled to PMT. The light output of CeBr_3 has been estimated to be $\sim 68,000$ photons/MeV. The energy resolution of 662 keV peak for CeBr_3 is 3.4% (FWHM) at room temperature.

Figure 1 shows pulse height spectra for both CeBr_3 and BGO under ^{137}Cs irradiation and amplifier shaping time of 4.0 μsec . This shaping time is long enough to allow full light collection from both the scintillators. The PMT bias and amplifier gain were same for both spectra. Based on the recorded photopeak positions for CeBr_3 and BGO, and by taking into account the photocathode quantum efficiency for BGO and CeBr_3 , we estimated light output of

CeBr₃ crystal to be about 68,000 photons/MeV. This light output is amongst the highest values for inorganic scintillators [Knoll, Rodyni].

The energy resolution of the 662 keV photopeak recorded with CeBr₃ scintillator has been measured to be ~3.5% (FWHM) at room temperature as shown in **Figure 1**, which is substantially better than the energy resolution of 6-7% (FWHM) at 662 keV obtained with established scintillators such as NaI(Tl) and CsI(Tl). The energy resolution of CeBr₃ crystals at 662 keV approaches that of room temperature semiconductor detectors such as CdTe and CdZnTe (2-3% FWHM at 662 keV).

4.4.2 Emission Spectrum

We have measured the emission spectrum of the CeBr₃ scintillators. The CeBr₃ samples were excited with radiation from a Philips X-ray tube having a Cu target, with power settings of 30 kVp and 15 mA. The scintillation light was passed through a McPherson monochromator and detected by a Hamamatsu R2059 photomultiplier tube with a quartz window. The system was calibrated with a standard light source to enable correction for sensitivity variations as a function of wavelength. A normalized emission spectrum for a CeBr₃ sample is shown in **Figure 2**. The peak emission wavelength for the CeBr₃ sample is at ~370 nm and this emission is anticipated to be due to 5d→4f transition of Ce³⁺. The peak emission wavelength of 370 nm for CeBr₃ is attractive for gamma ray spectroscopy because it matches well with the spectral response of the photomultiplier tubes as well as new generation of silicon photodiodes.

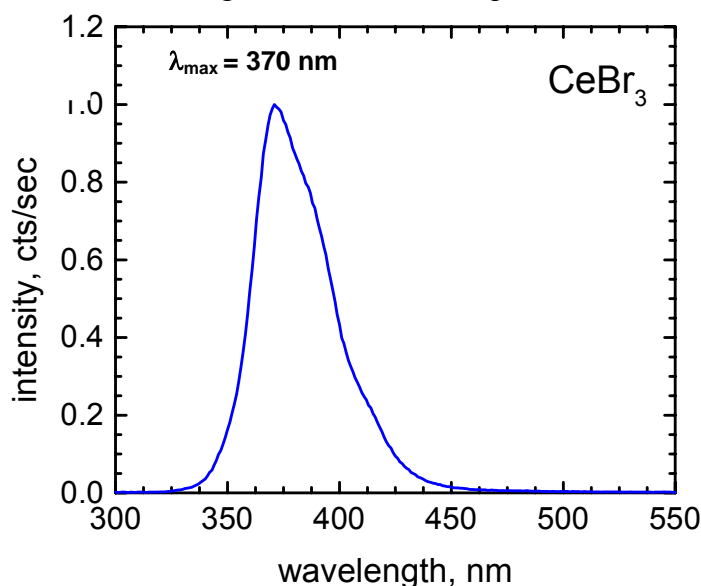


Figure 2. Optical emission spectrum for a CeBr₃ scintillator upon exposure to X-rays.

4.4.3 Decay Time

Decay-time spectrum of a CeBr₃ crystal has been measured using the delayed coincidence method [Bollinger]. **Figure 3** shows the decay-time spectrum recorded for a CeBr₃ sample along with a theoretical fit (with an exponential rise and decay time plus background) to the data. The risetime of the scintillation pulse is <0.5 ns, while the decay constant is 17 ns and this component covers almost all of the integrated light output of the sample. This decay component can be

attributed to optical emission arising from direct capture of electron-hole pairs at the Ce^{3+} sites. The risetime of the scintillation pulse from CeBr_3 has been estimated to be ~ 0.1 ns using the data shown in **Figure 3**. The *initial photon intensity*, a figure of merit for timing applications, has been estimated to be $\sim 4,000$ photons/(ns-MeV) for CeBr_3 , which is higher compared to all common inorganic scintillators (including BaF_2 , a benchmark for timing applications).

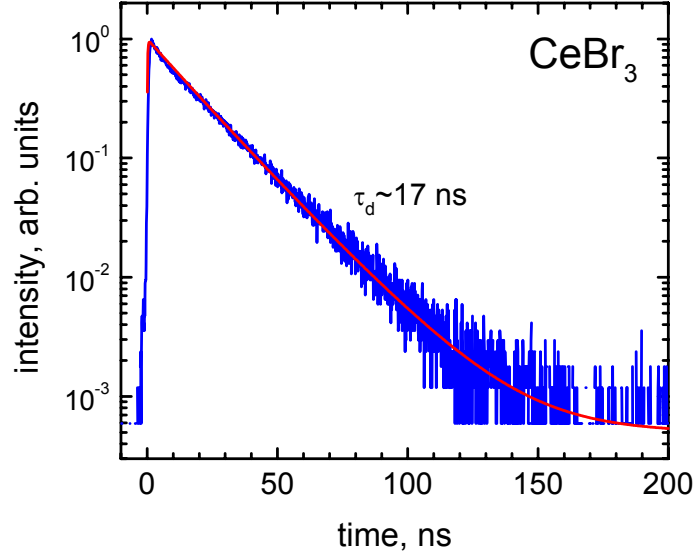


Figure 3. Decay-time spectrum for CeBr_3 scintillator.

4.4.4 Coincidence Timing Resolution

Coincidence timing resolution of CeBr_3 crystals has been measured as shown in **Figure 4**. This experiment involved irradiating a BaF_2 and a CeBr_3 scintillator, each coupled to a fast PMT (Hamamatsu R5320) with 511 keV positron annihilation γ -ray pairs (emitted by a ^{22}Na source).

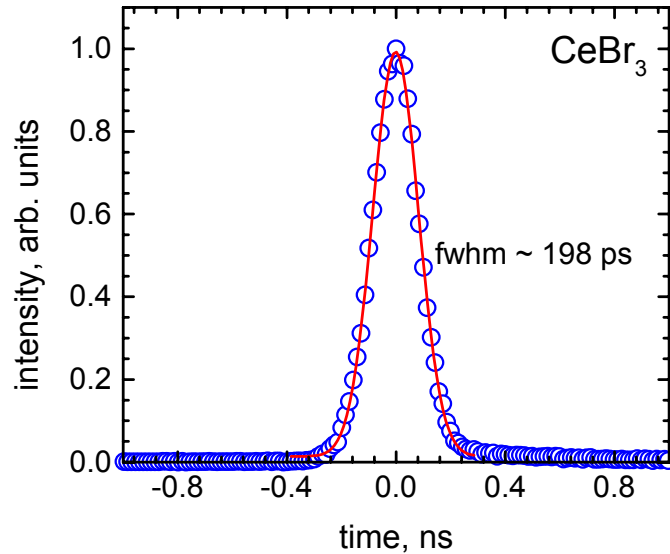


Figure 5. Timing resolution for CeBr_3 and BaF_2 crystals in coincidence. For two BaF_2 crystals in coincidence, the timing resolution with the same setup was 210 ps (fwhm).

The BaF₂-PMT detector formed a “start” channel in the timing circuit, while the CeBr₃-PMT detector formed the “stop” channel. The signal from each detector was processed using two channels of a Tennelec TC-454 CFD that had been modified for use with the MCP-PMTs. The time difference between the start and stop signals was digitized with a Tennelec TC-862 TAC and a 16-bit ADC, resulting in a TDC with 7.5 ps per bin resolution. Data were accumulated until the coincidence timing distribution had approximately 10,000 counts in the maximum bin.

Figure 4 shows a coincidence timing resolution plot acquired in this manner with CeBr₃ and BaF₂ crystals and the timing resolution was measured to be <200 ps (FWHM). Using the same setup, the timing resolution of two BaF₂ crystals in coincidence was measured to be 210 ps (FWHM). These results confirm that CeBr₃ is well suited for applications requiring fast response, high count-rates, and good timing resolution. Based on its high timing resolution, CeBr₃ scintillators can be expected to provide accurate time-of-flight (TOF) information.

4.4.5 Proportionality of Response

We have evaluated the proportionality of response of CeBr₃ scintillators. Non-proportionality (as a function of energy) in light yield can be one of the important reasons for degradation in energy resolution of established scintillators such as NaI(Tl) and CsI(Tl) [Dorenbos]. As a result, we have measured light output of CeBr₃ under excitation from isotopes such as ⁵⁷Co (122 keV γ -rays), ²²Na (511 keV and 1275 keV γ -rays) and ¹³⁷Cs (662 keV γ -rays).

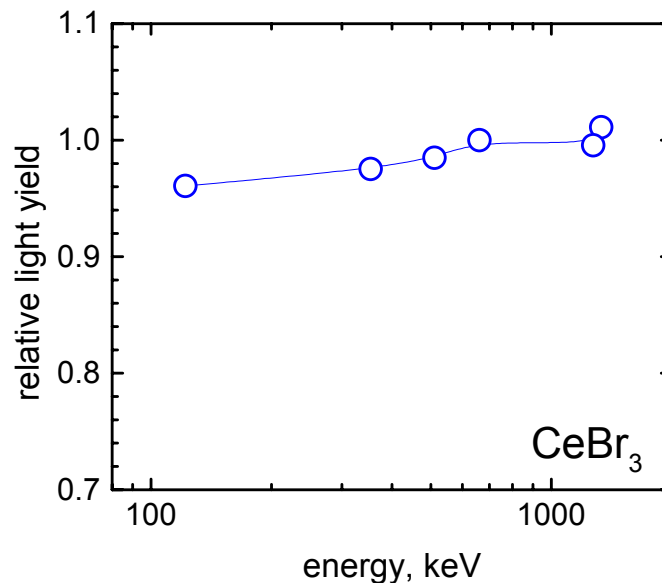


Figure 5. Proportionality of response for a CeBr₃ crystal. Over 100 keV to >1 MeV gamma ray energy range, the non-proportionality for CeBr₃ is ~5%.

A CeBr₃ crystal was wrapped in Teflon tape and coupled to a PMT. Pulse height measurements were performed using standard NIM equipment with the scintillator exposed to different isotopes. Same settings were used for PMT and pulse processing electronics for each isotope. From the measured peak position and the known γ -ray energy for each isotope, the light output (in photons/MeV) at each γ -ray energy was estimated. The data points were then normalized with respect to the light output value at 662 keV energy and the results (shown in **Figure 5**) indicate that CeBr₃ is a very proportional scintillator. Over the energy range from 100

to 1275 keV, the non-proportionality in light yield is about 4% for CeBr₃ which is substantially better than that for many established scintillators [Guillot-Noel]. The higher proportionality of CeBr₃ can be expected to enhance its energy resolution.

Overall, these measurements clearly indicate that CeBr₃ is a promising scintillator. It has high light output, fast response and shows very high energy and timing resolution. It also shows good proportionality of response over the γ -ray energy range from 100 to 1275 keV.

4.5 ENERGY RESOLUTION OF LARGER CeBr₃ CRYSTALS

Encouraged by the performance of smaller CeBr₃ crystals ($\sim 0.3 \text{ cm}^3$ size) presented in the previous section, we have grown larger CeBr₃ crystals by the Bridgman method and analyzed their performance, particularly their energy and timing resolution. In order to grow larger CeBr₃ crystals, the temperature gradients in the furnace as well as the crystal growth rate were carefully adjusted. **Figure 6** shows photographs of larger CeBr₃ crystals produced using the Bridgman method. In this section energy resolution studies for larger ($\sim 1 \text{ cm}^3$ sized) CeBr₃ crystals are discussed.

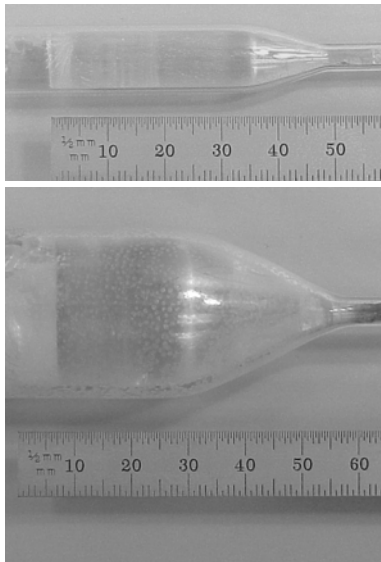


Figure 6. Photographs of Bridgman grown CeBr₃ crystals. On top, 1 cm diameter, $>1''$ length crystal, On bottom, 1" diameter, 1" long crystal.

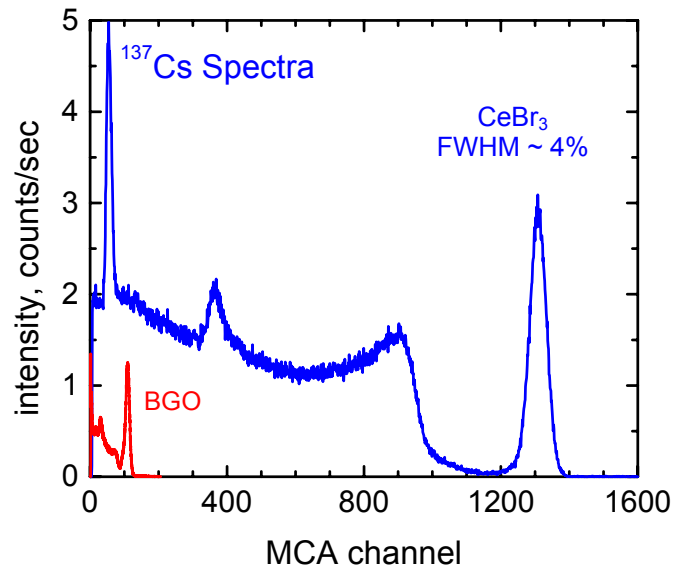


Figure 7. ^{137}Cs spectra with CeBr₃ and BGO crystals.

Energy resolution of a CeBr₃ scintillator with 1 cm^3 size for 662 keV γ -ray (^{137}Cs source) has been measured. This involved coupling an unpackaged CeBr₃ scintillator to a photomultiplier tube (with a bialkali photocathode and a quartz window). The scintillator was coated with Teflon tape to maximize the light collection and irradiated with 662 keV γ -rays (^{137}Cs source), and the resulting PMT signal was processed with a preamplifier (Canberra #2005), and then shaped with a spectroscopy amplifier (Canberra #2022). A ^{137}Cs pulse height spectrum, recorded at room temperature with shaping time of 4 μs , is shown in **Figure 7**. The energy resolution of the 662 keV photopeak was measured to be $\sim 4\%$ (FWHM) at room temperature.

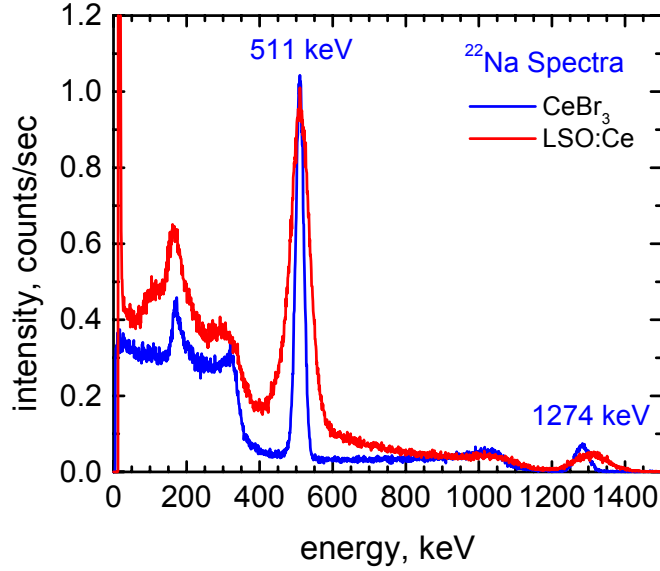


Figure 8. ^{22}Na spectra (511 keV photons) recorded with CeBr_3 and LSO crystals. The energy resolution of CeBr_3 is better by more than a factor of two compared to LSO.

Using the same approach, energy resolution of a CeBr_3 crystal (1 cm^3 size) coupled to a PMT was also measured at 511 keV energy (^{22}Na source). **Figure 8** shows the ^{22}Na spectrum for CeBr_3 -PMT detector and the energy resolution of the 511 keV photopeak was measured to be 4.5% (FWHM) at room temperature, which is substantially better than that of other PET scintillators such as BGO and LSO, which typically have energy resolution of $\geq 12\%$ (FWHM) at 511 keV. ^{22}Na spectrum for a LSO crystal coupled to a PMT is also included in **Figure 8**.

We have analyzed the measured 511 keV photopeak resolution for CeBr_3 and LSO scintillators (shown in **Figure 8**) to determine effect of various components

that contribute towards the overall broadening of the photopeak. This analysis, discussed in detail in **Chapter 3** (section 3.5.2), was performed using the framework developed by *van Eijk et. al.*, where the overall energy resolution for a scintillation detector can be expressed as [van Eijk]:

$$(\Delta E/E)^2 = R^2 = R_{phe}^2 + R_{sci}^2 + R_{noise}^2 \quad (1)$$

R_{phe} represents the resolution broadening due to the photoelectron statistics (including the excess noise effects, arising from the variance in the photodetector gain). R_{sci} represents broadening effects due to non-ideal nature of scintillators. This parameter includes contribution of effects such as inhomogeneities and nonproportionality. Finally, the electronic noise effects in the scintillation detection system are included in the final term, R_{noise} . For PMT readout, the last term, R_{noise} can be ignored due to PMT's negligible electronic noise contribution. It is possible to estimate the contribution of the first term, R_{phe} , by estimating the number of photoelectrons (N_{phe}) generated in the photodetector for a gamma-ray event in the scintillator. N_{phe} can be estimated using the following expression:

$$N_{phe} \approx N_{ph} \cdot E_\gamma \cdot \eta_{det} \quad (2)$$

where, N_{ph} is the light output of the scintillator (in photons/MeV), E_γ is energy of the incident gamma-ray in MeV (0.511 in this case) and η_{det} is the quantum efficiency of the photodetector over the emission spectrum of the scintillator (including the light collection efficiency). Once N_{phe} is known, the resolution broadening due to R_{phe} , representing variance in photoelectron statistics, can be estimated using the traditional Poisson distribution:

$$R_{phe}^2 = (2.36)^2 [ENF/N_{phe}] \quad (3)$$

where, ENF is the excess noise factor of the photodetector (~ 1.15 for PMTs). Using this framework, it is possible to estimate N_{phe} and R_{phe} from the known parameters of the

scintillator and the photodetectors using equations (2) and (3). Since $R_{noise} \approx 0$ for PMT read out, from the measured value of R and estimated value of R_{phe} , R_{sci} can be back calculated using equation (1). Using this framework, the 511 keV energy resolution of various spectrometers such as CeBr₃-PMT and LSO-PMT (see **Figure 8**) was analyzed and the results are presented in **Table I**. For LSO-PMT detector, the overall energy resolution (R) at 511 keV energy was measured to be 12% (FWHM) for LSO coupled to PMT. R_{phe} was estimated to be 5.0% (FWHM) using equation (3). R_{sci} was then calculated to be 10.9% (FWHM) from equation (1). Similar analysis was also performed for the 511 keV spectrum recorded with CeBr₃ that is shown in **Figure 8**, and the results are listed in **Table I**. The energy resolution (R) of CeBr₃ at 511 keV was measured to be 4.5% (FWHM). R_{lid} for CeBr₃-PMT detector was calculated from equation (3) to be 3.0% (FWHM). R_{sci} was then estimated to be 3.3% (FWHM). This study illustrates that the non-ideal nature of the scintillator (R_{sci}) is the dominant resolution broadening component for LSO, while in case of CeBr₃, both R_{phe} and R_{sci} have roughly similar contribution.

Table I. Analysis of the 511 keV Energy Resolution of Scintillator-PMT Spectrometers

<i>Detector</i>	<i>N_{phe} (at 0.511 MeV)</i>	<i>R (%)</i>	<i>R_{phe} (%)</i>	<i>R_{sci} (%)</i>	<i>R_{noise}(%)</i>
LSO-PMT	2600	12	5.0	10.9	0
CeBr₃-PMT	7300	4.5	3.0	3.3	0

4.6 TIMING RESOLUTION OF CeBr₃ CRYSTALS WITH ENERGY GATING

Timing resolution experiments have also been performed with a CeBr₃ crystal (1 cm diameter, 2 cm length) at the University of Pennsylvania to evaluate their potential in time-of-flight PET studies. The reference detector in this case was a thin slice (~2 mm thick, 1 cm diameter) of CeBr₃. Fast PMTs (Hamamatu's R4998) were used in both timing chains. A ²²Na source (emitting 511 keV gamma-ray pairs) was placed between the two detectors, which were operated in coincidence. Energy gating was applied on each detector to generate coincidence timing spectra and a coincidence timing distribution plot is shown in **Figure 9**. The timing resolution is estimated to be ~150 ps (FWHM). Based on prior calibration of the thin CeBr₃ sample, the coincidence timing resolution of two 20 mm-long CeBr₃ samples can be estimated to be 175 ps (FWHM). These results confirm that CeBr₃ is indeed a promising scintillator for time-of-flight PET.

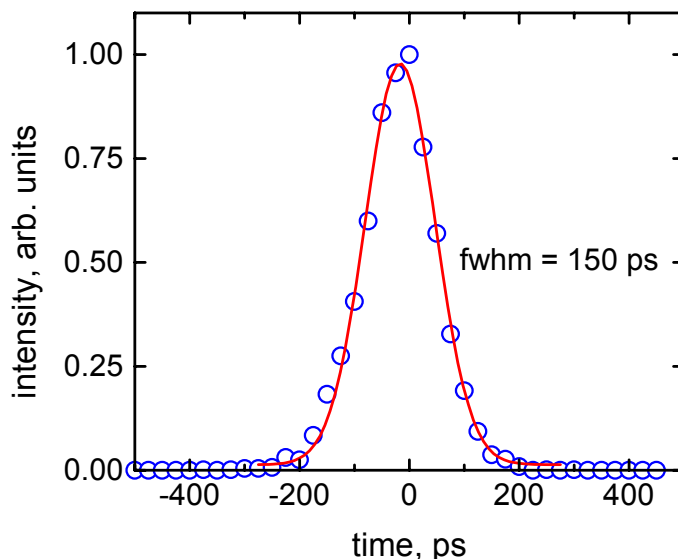


Figure 9. Timing spectrum for a CeBr₃ crystal (2 cm long, 1 cm diameter) operating in coincidence with a reference scintillator (a 2 mm thick slice of CeBr₃) at U-Penn. The coincidence timing resolution is 150 ps (FWHM).

4.7 STUDY OF OTHER CERIUM HALIDES

In addition to examination of the scintillation performance of CeBr₃, scintillation properties of other cerium halides have also been investigated. Previously, CeF₃ has been examined as a scintillator [Moses 02] and while it is fast (~30 ns decay time), its light yield is very low (~2000 photons/MeV). This limits the potential of CeF₃ in PET.

A study of CeI₃, CeCl₃ as well as a selected mixed halide (CeBr_{1.5}Cl_{1.5}) has been conducted. Small crystals (<1 cm³ size) of these materials were grown using Bridgman method and their scintillation performance was examined. CeI₃ was found to exhibit very low light yield (<5000 photons/MeV with λ_{max} of ~514 nm) and as a result was not examined further. However, the scintillation properties of CeCl₃ and CeBr_{1.5}Cl_{1.5} were promising. We have characterized emission spectra, decay time spectra, light output and energy resolution of these compositions and the results are discussed here.

4.7.1 Emission Spectra

The emission spectra for CeCl₃ and CeBr_{1.5}Cl_{1.5} have been measured under X-ray excitation using techniques discussed earlier and the normalized results are shown in **Figure 10**. The normalized emission spectrum (under X-ray excitation) of CeBr₃ is also included in the figure for comparison. As seen in the figure, the emission spectra of all three compositions are similar and fall within 300 to 500 nm range. The luminescence in each case is due to $5d \rightarrow 4f$ transition on Ce³⁺ ions. The results are summarized in **Table II**. The emission of CeCl₃ shows a primary peak at 355 nm as well as a smaller, broad peak at ~450 nm. The origin of the this ~450 nm peak is not clear though it could be due to STE luminescence or impurities in the material.

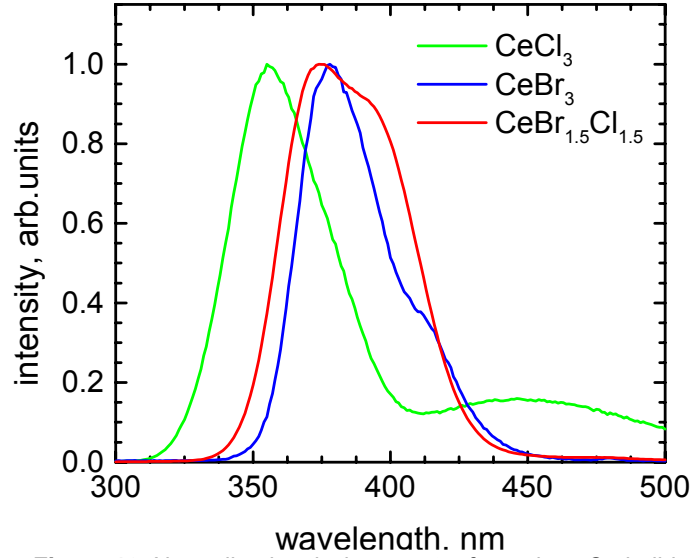


Figure 10. Normalized emission spectra for various Ce-halides.

4.7.2. Decay Time Spectra

As shown in **Figure 11**, the fluorescent decay time spectra of CeCl_3 and $\text{CeBr}_{1.5}\text{Cl}_{1.5}$ upon gamma-ray excitation (^{22}Na source, 511 keV photons) were measured using the delayed coincidence method [Bollinger]. The temporal response for each sample was fitted to an exponential decay lifetime model. The normalized results are shown in **Figure 11** (including decay time plot for CeBr_3). The principal decay time constant was estimated to be <25 ns for all compositions and the results are summarized in **Table II**. These components can be attributed to $f-d$ transitions on Ce^{3+} ions.

4.7.3. Light Output Measurements

The light output of CeCl_3 and $\text{CeBr}_{1.5}\text{Cl}_{1.5}$ test samples has been measured by acquiring ^{137}Cs spectra with these crystals and comparing the 662 keV peak position with that obtained using a calibrated BGO crystal. The optically polished samples were wrapped in Teflon tape and coupled to the face of a photomultiplier tube (with bialkali photocathode) with optical grease. The measurement was made at room temperature. The light output of the samples was estimated based on calibration of the system with BGO (see **Figure 12**). The light yield of CeCl_3 , and $\text{CeBr}_{1.5}\text{Cl}_{1.5}$ was estimated to be 45,500 and 65,000 photons/MeV, respectively. The energy resolution of the 662 keV peak was estimated to be 4% (FWHM) at room temperature for $\text{CeBr}_{1.5}\text{Cl}_{1.5}$, while it was $\sim 4.5\%$ (FWHM) for CeCl_3 . The results are summarized in **Table II**.

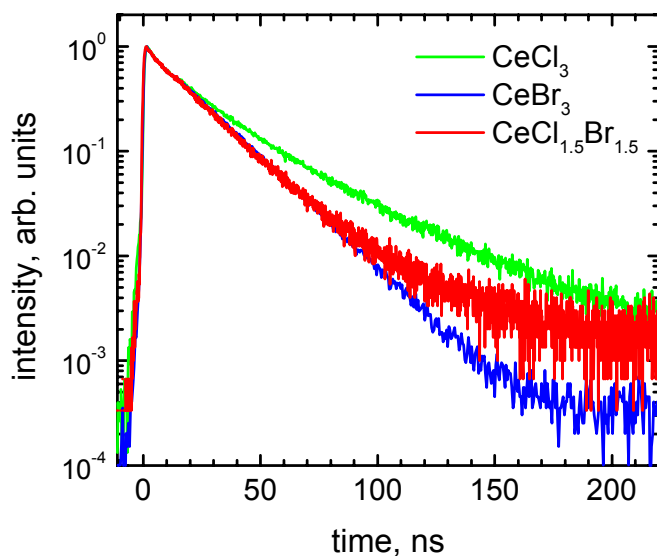


Figure 11. Normalized decay time spectra for various Ce-halides.

One observation that can be made from **Figures 10-12** is that the scintillation properties of CeBr_3 and $\text{CeCl}_{1.5}\text{Br}_{1.5}$ are very similar while that of CeCl_3 are slightly worse (particularly, its light output). The light output of CeI_3 is very low at room temperature.

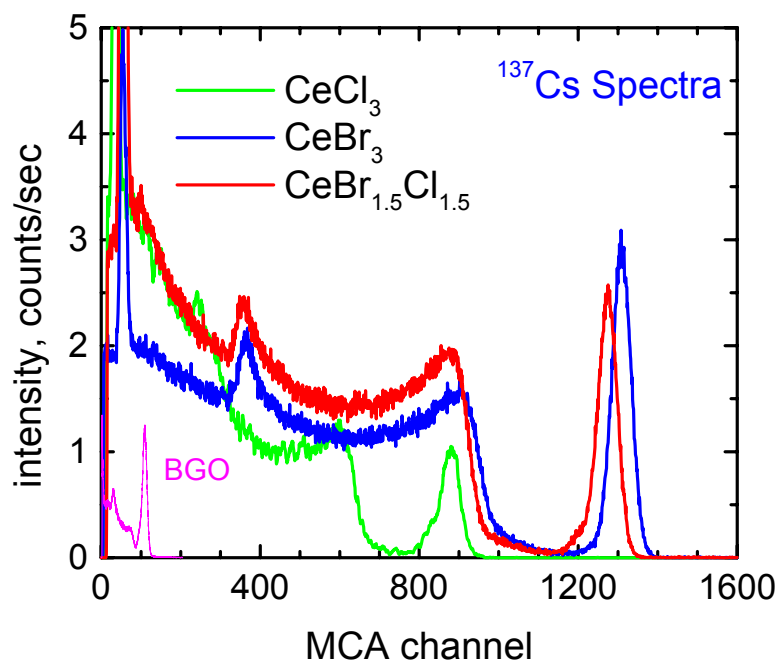


Figure 12. ^{137}Cs energy spectra for various Ce-halides and BGO.

Table II. Summary of Scintillation Properties of Various Cerium Halides

Crystal	Light Yield photons/MeV	Emission nm	Decay time ns
CeI ₃	≤5,000	514	-
CeBr _{1.5} Cl _{1.5}	65,000	370	17
CeBr ₃	68,000	370	17
CeCl ₃	45,500	355	23

4.8. SUMMARY

In our research, we have discovered a new scintillation material, CeBr₃, for γ -ray detection. Our research concentrated on growth of CeBr₃ crystals using Bridgman method, as well as characterization of the scintillation properties of these crystals. Our measurements indicate that CeBr₃ is a promising scintillator. It has high light output, fast response and shows good energy and timing resolution. Based on its performance, this new scintillation material appears to be very promising for applications such as medical imaging (positron emission tomography or PET and single photon emission computed tomography or SPECT), nuclear and particle physics research, X-ray diffraction, non destructive evaluation, nuclear treaty verification and non-proliferation monitoring, environmental cleanup, and geological exploration.

It is worth pointing out that the physical and scintillation properties of CeBr₃ are similar to those for another new promising scintillator, lanthanum bromide doped with cerium (LaBr₃:Ce) [van Loef 01, Shah 03]. The dominant luminescence in both scintillators is due to Ce³⁺. In case of LaBr₃:Ce, cerium is a dopant and it is intentionally added to enhance the scintillation performance of the material. In case of CeBr₃, cerium is an intrinsic constituent as well as an activator for the luminescence process. One issue that differentiates CeBr₃ and LaBr₃ is their self-activity due to presence of radioactive isotopes. In LaBr₃, self-activity is primarily due to ¹³⁸La that emits conversion electrons and β -particles with energy of up to 1.7 MeV. The self-activity due to ¹³⁸La in LaBr₃ has an intrinsic count-rate of ~ 1.5 events/(cm³•sec). The self-activity of CeBr₃ (due to ¹⁴²Ce that emits β -particles with total energy of 4.5 MeV) is 4×10^{-4} events/(cm³•sec). Thus, the self-activity of CeBr₃ is about 3750 times lower than that in LaBr₃. While self-activity issues are not critical in PET (which relies on coincidence measurements), the negligible self-activity of CeBr₃ makes it more attractive in large radionuclide detection and imaging systems required for homeland security applications. In these systems, large detector volumes are required and the expected extrinsic count-rate can be very low which requires detectors with very low background. Overall, both materials are very promising and deserve further investigation.

Investigation of other cerium halides such as CeI₃, CeCl₃ and CeBr_{1.5}Cl_{1.5} has also been conducted. The light output of CeI₃ is very low at room temperature, which reduces its potential as a scintillator. While the light output of CeCl₃ is lower than that for CeBr₃, the overall scintillation performance of CeBr_{1.5}Cl_{1.5} is similar to that for CeBr₃.

4.9. CURRENT STATUS

Due to unique potential of CeBr_3 , in recent years, several groups are investigating its performance. Due to its low intrinsic background, a research team at the Remote Sensing Laboratory (RSL) in Las Vegas, Nevada is evaluating CeBr_3 crystals for nuclear non-proliferation monitoring. Their research has shown that CeBr_3 crystals with larger than 100 cm³ size provide energy resolution better than 4% (FWHM) at 662 keV [Gus]. The RSL has also shown that when analyzing ^{137}Cs spectra with CeBr_3 , $\text{LaBr}_3:\text{Ce}$ and NaI:Tl , the ratio of peak height to the gross counts in the 0 to 3 MeV region is superior for CeBr_3 compared to the other two candidates [Gus]. The European Space Agency in collaboration with TUDelft is also investigating the potential of CeBr_3 in space missions, again in view of its low intrinsic background [Dorenbos 07]. Growth and evaluation of larger prototype CeBr_3 crystals is being explored at several companies and institutes including Saint Gobain Crystals [Mayhugh], Scionix [Schotanus] and Tohoku Institute of Technology, Japan [Onodera] amongst others. Finally, RMD in collaboration with Dr. Joel Karp's team is evaluating the potential of CeBr_3 crystals for time-of-flight PET [Glodo].

References:

- L. M. Bollinger and G. E. Thomas, Measurement of the time dependence of scintillation intensity by a delayed-coincidence method, *Rev Sci Instr*, vol. 32, pp. 1044, (1961).
- J.C. Brice, **Crystal Growth Processes**, Blackie Halsted Press, (1986).
- S. E. Derenzo and W. W. Moses, "Experimental efforts and results in finding new heavy scintillators," in *Heavy Scintillators for Scientific and Industrial Applications*, F. De Notaristefani, P. LeCoq, and M. Schneegans, Eds. Gif-sur-Yvette, France: Editions Frontieres, 1993, pp. 125–135.
- P. Dorenbos, *et. al.*, Non-Proportionality in the Scintillation Response and the Energy Resolution Obtainable with Scintillation Crystals, *IEEE Trans. Nuc. Sci.*, 42(6), p. 2190, (1995).
- P. Dorenbos, CeBr_3 scintillator development for space missions, Presented at 9th International Conference on Scintillators and their Applications, Winston-Salem, NC, USA, June, (2007).
- J. Glodo, E. V. D. van Loef, C. Kyba, J. S. Karp, K. S. Shah, $\text{CeBr}_3\text{-PrBr}_3$ Scintillators, Presented at IEEE NSS, Honolulu, Hawaii, Oct. (2007)
- O. Guillot-Noel *et al.*, Scintillation Properties of $\text{RbGd}_2\text{Br}_7:\text{Ce}$ Advantages and Limitations, *IEEE Trans. Nuc. Sci.*, V46(5), (1999).
- P. Gus, M. Reed, *et. al.*, CeBr_3 as a High-Resolution Gamma-Ray Detector, Presented at LDRD Symposium, Washington DC, Aug (2007).
- K. Kleinknecht, **Detectors for Particle Radiation**, 2nd Edition, Cambridge University Press, Cambridge, U.K. (1998).
- G. Knoll, Radiation Detection and Measurement, 3rd Ed., John Wiley and Sons, (1999).
- P. Lecoq and M. Korzhik, "Scintillator developments for high energy physics and medical imaging," *IEEE Trans. Nucl. Sci.*, vol. 47, pp. 1311-1314, 2000
- M. Mayhugh, Saint Gobain Crystals and Detectors, Private Communication, June, (2009).
- W.W. Moses, *Current trends in scintillator detector and materials*, *Nucl. Inst. and Meth. A*-487, pp. 123-128, (2002).

- T. Onodera, K. Hitomi, T. Shoji, Cerium Bromide Scintillation Detectors, Presented at IEEE NSS, Honolulu, Hawaii, Oct. (2007)
- P. A. Rodnyi, Physical Processes in Inorganic Scintillators, CRC Press, New York, (1997)
- P. Schotanus, Private Communication as well as Industrial booth display at SORMA XII, Ann Arbor, MI, May, (2010)
- C. W. E. van Eijk. New scintillators, new light sensors, new applications. Proceedings of The International Conference on Inorganic Scintillators and Their Applications, pp. 3–12, (Edited by Y. Zhiwen, F. Xiqi, L. Peijun, and X. Zhilin), Shanghai, China, 1997
- E.V.D. van Loef, P. Dorenbos, C.W.E. van Eijk, K. Kramer, and H.U. Gudel, High Energy Resolution Scintillator: Ce^{3+} Activated LaBr_3 , Appl. Phys. Lett., 79(10), p.1573, (2001).

CHAPTER 5: CERIUM DOPED LUTETIUM IODIDE SCINTILLATORS

5.1 OVERVIEW

This chapter covers investigation of cerium doped lutetium iodide scintillators. This chapter is adapted from the publication: *K.S. Shah et. al., LuI₃:Ce- A new scintillator for gamma-ray spectroscopy, IEEE Transactions on Nuclear Science V. 51(5), (2004)* as well as the presentation: *K.S. Shah et. al., Cerium Doped Lutetium Iodide Scintillators, Presented at IEEE NSS, Puerto Rico, October, (2005)*. This chapter covers investigation of some of the basic scintillation properties of LuI₃ crystals as well as their energy and timing resolution. Variation of scintillation properties of LuI₃:Ce crystals as a function of Ce³⁺ concentration is also included.

5.2. INTRODUCTION

Scintillation spectrometers are widely used in detection and spectroscopy of energetic photons (X-rays and γ -rays) at room temperature. These detectors are commonly used in nuclear and particle physics research, medical imaging, diffraction, non destructive testing, nuclear treaty verification and safeguards, nuclear non-proliferation monitoring, and geological exploration [Knoll, Kleinknecht].

Important requirements for the scintillation crystals used in these applications include high light output, high stopping efficiency, fast response, good proportionality, low cost and availability in large volume. These requirements cannot be met by any of the commercially available scintillators. As a result, there is continued interest in search for new scintillators with enhanced performance [Derenzo, van Eijk, Lecoq, Moses].

In this chapter, properties of a relatively new scintillator, cerium doped lutetium iodide (LuI₃:Ce), are discussed [Shah, Glodo, Birowosuta,]. The γ -ray stopping efficiency of LuI₃:Ce is higher than that of NaI(Tl), the most common scintillation detector. In our investigation, small crystals ($\sim 0.5 \text{ cm}^3$) of LuI₃:Ce have been grown using the Bridgman process and their scintillation properties have been characterized. High light output, good proportionality, fast response and excellent energy and timing resolution have been measured for small LuI₃:Ce crystals. Based on the results, LuI₃:Ce is very promising for γ -ray spectroscopy.

5.3 PHYSICAL PROPERTIES AND CRYSTAL GROWTH

LuI₃:Ce has rhombohedral crystal structure (similar to BiI₃ with R3 space group) and its density is 5.6 g/cm^3 . Based on its high atomic number constituents and high density, LuI₃:Ce provides high gamma ray stopping efficiency. The attenuation length of 511 keV photons in LuI₃:Ce is 1.7 cm. LuI₃:Ce compound melts congruently at 1050 °C and therefore its crystals can be grown using melt based methods such as Bridgman and Czochralski. This is fortunate because these melt-based processes are well suited for growth of large volume crystals [Brice]. In our research, we used Bridgman method for growing LuI₃:Ce crystals because this technique is easy to implement, and can provide good indication of the feasibility of producing high quality crystals of LuI₃:Ce from the melt. Ultra-dry forms of LuI₃ and CeI₃ were used with 99.99% purity. A two-zone Bridgman furnace was used with temperature in the hotter zone above the melting point of LuI₃ (1050 °C) and that of the cooler zone below 1050 °C. The amount of CeI₃ in the feed material was adjusted to produce LuI₃ samples with Ce³⁺ concentration in 0.5 to 20% range (on molar basis). LuI₃ crystals as large as $\sim 1 \text{ cm}^3$ were grown using Bridgman method.

Figure 1 shows a photograph of one such crystal. These crystals were then sliced from the solid ingot to produce small samples ($\leq 0.3 \text{ cm}^3$ size) for measurements.



Figure 1. Photograph of a $\text{LuI}_3\text{:Ce}$ crystal (in which its layered structure is evident) grown by Bridgman.

Scintillation properties of the LuI_3 crystals were then measured. For some measurements, packaged samples were used because $\text{LuI}_3\text{:Ce}$ crystals are sensitive to moisture. This involved placing a $\text{LuI}_3\text{:Ce}$ crystal inside a metal can on a quartz window. The crystal was attached to the quartz with a clear optical epoxy (EPO-TEK #301-2). The space around the crystal in the can was filled with SiO_2 powder. The top of the can was finally sealed by attaching a metal disc using epoxy.

5.4 SCINTILLATION PROPERTIES OF $\text{LuI}_3\text{:Ce}$

We have performed characterization of the scintillation properties of LuI_3 crystals grown by the Bridgman process. This investigation involved measurement of the light output, the emission spectrum, and the fluorescent decay time of the crystals. Energy and timing resolution of $\text{LuI}_3\text{:Ce}$ crystals and their proportionality of response were also measured. Measurements are presented here for small $\text{LuI}_3\text{:Ce}$ crystals ($< 0.5 \text{ cm}^3$) with 5% cerium followed by a summary of results for the entire Ce^{3+} concentration range (0.5 to 20%, on molar basis) studied.

5.4.1. Light Output and Energy Resolution

The light output of $\text{LuI}_3\text{:Ce}$ crystals (2-5% Ce) was measured by comparing their response to 662 keV γ -rays (^{137}Cs source) to the response of a calibrated BGO scintillator to the same isotope (see **Figure 2**). This measurement involved optical coupling of an unpackaged $\text{LuI}_3\text{:Ce}$ crystal to a photomultiplier tube (with multi-alkali S-20 photocathode), irradiating the scintillator with 662 keV photons and recording the resulting pulse height spectrum. In order to maximize light collection, the $\text{LuI}_3\text{:Ce}$ crystal was wrapped in reflective, white Teflon tape on all faces (except the one coupled to PMT). An index matching silicone fluid was also used at the PMT-scintillator interface. **Figure 2** shows pulse height spectra for both $\text{LuI}_3\text{:Ce}$ and BGO under ^{137}Cs irradiation and amplifier shaping time of 4.0 μsec . This shaping time is long enough to allow full light collection from both the scintillators. The PMT bias and amplifier gain were same for both spectra. Based on the recorded photopeak positions for $\text{LuI}_3\text{:Ce}$ and BGO, and by taking into account the photocathode quantum efficiency for BGO and LuI_3 , we estimated light output of $\text{LuI}_3\text{:Ce}$ crystal to be about 100,000 photons/MeV. This light output is the highest reported value for inorganic scintillators with principal decay time $\leq 10 \mu\text{s}$ [Knoll, Rodyni]. It

should be pointed out that this light output result for LuI₃:Ce samples is substantially higher than that reported for some of our earlier crystals [Glodo, Shah] due to considerable improvement in the crystal quality that has been achieved.

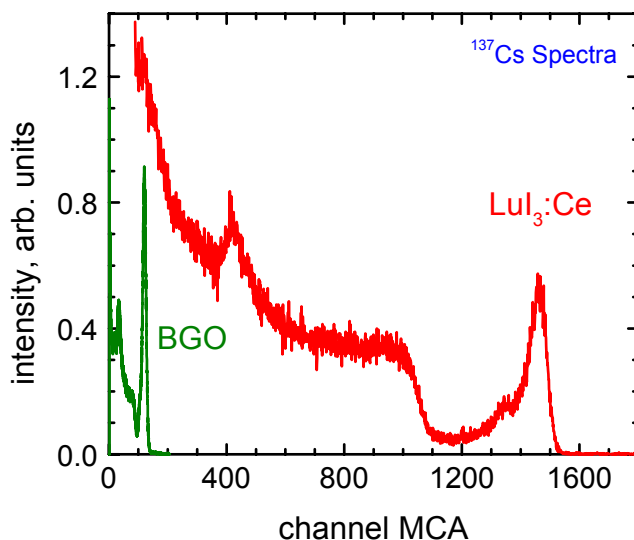


Figure 2. ¹³⁷Cs spectra recorded with LuI₃:Ce and BGO crystals. The light yield of LuI₃:Ce was estimated to be 100,000 photons/MeV and its energy resolution for the 662 keV photopeak was 3.5% (FWHM).

The energy resolution of the 662 keV photopeak recorded with LuI₃:Ce scintillator has been measured to be ~3.5% (FWHM) at room temperature as shown in **Figure 2**, which is substantially better than the energy resolution of 6-7% (FWHM) at 662 keV obtained with established scintillators such as NaI(Tl) and CsI(Tl). High energy resolution of ~4.2% (FWHM) has also been measured with LuI₃:Ce coupled to PMT for 511 keV gamma-rays (²²Na source).

5.4.2. Emission Spectrum

We have measured the emission spectrum of the LuI₃:Ce scintillators. The LuI₃:Ce (5% Ce) samples were excited with radiation from a Philips X-ray tube having a Cu target, with power settings of 30 kVp and 15 mA. The scintillation light was passed through a McPherson monochromator and detected by a Hamamatsu R2059 photomultiplier tube with a quartz window. The system was calibrated with a standard light source to enable correction for sensitivity variations as a function of wavelength. A normalized emission spectrum for a LuI₃:Ce sample is shown in **Figure 3**. The peak emission wavelength for the LuI₃:Ce sample is at ~475 nm and this emission is due to $5d \rightarrow 4f$ transition of Ce³⁺. The peak emission wavelength of 475 nm for LuI₃:Ce is reasonable for gamma ray spectroscopy because it matches well with the spectral response of the photomultiplier tubes as well as silicon photodiodes.

5.4.3. Decay Time

Decay-time spectrum of a LuI₃:Ce crystal (5% Ce) has been measured using the delayed coincidence method [Bollinger] using the Pulsed X-ray Facility available at LBNL. **Figure 4** shows the decay-time spectrum recorded for a LuI₃:Ce sample along with a multi-exponential fit to the data. The principal decay constant (τ_1) for the sample is estimated to be 25 ns and this component covers about 88% of the integrated light output of the sample. This decay component

can be attributed to optical emission arising from direct capture of electron-hole pairs at the Ce^{3+} sites. An additional decay component (τ_2) with 180 ns time constant covers the remaining 12% of the scintillation light. The risetime of the scintillation pulse from $\text{LuI}_3\text{:Ce}$ has been estimated to be ~ 0.2 ns.

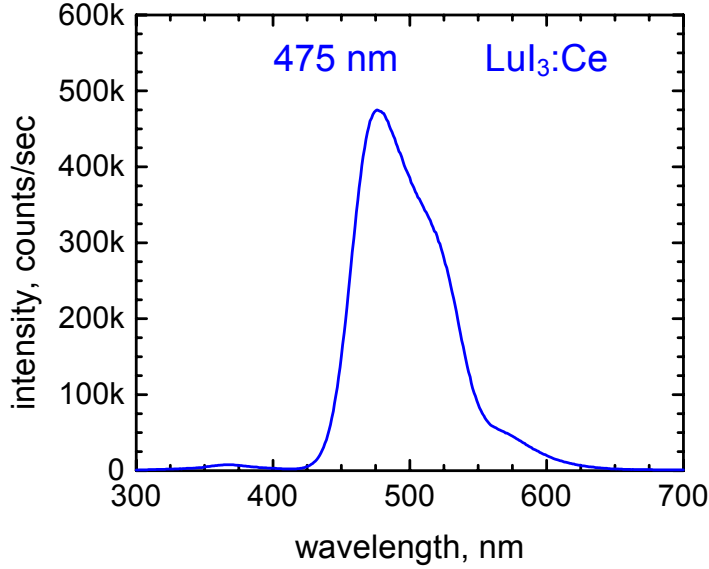


Figure 3. Optical emission spectrum for a $\text{LuI}_3\text{:Ce}$ scintillator (5% Ce) upon exposure to X-rays.

The *initial photon intensity*, a figure of merit for timing applications, has been estimated to be $\sim 3,600$ photons/(ns-MeV) for $\text{LuI}_3\text{:Ce}$, which is higher compared to all common inorganic scintillators (including BaF_2 , a benchmark for timing applications).

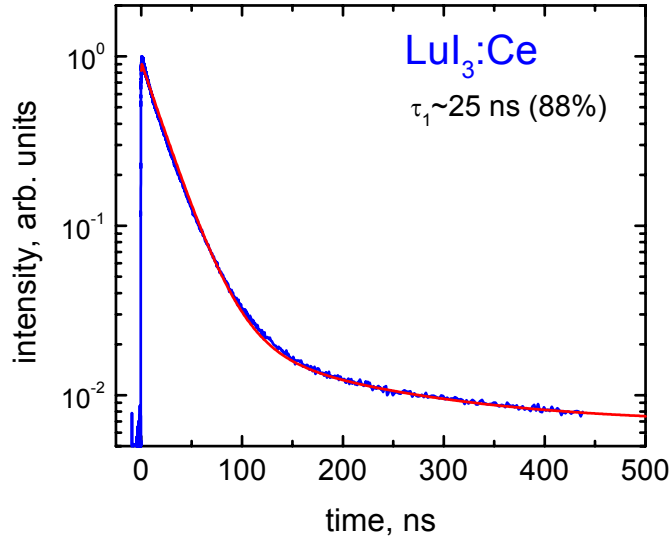


Figure 4. Decay-time spectrum for $\text{LuI}_3\text{:Ce}$ scintillator.

5.4.4. Coincidence Timing Resolution

Coincidence timing resolution of $\text{LuI}_3\text{:Ce}$ crystals has been measured. This experiment involved irradiating a BaF_2 and a $\text{LuI}_3\text{:Ce}$ scintillator (5% Ce), each coupled to a fast PMT

(Hamamatsu R5320) with 511 keV positron annihilation γ -ray pairs (emitted by a ^{22}Na source). The BaF_2 -PMT detector formed a “start” channel in the timing circuit, while the $\text{LuI}_3\text{:Ce}$ -PMT detector formed the “stop” channel. The signal from each detector was processed using two channels of a Tennelec TC-454 CFD that had been modified for use with the MCP-PMTs. The time difference between the start and stop signals was digitized with a Tennelec TC-862 TAC and a 16-bit ADC, resulting in a TDC with 7.5 ps per bin resolution. Data were accumulated until the coincidence timing distribution had approximately 10,000 counts in the maximum bin. **Figure 5** shows a coincidence timing resolution plot acquired in this manner with $\text{LuI}_3\text{:Ce}$ and BaF_2 crystals and the timing resolution was measured to be <200 ps (FWHM). Using the same setup, the timing resolution of two BaF_2 crystals in coincidence was measured to be 210 ps (FWHM). These results confirm that $\text{LuI}_3\text{:Ce}$ is well suited for applications requiring fast response, high count-rates, and good timing resolution. Based on its high timing resolution, $\text{LuI}_3\text{:Ce}$ scintillator can be expected to provide accurate time-of-flight (TOF) information.

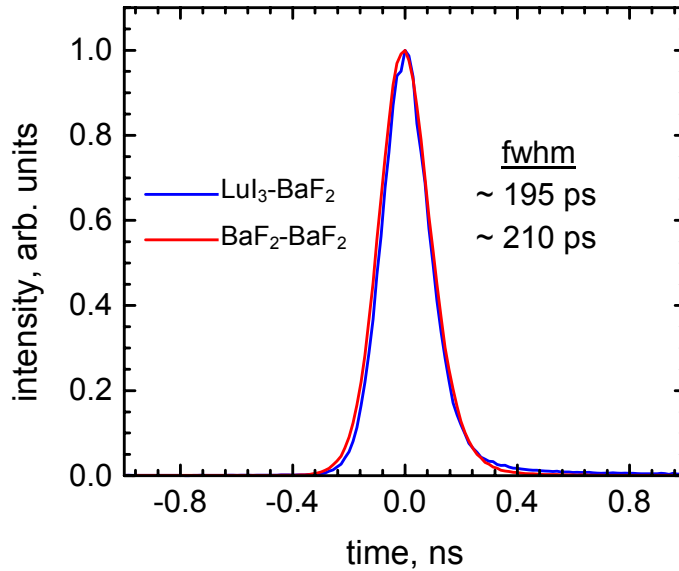


Figure 5. Coincidence timing resolution plot for BaF_2 and $\text{LuI}_3\text{:Ce}$ scintillators upon irradiation with 511 keV gamma ray pairs. The timing resolution is 195 ps (FWHM). For BaF_2 - BaF_2 pair, the timing resolution is 210 ps (FWHM).

5.4.5. Proportionality of Response

We have evaluated the proportionality of response of $\text{LuI}_3\text{:Ce}$ scintillators. Non-proportionality (as a function of energy) in light yield can be one of the important reasons for degradation in energy resolution of established scintillators such as NaI(Tl) and CsI(Tl) [Dorenbos 95, Moses]. As a result, we have measured light output of $\text{LuI}_3\text{:Ce}$ under excitation from isotopes such as ^{57}Co (14 and 122 keV γ -rays), ^{22}Na (511 keV and 1275 keV γ -rays) and ^{137}Cs (662 keV γ -rays). A $\text{LuI}_3\text{:Ce}$ crystal was wrapped in Teflon tape and coupled to a PMT. Pulse height measurements were performed using standard NIM equipment with the scintillator exposed to different isotopes. Same settings were used for PMT and pulse processing electronics for each isotope. From the measured peak position and the known γ -ray energy for each isotope, the light output (in photons/MeV) at each γ -ray energy was estimated. The data points were then

normalized with respect to the light output value at 662 keV energy and the results (shown in **Figure 6**) indicate that $\text{LuI}_3\text{:Ce}$ is a very proportional scintillator. Over the energy range from 14 to 1275 keV, the non-proportionality in light yield is about 5% for $\text{LuI}_3\text{:Ce}$ which is substantially better than that for many established scintillators [Guillot-Noel]. The higher proportionality of $\text{LuI}_3\text{:Ce}$ can be expected to enhance its energy resolution.

Overall, these measurements clearly indicate that $\text{LuI}_3\text{:Ce}$ is a promising scintillator. It has high light output, fast response and shows very high energy and timing resolution. It also shows good proportionality of response over the γ -ray energy range from 14 to 1275 keV.

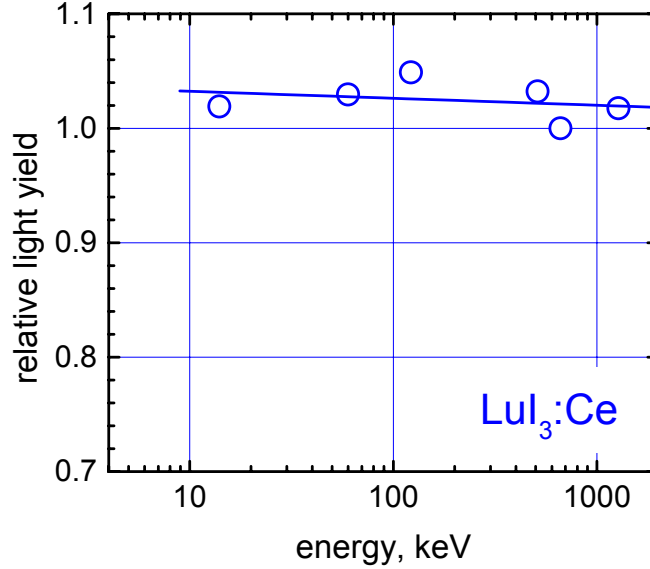


Figure 6 Proportionality in light yield as a function of γ -ray energy for $\text{LuI}_3\text{:Ce}$ at room temperature.

5.4.6. Effect of Ce^{3+} Concentration on Scintillation Properties of $\text{LuI}_3\text{:Ce}$

In addition to LuI_3 crystals with 5% Ce, additional LuI_3 crystals with Ce^{3+} concentration of 0.5%, 2%, 10% and 20% (on molar basis) were also grown by Bridgman method. Small crystals ($\sim 0.3 \text{ cm}^3$) were cut from the Bridgman grown ingots. Light output, emission spectra, and decay time spectra were measured for these crystals ($\leq 1 \text{ cm}^3$ size) using techniques described in sections 5.4.1 to 5.4.3 in order to determine the relationship between scintillation properties of LuI_3 and the Ce^{3+} doping level. The results of this investigation are presented in **Table I** and indicate that as the cerium concentration is increased from 0.5% to 5%, the timing properties (rise as well as decay times) become faster. This improvement is observed without any significant degradation in light output. However as the Ce^{3+} concentration is increased beyond 5%, the light yield begins to drop, very fast decay component(s) appear, and a shift in emission towards longer wavelength is observed. These trends indicate that self absorption and quenching processes govern scintillation properties of LuI_3 at Ce^{3+} doping levels above 5%. Based on the results presented in **Table I**, Ce^{3+} doping level in 2-5% range appears to be optimal for LuI_3 because the light yield is very high in this doping range and the temporal response is also reasonably fast.

Table I. Scintillation Properties of LuI_3 as a function of Ce^{3+} Doping Level

Ce %	Light Yield photons/MeV	Emission nm	Risetime ns	Decay time(s) ns
0.5	$\geq 100,000$	475	~ 5	40 (89%), 300 (11%)
2	$\geq 100,000$	475	0.4	30 (93%), 180 (7%)
5	$\geq 100,000$	475	0.2	25 (88%), 180 (12%)
10	70,000	475	0.1	5 (9%), 28 (68%), 180 (23%)
20	38,000	525	0.1	5 (9%), 30 (60%), 180 (31%)

5.5. SUMMARY AND CURRENT STATUS

In our research, we have investigated a new scintillation material, $\text{LuI}_3:\text{Ce}$, for γ -ray detection. Our research involved growth of $\text{LuI}_3:\text{Ce}$ crystals using Bridgman method, as well as characterization of the scintillation properties of these crystals. Our measurements indicate that $\text{LuI}_3:\text{Ce}$ is a promising scintillator. It has high light output, fast response and shows good energy and timing resolution. Based on its performance, this new scintillation material appears to be very promising for medical imaging, particularly positron emission tomography (PET). Nuclear and particle physics research, X-ray diffraction, non-destructive evaluation, nuclear treaty verification, environmental cleanup, and geological exploration also appear to be potential applications for this new scintillator. Preparation of large crystals of $\text{LuI}_3:\text{Ce}$ and evaluation of their properties is necessary in order to investigate the full potential of this promising scintillator. Due to its layered, rhombodredal crystal structure, growth of large crystals of this composition appears to be challenging.

While the efforts to grow high quality bulk single crystals continue, alternative approaches, such as growth of thin, single-crystal layers using sintering and melt quenching approaches are also being explored at RMD [Glodo]. These $\text{LuI}_3:\text{Ce}$ crystal layers (approximately 2 mm thick) provide emission and decay characteristics very similar to those for the bulk single crystals discussed earlier in this chapter and their light output is already about 75% of the best value for bulk crystals with room for considerable improvement as the optical quality of these layers is enhanced [Glodo]. These thin $\text{LuI}_3:\text{Ce}$ crystalline layers are expected to be much easier to produce than the large bulk crystals and they can be employed in a PET module design with stacked detector (see **Figure 7**) such as the one being developed at the Stanford University with silicon APDs [Levin]. In this

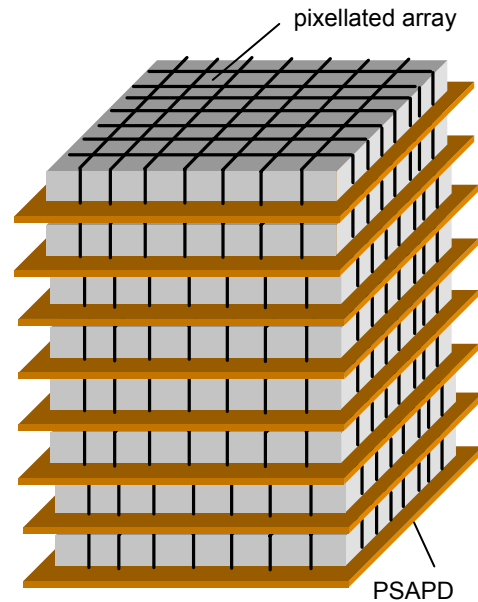


Figure 7. Design of a PET module being explored at the Stanford University consisting of a stack of thin, pixellated crystal arrays coupled to PSAPDs [Levin]. While the original design is based on $\text{LSO}:\text{Ce}$ crystal layers, $\text{LuI}_3:\text{Ce}$ crystal layers can also be considered in this configuration.

PET module design each detector consists of a number of sub-detectors. Each sub-detector is based on a thin (approximately 2 mm thick), pixellated crystal layer of a scintillator coupled to RMD's position sensitive avalanche photodiode. This concept maximizes the collection of the scintillation light at the photodetector surface and inherently provides DOI information [Levin]. While Dr. Levin's current research is based on LSO:Ce crystals layers (1-2 mm thick scintillators in 8x8 format with 1 mm pixel size), improved scintillators such as LuI₃:Ce with significantly higher light output, faster decay and better spectral match with silicon sensors (than LSO:Ce) would enhance the overall detector performance. This arrangement would allow exploitation of excellent scintillation properties of LuI₃:Ce without the need to grow large bulk crystals and on-going research at RMD is exploring this avenue.

5.6 REFERENCES:

- L. M. Bollinger and G. E. Thomas, Measurement of the time dependence of scintillation intensity by a delayed-coincidence method, *Rev Sci Instr*, vol. 32, pp. 1044, (1961).
- J.C. Brice, **Crystal Growth Processes**, Blackie Halsted Press, (1986).
- S. E. Derenzo and W. W. Moses, "Experimental efforts and results in finding new heavy scintillators," in *Heavy Scintillators for Scientific and Industrial Applications*, F. De Notaristefani, P. LeCoq, and M. Schneegans, Eds. Gif-sur-Yvette, France: Editions Frontieres, 1993, pp. 125–135.
- P. Dorenbos, *et. al.*, Non-Proportionality in the Scintillation Response and the Energy Resolution Obtainable with Scintillation Crystals, *IEEE Trans. Nuc. Sci.*, 42(6), p. 2190, (1995).
- J.Glodo, : *A Novel, High Resolution PET Detector. DOE SBIR Phase I project, DOE Contract Number DE-FG02-08ER85175, Final Report, April, 2008*
- O. Guillot-Noel et al., Scintillation Properties of RbGd₂Br₇:Ce Advantages and Limitations, *IEEE Trans. Nuc. Sci.*, V46(5), (1999).
- K. Kleinknecht, **Detectors for Particle Radiation**, 2nd Edition, Cambridge University Press, Cambridge, U.K. (1998).
- G. Knoll, *Radiation Detection and Measurement*, 3rd Ed., John Wiley and Sons, (1999).
- P. Lecoq and M. Korzhik, "Scintillator developments for high energy physics and medical imaging," *IEEE Trans. Nucl. Sci.*, vol. 47, pp. 1311-1314, 2000
- C. S. Levin, F. Habte, A. M. Foudray, *NIM A* **527**, 2004, pp. 35-40, "Methods to extract more light from minute scintillation crystals used in an ultra-high resolution positron emission tomography detector";
- W.W. Moses, *Current trends in scintillator detector and materials*, *Nucl. Inst. and Meth. A*-487, pp. 123-128, (2002).
- P. A. Rodnyi, *Physical Processes in Inorganic Scintillators*, CRC Press, New York, (1997)
- C. W. E. van Eijk. New scintillators, new light sensors, new applications. Proceedings of The International Conference on Inorganic Scintillators and Their Applications, pp. 3–12, (Edited by Y. Zhiwen, F. Xiqi, L. Peijun, and X. Zhilin), Shanghai, China, 1997
- E.V.D. van Loef, P. Dorenbos, C.W.E. van Eijk, K. Kramer, and H.U. Gudel, High Energy Resolution Scintillator: Ce³⁺ Activated LaBr₃, *Appl. Phys. Lett.*, 79(10), p.1573, (2001).

Chapter 6: Elpasolite and Alkaline Earth Halide Scintillators for SPECT

6.1 INTRODUCTION

Single photon emission computed tomography (SPECT) is a powerful, noninvasive medical imaging modality that mathematically reconstructs the three dimensional distribution of a radionuclide throughout the body of a human patient or a research animal [Cherry]. Typically, the collected data are displayed and evaluated as a set of two-dimensional images through the organ or diseased area under investigation. SPECT allows quantitative study of the function in the investigated region and therefore is an extremely useful tool for understanding organ and tissue physiology including that in the heart, lung, kidney, liver, brain, and skeletal system. SPECT agents now are becoming available for prostate and other forms of cancer as well. SPECT is very commonly used in identifying and localizing coronary artery disease and as many as 90% of all myocardial perfusion studies are now performed using SPECT.

At present, the performance of SPECT systems often is limited by the detectors used in these systems. Modern SPECT systems consist of scintillation crystals coupled to photomultiplier tubes as detectors. Important requirements for scintillators used in SPECT applications include high light output and high energy resolution, reasonably fast response and high gamma ray stopping efficiency. Ideally, the scintillator should also be inexpensive, rugged and easy to manufacture. Currently, NaI:Tl is the detector of choice in SPECT systems and it is relatively inexpensive and its light output is fairly large. However, the poor energy resolution of NaI:Tl often limits SPECT performance [Heanue]. The energy resolution of NaI:Tl is limited by its relatively poor proportionality [Dorenbos, Moses]. If scintillators with higher energy resolution at typical SPECT energies (~ 140 keV) were available, the essential process of scatter rejection would improve. Furthermore, dual-isotope imaging, which is a unique property of SPECT, would also become possible if scintillators with high energy resolution became available.

Over last decade, cerium doped lanthanum bromide ($\text{LaBr}_3\text{:Ce}$) has emerged as a promising scintillator for gamma-ray spectroscopy [van Loef 01, Shah 03]. $\text{LaBr}_3\text{:Ce}$ and other related rare earth trihalides (such as CeBr_3) provide high light output ($>60,000$ photons/MeV) along with very fast response (≤ 20 ns) and good proportionality, particularly at high energies. Correspondingly, the energy resolution of these materials is very high at 511 keV ($\sim 3.5\%$ FWHM), which is almost a factor of two higher than that from NaI:Tl. However, $\text{LaBr}_3\text{:Ce}$ (and related scintillators) show increased non-proportionality at lower electron energies [Choong, Cherepy], which is expected to impact the energy resolution of $\text{LaBr}_3\text{:Ce}$ over the energy range of interest for SPECT. The current cost of large $\text{LaBr}_3\text{:Ce}$ crystals is also high, primarily due to difficulties (such as cracking and cleavage) associated with growth of large $\text{LaBr}_3\text{:Ce}$ crystals which have anisotropic, hexagonal crystal structure. As a result, the search for improved scintillators for SPECT continues.

In this chapter, properties of promising scintillator compositions belonging to Ce^{3+} doped elpasolite and Eu^{2+} doped alkaline earth halide families are discussed [Shah 07 & 09, Wilson, van Loef 08, Cherepy]. A screening of over ten elpasolite compositions was carried out and a promising composition, $\text{Cs}_2\text{LiLaBr}_6\text{:Ce}$ (or CLLB) was chosen for further evaluation. In the alkaline earth family, $\text{SrI}_2\text{:Eu}$ was chosen for further evaluation as a scintillator for SPECT.

These scintillators offer relatively high stopping power, high light yield, and good proportionality. They are spectrally well matched to PMTs as well as the advanced silicon photodetectors. Energy resolution of these new scintillators at 662 keV (^{137}Cs source) is <3% (FWHM), which is very similar to that for $\text{LaBr}_3\text{:Ce}$ and two times better than that for NaI:Tl . Furthermore, these scintillators offer very high proportionality over a broad energy range. As a result, they provide excellent energy resolution at lower gamma-ray energies too. For example, at 122 keV (^{57}Co source), the energy resolution of $\text{SrI}_2\text{:Eu}$ and CLLB:Ce is <6% (FWHM), while that of NaI:Tl is in 9-10% (FWHM) range. Since the gamma-rays emitted by $^{99\text{m}}\text{Tc}$ (the most common radioisotope for SPECT) have energy of 140 keV, similar to 122 keV gamma-ray emission from ^{57}Co , the high energy resolution of CLLB and $\text{SrI}_2\text{:Eu}$ at 122 keV, confirms their promise for SPECT.

6.2. DETECTOR REQUIREMENTS FOR SINGLE PHOTON IMAGING

The detector requirements for SPECT are straightforward and result from the considerations of patient safety and image quality. Patient safety requires that the detectors be sufficiently sensitive to optimize the use of the emitted radiation in order to minimize the patient dose while offering image quality sufficient for the diagnostic task. The specifications are derived from the characteristic of the isotopes used. Since SPECT is commonly performed (~70% of the time) using $^{99\text{m}}\text{Tc}$ (140 keV), good detection efficiency and high energy resolution at 140 keV are needed, although radioisotopes with lower as well as higher energy emissions are also available. Essentially, the detection efficiency must exceed 80% for the gamma ray energy of interest. Regarding energy resolution, the detector must be able to distinguish photoelectric events from Compton events. Typically, ~9% (FWHM) resolution is obtained with NaI(Tl) crystals coupled to photomultipliers at 140 keV, however, better energy resolution would offer superior scatter rejection. Recent studies have shown that energy resolution ~4% (FWHM) would provide adequate scatter rejection for myocardial perfusion studies [Heanue]. Count-rate requirements for SPECT are moderate and should be readily achievable with the new elpasolite scintillators which have significantly faster decay times than NaI:Tl .

High energy resolution of SPECT detectors can also have important implications for dual-isotope imaging such as $^{201}\text{Tl}/^{99\text{m}}\text{Tc}$ -sestamibi imaging of myocardial perfusion [Liu, Johnson 87, Johnson 90, Berman, Maddahi, Alexander]. Such dual isotope studies are performed sequentially by acquiring a ^{201}Tl myocardial perfusion scan at rest, followed by a myocardial perfusion scan acquired under stress with $^{99\text{m}}\text{Tc}$ -sestamibi [Heo, Kiat]. This provides an alternative to traditional myocardial imaging in which ^{201}Tl is injected to acquire a stress image, followed by a 2-3 hr redistribution period after which a ^{201}Tl rest image is acquired. Although the ^{201}Tl rest/stress study can be acquired with a single injection, the sequential $^{201}\text{Tl}/^{99\text{m}}\text{Tc}$ study shortens the procedure time and takes advantage of the improved photon statistics and photon energy characteristics from $^{99\text{m}}\text{Tc}$ -sestamibi for the stress scan. The improved energy resolution expected from newer scintillators has the potential of reducing errors due to contamination of the ^{201}Tl data from lead x-ray and Compton scatter in dual-isotope $^{201}\text{Tl}/^{99\text{m}}\text{Tc}$ imaging.

6.3. SCINTILLATORS FOR SINGLE PHOTON IMAGING

Scintillation crystals coupled to PMTs are commonly used as γ -ray detectors in single photon imaging. **Table 1** provides a comparison of common inorganic scintillators considered in

SPECT. Most commercial SPECT systems at present use NaI:Tl scintillators. NaI:Tl crystals are available in large sizes at reasonable cost and offer relatively high light output. The main limitation of NaI:Tl in SPECT imaging is its modest energy resolution (~9% FWHM at 140 keV). CsI:Tl is a bright scintillator which also is available and cost-effective in large sizes. The spectral emission of CsI:Tl has a better match with silicon photodiodes than with PMTs and dedicated, single photon imaging systems for cardiac studies have been built using CsI:Tl scintillators with solid-state photodetectors [www.digirad.com]. However, CsI:Tl scintillators also show relatively poor energy resolution at the photon energies used for SPECT (~10% FWHM at 140 keV). For both NaI:Tl and CsI:Tl, the energy resolution is limited by their nonproportional response [Dorenbos, Moses]. Scintillators such as YAP (YAlO₃:Ce) have been used in combined SPECT-PET small animal systems [www.ise-srl.com/YAPPET/yap-doc.htm]. YAP:Ce shows high degree of proportionality but its light output is low, which limits its energy resolution.

Newer, rare earth trihalide scintillators such as LaBr₃:Ce show very high light output and fast response (see **Table 1**). LaBr₃:Ce scintillators also show high proportionality, though increased nonproportionality is observed at low electron energies [Cherepy]. As a result, even though the energy resolution of LaBr₃:Ce is almost 2-fold better than that of NaI:Tl at 662 keV, the improvement at typical SPECT energy (of 140 keV) is rather modest (about 25%). Also, large crystals of LaBr₃:Ce are still expensive due to difficulties associated with growth of high quality, large crystals of LaBr₃ that are prone to cracking and cleavage. These problems arise mostly due to highly anisotropic, hexagonal structure of LaBr₃. LaCl₃:Ce and CeBr₃, which are related rare earth halide scintillators with the same hexagonal crystal structure as LaBr₃:Ce, also face many of the same challenges that are present for LaBr₃:Ce.

Table 1. Properties of Inorganic Scintillators for Nuclear Medicine

Material	Light Output [Photons/MeV]	Wavelength of Maximum Emission [nm]	Attenuation Length (140 keV) [cm]	Principal Decay Time [ns]
NaI(Tl)	38,000	415	0.4	230
CsI(Tl)	52,000	540	0.26	1000
YAP	20,000	370	0.65	26
LaBr ₃ :Ce	≥63,000*	360	0.35	17

* Saint Gobain quotes light yield of 63K photons/MeV for its LaBr₃:Ce, RMD has measured light output of 70K photons/MeV for its LaBr₃:Ce

In view of these limitations for existing scintillators for SPECT, new promising classes of scintillators (Ce³⁺ doped elpasolites and Eu²⁺ doped alkaline earth halides) are discussed in this chapter for SPECT.

6.4 Ce³⁺ DOPED ELPASOLITE SCINTILLATORS

6.4.1 Overview

A new class of halide scintillators crystallizing in the ordered double perovskite (or elpasolite) structure has recently been discovered [Shah 07 & 09, van Loef 05, Glodo 06, Bessiere, Birowosuto]. Elpasolites with composition A₂BMX₆ (with A = Rb, Cs, K; B = Li, Na, K; M = La, Ce, Gd, Y, Al; X = F, Cl, Br, I) are model systems investigated in numerous optical, scintillation and magnetic studies [Cross, Meyer, van Eijk 05]. Elpasolites are named after the

mineral K_2NaAlF_6 found at the site of El Paso county, Colorado, in 1883. One advantage the elpasolites have over many other crystalline systems is that the M^{3+} site, located at the center of an octahedron of halide ions X^- , offers a natural environment for incorporating Ce^{3+} or other trivalent ions. Many of these materials retain cubic or near cubic structures over a range of compositions. Recent investigation of Ce^{3+} doped elpasolites as scintillators was initially carried out using compositions with Li ions on the *B-site* [van Loef 05, Bessiere, van Eijk 05]. These Li-containing scintillators were targeted towards thermal neutron detection. Based on promising results generated by research at TUDelft [Bessiere], the initial attention on elpasolites at RMD was focused on $\text{Cs}_2\text{LiYCl}_6\text{:Ce}$ (or CLYC) for thermal neutron detection [Shah 07, Glodo 06]. During our investigation of CLYC, one interesting observation made was its extremely high proportionality (<1% non-proportionality over 60 to 1275 keV gamma-ray energy range). Due to such high proportionality, CLYC provided very high energy resolution ($\leq 4\%$ FWHM at 662 keV), despite its relatively low light output of $\sim 20,000$ photons/MeV for gamma-rays.

The combination of very high proportionality, high energy resolution and cubic crystal structure (which makes growth of large crystals easier compared to complex hexagonal structure of $\text{LaBr}_3\text{:Ce}$) of CLYC prompted us to investigate elpasolite compositions that share these promising features of CLYC but are brighter. In our investigation, small crystals ($\leq 1 \text{ cm}^3$) of several Ce doped elpasolites were grown by Bridgman method and their scintillation characteristics (emission wavelength, decay time, light output and non-proportionality) were measured. **Table 2** provides a summary of these measurements for various elpasolites [Shah 07].

Table 2. Properties of Ce^{3+} doped Elpasolites

Material	Wavelength of Maximum Emission [nm]	Light Output [Photons/MeV]	Decay Time [ns] for Ce^{3+} Luminescence	Non-Proportionality Over 60 to 1275 keV Range (%)
$\text{Cs}_2\text{NaLaI}_6\text{:Ce}$	455	54,000 – 60,000	50	<2%
$\text{Cs}_2\text{LiLaI}_6\text{:Ce}$	450	$\geq 55,000$	50	<2%
$\text{Cs}_2\text{LiLaBr}_6\text{:Ce}$	420	55,000 - 60,000	55	<2%
$\text{Cs}_2\text{NaLaBr}_6\text{:Ce}$	400	12,000	55	3%
$\text{Cs}_2\text{LiLaCl}_6\text{:Ce}$	390	36,000	90	<2%
$\text{Cs}_2\text{NaCeBr}_6$	415	32,000	115	12.5%
$\text{Cs}_2\text{LiCeBr}_6$	420	35,000	100	12.5%
$\text{Cs}_2\text{NaGdI}_6\text{:Ce}$	445	21,000	55	<2%
$\text{Cs}_2\text{NaLuI}_6\text{:Ce}$	450	27,000	35	2.5%
$\text{Cs}_2\text{LiLuI}_6\text{:Ce}$	490	12,000	45	<3%
$\text{Cs}_2\text{LiYCl}_6\text{:Ce}$	370	20,000	37	<1%

These measurements, while dependent on the quality of the crystals produced, provide some interesting observations. It can be seen that several elpasolites with La ions occupying the *M-site* provide higher light output than other candidates, with the light output of at least three candidates ($\text{Cs}_2\text{LiLaI}_6\text{:Ce}$ or CLLI, $\text{Cs}_2\text{NaLaI}_6\text{:Ce}$ or CNLI and $\text{Cs}_2\text{LiLaBr}_6\text{:Ce}$ or CLLB) approaching that for $\text{LaBr}_3\text{:Ce}$. Another interesting trend observed is that all elpasolites that we evaluated showed excellent non-proportionality with exception of self-activated elpasolites where Ce ions occupy the *M-site*. It should be noted that in addition to the fast decay constant for Ce^{3+} based luminescence presented in **Table 2**, slower decay components were present

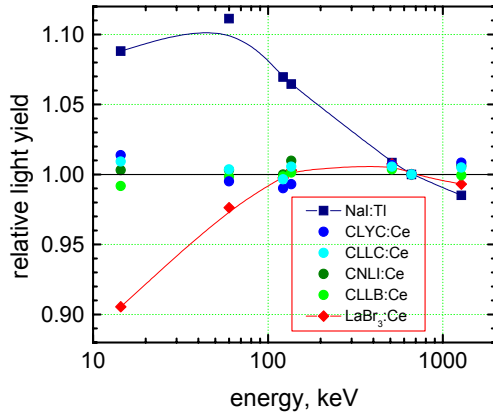


Figure 2. Proportionality between 14 and 1274 keV measured for NaI:Tl, CLYC:Ce, CLLC:Ce, CNLI:Ce, CLLB:Ce, and $\text{LaBr}_3\text{:Ce}$ crystals using isotopic sources with different γ -energies.

selected elpasolites as well as $\text{LaBr}_3\text{:Ce}$ and NaI:Tl crystals available at RMD are shown in **Figure 2**. As seen in the figure, the proportionality of all elpasolites is very high and is significantly better than that of not only NaI:Tl but also $\text{LaBr}_3\text{:Ce}$ (particularly at low energies). **Figure 3** shows 662 keV energy spectra (^{137}Cs source) for several elpasolites as well as NaI:Tl and $\text{LaBr}_3\text{:Ce}$. The energy resolution of all of the selected elpasolites is superior to that for NaI:Tl and some of them

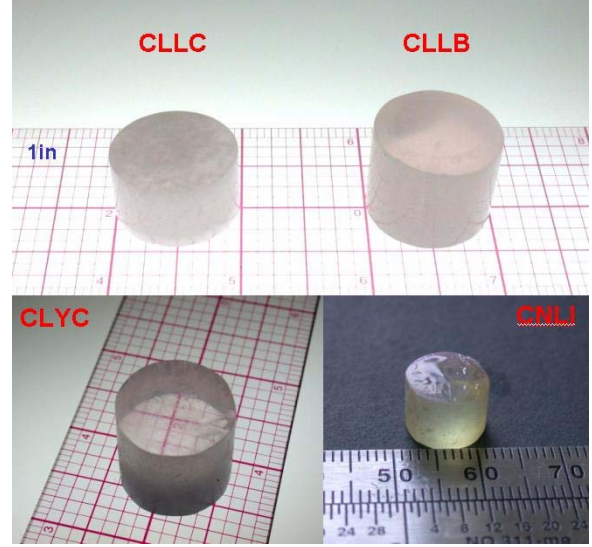


Figure 1. Photographs of elpasolite crystals grown at RMD using the Bridgman method.

in almost all cases. Based on the initial measurements, CLLI, CNLI, CLLB and CLLC appeared to be promising candidates and were selected for further evaluation.

For several elpasolites (such as CLYC, CLLC, CNLI and CLLB) where high quality, small crystals were available (see **Figure 1**), we conducted non-proportionality studies over a wider energy range (14 keV to 1275 keV energy range) using isotopic sources such as ^{57}Co , ^{241}Am , ^{22}Na and ^{137}Cs . These measurements were conducted on samples that were ≤ 1 cm³ in size. The resulting proportionality plots for

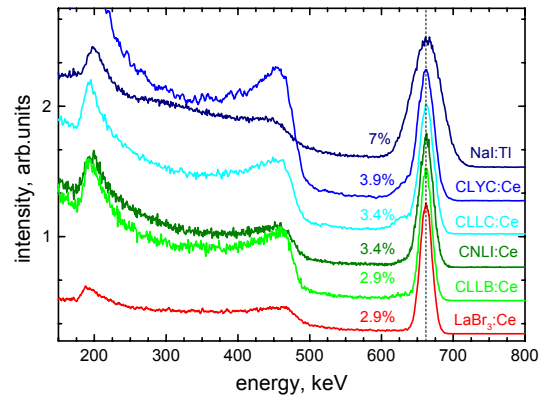


Figure 3. ^{137}Cs energy spectra collected with NaI:Tl, CLYC:Ce, CLLC:Ce, CNLI:Ce, CLLB:Ce, and $\text{LaBr}_3\text{:Ce}$ crystals at RMD.

even approach $\text{LaBr}_3\text{:Ce}$'s energy resolution. These results confirm the promise of this class of scintillators. Out of the brightest elpasolite compositions we have identified (CNLI, CLLI and CLLB), only CLLB is cubic [Yang], the others such as CLLI and CNLI are trigonal (or pseudo-cubic). As a result, we have selected CLLB for detailed evaluation, which is discussed in the following section.

6.4.2 $\text{Cs}_2\text{LiLaBr}_6\text{:Ce}$ (CLLB) Scintillators

6.4.2.1. OVERVIEW

$\text{Cs}_2\text{LiLaBr}_6\text{:Ce}$ has a cubic elpasolite structure that is isotropic (see **Figure 4**). As a result, growth of large volume crystals of these compositions can be expected to be substantially easier compared to that of hexagonal LaBr_3 , CeBr_3 and LaCl_3 compositions. The melting point of CLLB, based on measurements performed at RMD, is approximately 500 °C and its estimated density is 4.2 g/cm³. Small crystals (~1 cm³ size) of CLLB (undoped and with varying Ce^{3+} doping level) have been grown at RMD using the Bridgman method. Scintillation characteristics of these crystals have been evaluated, which includes measurement of emission spectrum, decay time spectrum and light output. Gamma-ray detection characteristics including energy resolution, proportionality and timing resolution for Ce^{3+} doped CLLB crystals has also been performed.

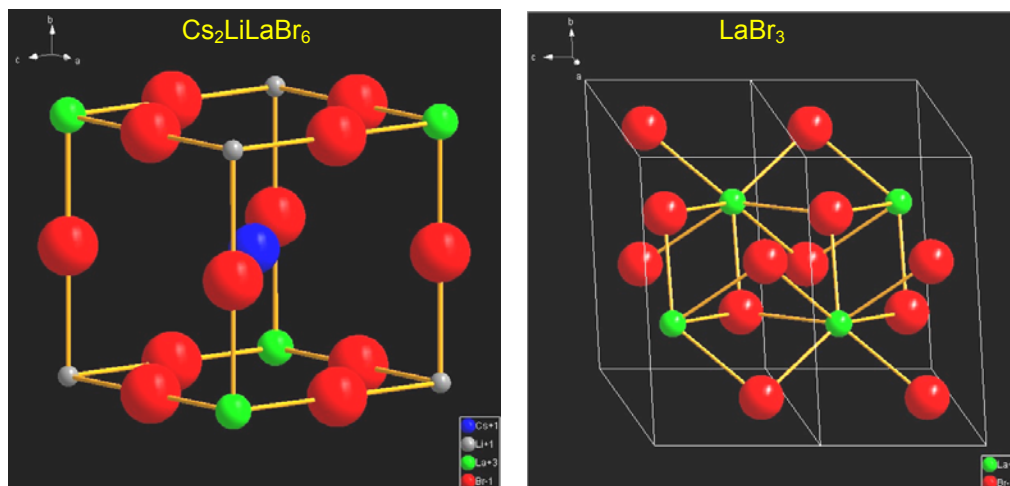


Figure 4. Illustration of isotropic, cubic structure of $\text{Cs}_2\text{LiLaBr}_6$ (left) and of highly anisotropic (hexagonal) structure of LaBr_3 (right) with La in green, Br in red, Cs in blue and Li in gray. The highly anisotropic structure (including cleavage planes) of LaBr_3 is the main reason behind the crystal growth difficulties and high cost associated with LaBr_3 . The isotropic, cubic structure for $\text{Cs}_2\text{LiLaBr}_6$ should simplify its crystal growth significantly.

6.4.2.2. Scintillation Properties of CLLB Crystals

Scintillation properties such as emission spectra, light output and decay time spectra were measured for CLLB crystals. These properties are discussed here for undoped CLLB crystals as well those with varying Ce^{3+} concentration (0.5%, 2%, 5% and 10% on molar basis).

Emission Spectra

Optical emission spectra of CLLB crystals (with 0.5%, 2%, 5% and 10% Ce^{3+} doping) were measured. Each crystal was excited with radiation from a Philips X-ray generator having a

copper target, with power settings of 40 KVp and 20 mA. The scintillation light was passed through a McPherson 0.2-meter monochromator and detected with a Hamamatsu R2059 PMT with a quartz window. The system was calibrated with a standard light source to enable correction for sensitivity variations as a function of wavelength. **Figure 5** shows normalized emission spectra for CLLB crystals with varying Ce^{3+} doping level. As seen in the figure, two peaks corresponding to $5d \rightarrow 4f$ transition of Ce^{3+} are observed in the emission spectra for Ce doped CLLB crystals. The wavelengths corresponding to the two emission peaks are 390 nm and 420 nm. It is interesting to note that the relative intensity of the 420 nm peak with respect to the 390 nm peak increases as the Ce^{3+} concentration in CLLB is increased. This may indicate that as the cerium concentration increases, some 390 nm light may be getting absorbed and then re-emitted as 420 nm light. The same two peaks were observed in undoped samples too, indicating that very small amount of Ce^{3+} contamination was present in the undoped sample, which is not surprising considering that Ce is adjacent to La in the period table.

Decay Time Spectra

The fluorescent decay time spectra of CLLB samples (undoped and with 0.5 to 10% Ce doping) were measured under 662 keV gamma-ray excitation (^{137}Cs source) at RMD. The resulting temporal response plots are shown in **Figure 6**. From multi-exponential fits to the decay plots, multiple decay components were estimated. The undoped CLLB shows a relatively slow decay time of ~ 2300 ns. For samples with Ce^{3+} doping, a 55 ns decay component was observed which was due to Ce^{3+} luminescence. Additional, longer component(s) with ≥ 270 ns time constants has also been observed (see **Table 3**). While the origin of these components is not yet established, they may be due to luminescence associated with the self trapped excitons (STE). An interesting observation that can be made from the decay plots shown in **Figure 6** is that as the Ce^{3+} concentration in CLLB increases, the relative contribution of the 55 ns component (in comparison to the longer ones) also increases. There is some evidence that rise-time is also faster for CLLB samples with higher Ce^{3+} concentration (approaching < 1 ns in CLLB samples with 10% Ce).

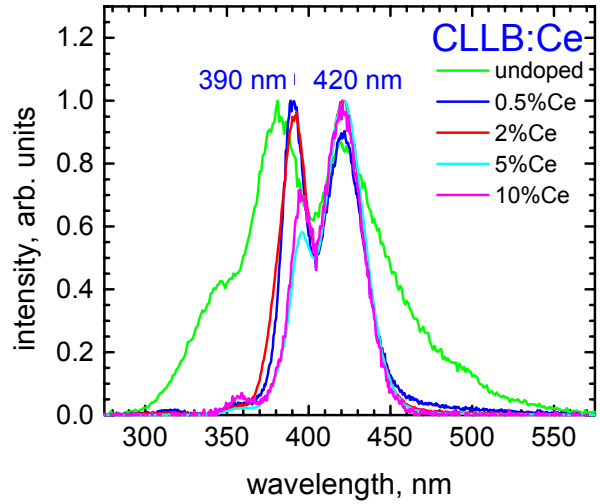


Figure 5. X-ray induced emission spectra for CLLB crystals with varying Ce^{3+} concentration.

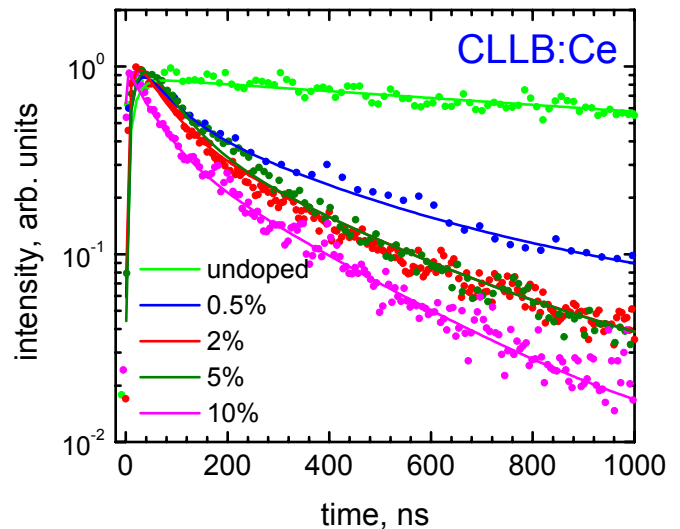


Figure 6. Decay time spectra for CLLB crystals, undoped as well as those with varying Ce^{3+} concentration (0.5%, 2%, 5% & 10%). The circles represent data points, the solid curves are multi-exponential fits to the data.

Overall, the fast risetime and the fast Ce^{3+} component (55 ns time constant) of CLLB are promising for gamma ray studies that require high timing resolution.

Light Output

The light output of CLLB crystals was measured using pulse height analysis. First, the photopeak position for thermally generated single photoelectrons in the PMT was measured for energy calibration. Next, a CLLB scintillator (with 2% Ce^{3+}), wrapped with several layers of Teflon tape, was coupled to a PMT (Hamamatsu R6233) using mineral oil and was irradiated with 60 keV gamma-rays. The PMT signal was shaped with Canberra spectroscopy amplifier (#2020) and shaping time of 4 μs was used. The pulse height spectra for single photoelectrons as well as 60 keV gamma-rays were then recorded with the Amptek

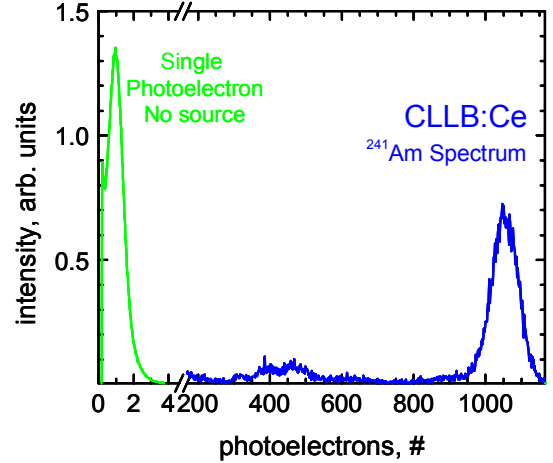


Figure 7. Estimation of light output of CLLB crystal (2% Ce^{3+} doping) coupled to a PMT by comparing its 60 keV peak position (^{241}Am source) with that for single electrons generated in the PMT photocathode. Knowing PMT quantum efficiency for CLLB emission, the light output of CLLB:2% Ce was estimated.

MCA 8000-A multichannel analyzer under same operating conditions (see **Figure 7**). By comparing these photopeak positions, the light output of the CLLB crystal with 2% Ce^{3+} doping was estimated using the known value of the quantum efficiency of the PMT for CLLB emission. Using such approaches, we have estimated the light output of CLLB:2%Ce to be as high as 60,000 photons/MeV. This light yield is $\sim 60\%$ higher than the light yield of NaI:Tl, one of the most common scintillators for gamma-rays at present. The light yield of CLLB:2%Ce also approaches the reported values for the emerging $\text{LaBr}_3\text{:Ce}$ scintillators, which is very encouraging.

The light output measurements were also conducted with other CLLB crystals, undoped as well as those with a wide range of Ce doping (0.5%, 2%, 5% and 10%). ^{137}Cs spectra were recorded for various CLLB crystals (see **Figure 8**) with the same PMT (Hamamatsu R6233).

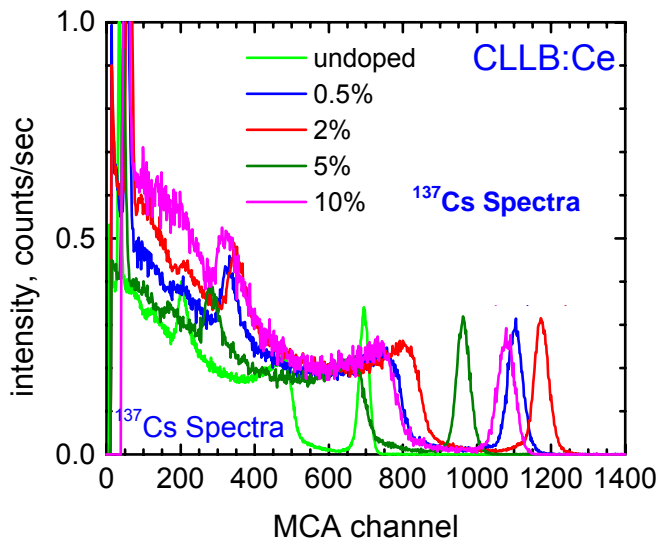


Figure 8. ^{137}Cs spectra recorded with CLLB crystals with varying Ce^{3+} concentration for estimation of their light yield.

The relative position of the 662 keV photopeak for each CLLB crystal in comparison to that for CLLB with 2% doping (with light output of 60,000 photons/MeV) was used for estimation of light output of various CLLB samples (undoped, 0.5%, 5% and 10%). The results are presented in **Table 3**. While the light yield of the undoped CLLB crystal is low ($\sim 35,500$ photons/MeV), all Ce^{3+} doped CLLB crystals show high light output ($> 50,000$ photons/MeV). The highest light output was observed for CLLB with 2% doping. Even at Ce^{3+}

doping level as high as 10%, light output remained reasonably high, ~55,000 photons/MeV, indicating that concentration quenching effects are limited.

The 662 keV energy resolution in the ^{137}Cs spectra recorded with CLLB:Ce crystals (shown in **Figure 8**) was measured to be as high as 3.4% (FWHM), which is impressive and is about two times better than that for NaI:Tl. However, it is important to note that the crystal surface finish (on sides) and the overall experimental setup was not optimized for energy resolution in this study and detailed energy resolution results with CLLB scintillators over a wider range of gamma-ray energies are presented in a later section.

A summary of scintillation properties of CLLB samples (undoped and with Ce^{3+} doping in 0.5 to 10% range) is presented in **Table 3**. The main conclusions are that CLLB with Ce doping shows impressive scintillation properties with high light output of up to ~60,000 photons/MeV and fast decay time of ~55 ns. The doping level of 2% Ce has provided highest light output so far, though additional studies will be conducted for optimization. Next, gamma-ray detection characteristics of CLLB crystals are discussed.

Table 3. Scintillation Properties of Various CLLB Crystals

<i>Doping</i>	<i>Light Output (photons/MeV)</i>	<i>Decay Time(s) (ns)</i>	<i>Peak Emission (ns)</i>
Undoped	35,500	2300	390, 420
0.5% Ce^{3+}	56,200	55 ns (19%), ≥ 270 ns (81%)	390, 420
2% Ce^{3+}	60,000	55 ns (27%), ≥ 270 ns (73%)	390, 420
5% Ce^{3+}	50,000	55 ns (33%), ≥ 270 ns (67%)	390, 420
10% Ce^{3+}	55,000	55 ns (53%), ≥ 270 ns (47%)	390, 420

6.4.2.3. Gamma Ray Detection with CLLB:Ce Scintillators

Once the scintillation properties of CLLB:Ce were evaluated, their gamma-ray detection performance was characterized. This involved measurement of energy resolution and timing resolution. These studies were conducted with CLLB crystals with 2% Ce doping in view of their high light output and reasonably fast response.

Room Temperature CLLB:Ce Energy Resolution Measurements

The energy resolution of CLLB:Ce scintillators for gamma-rays has been evaluated. This involved coupling an unpackaged CLLB:Ce scintillator (~1 cm³ size, 2% Ce) to a photomultiplier tube (with an enhanced QE bialkali photocathode and a quartz window, Hamamatsu R6233S). The polished scintillator was coated with Teflon tape to maximize the light collection. The scintillator was irradiated with 662 keV γ -rays (^{137}Cs source), and the resulting PMT signal was processed with a preamplifier (Canberra #2005), and then shaped with a spectroscopy amplifier (Canberra #2022). The resulting ^{137}Cs pulse height spectrum, recorded with shaping time of 4 μs , was shown earlier in **Figure 3**. Energy resolution for the 662 keV peak was computed to be about 2.9% (FWHM) at room temperature, which is amongst the best recorded resolution for scintillator based systems. The energy resolution of CLLB:2%Ce is almost 2.4 times better than that for NaI:Tl and it is comparable to that achieved with emerging LaBr₃:Ce scintillators.

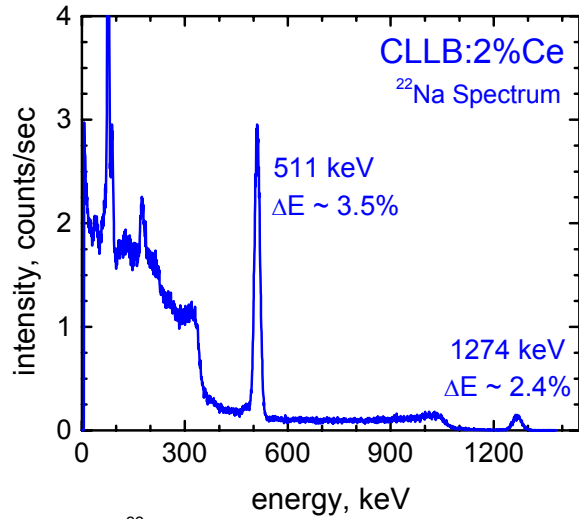


Figure 9. ^{22}Na spectrum (511 and 1275 keV γ -rays) recorded with CLLB:2%Ce crystal coupled to a PMT (Hamamatsu R6233S).

energy resolution of 122 keV photopeak was recorded to be 5.8% (FWHM). These results are indeed very encouraging and are significantly superior to that for NaI:Tl. For example, the energy resolution of NaI:Tl at 122 keV is $\sim 9\%$ (FWHM) as shown in **Figure 10**.

The high energy resolution of CLLB:2%Ce is due to its high proportionality (which was illustrated earlier in **Figure 2**) over a wide energy range and its high light output. We expect to further improve the energy resolution of the CLLB:Ce scintillators by optimizing the light collection, and by improving their overall quality.

Analysis of Energy Resolution of CLLB:Ce Scintillators

For 662 keV spectra shown in **Figure 3**, we have analyzed the photopeak resolution of CLLB:2%Ce and NaI:Tl crystals to determine the contribution of various components to the overall photopeak broadening. The energy resolution of a scintillator-PMT spectrometer can be expressed as follows [van Eijk 01]:

$$(\Delta E/E)^2 = R^2 = R_{phe}^2 + R_{sci}^2 + R_{noise}^2 \quad (1)$$

R_{phe} represents the resolution broadening due to the photoelectron statistics (including the excess noise effects, arising from the variance in the photodetector gain). R_{sci} represents broadening due to non-ideal nature of scintillators. This parameter includes contribution of nonproportionality as well as other parameters such as crystal inhomogeneities. Finally, the electronic noise effects in the scintillation detection system are included in the final term, R_{noise} . For PMT readout, the last term, R_{noise} can be ignored due to PMT's negligible electronic noise contribution, though R_{noise} has to be included in case of solid-state photodetectors (such as silicon

The ^{22}Na energy spectrum has also been recorded with the same CLLB:2%Ce crystal-PMT setup and its energy resolution for 511 keV and 1275 keV gamma-rays was estimated to be 3.5% (FWHM) and 2.4% (FWHM), respectively at room temperature as shown in **Figure 9**.

To determine the potential of CLLB:Ce in SPECT imaging, we also conducted measurements using a ^{57}Co source because the gamma-emission from ^{57}Co (122 keV) is very similar to that for common SPECT radioisotopes (e.g. ^{99m}Tc which emits at 140 keV gamma-rays). ^{57}Co energy spectrum was recorded with the same CLLB:2%Ce crystal-PMT setup. As shown in **Figure 10**, the

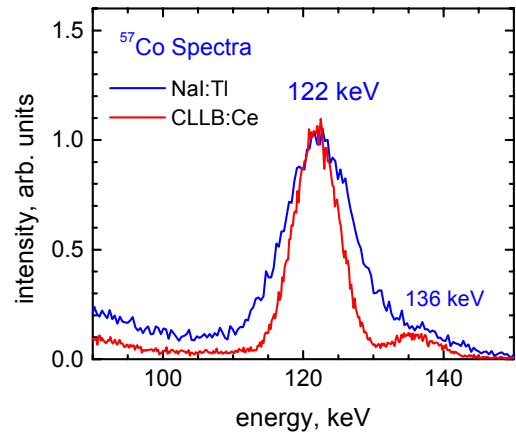


Figure 10. ^{57}Co spectra collected with CLLB:2%Ce and NaI:Tl crystals. The energy resolution of CLLB:2%Ce for 122 keV gamma-rays is 5.8% (FWHM), while that of NaI:Tl is $\sim 9\%$ (FWHM).

p-i-n diodes and Si-APDs). It is possible to estimate the contribution of the first term, R_{phe} , by estimating the number of photoelectrons (N_{phe}) generated in the photodetector for a gamma-ray event in the scintillator. N_{phe} can be estimated using the following expression:

$$N_{phe} \approx N_{ph} \bullet E_{\gamma} \bullet \eta_{det} \quad (2)$$

where, N_{ph} is the light output of the scintillator (in photons/MeV), which is 60,000 photons/MeV for CLLB:2% Ce (as shown in **Table 3**), E_{γ} is energy of the incident gamma-ray in MeV (0.662 in this case) and η_{det} is the quantum efficiency of the photodetector over the emission spectrum of the scintillator (including the light collection efficiency). Once N_{phe} is known, the resolution broadening due to R_{phe} , representing variance in photoelectron statistics, can be estimated using the traditional Poisson distribution:

$$R_{phe}^2 = (2.36)^2 [ENF/N_{phe}] \quad (3)$$

where, ENF is the excess noise factor of the photodetector (~ 1.15 for PMTs). Using this framework, it is possible to estimate N_{phe} and R_{phe} from the known parameters of the scintillator and PMTs using equations (2) and (3). Then using the measured value of R (or $\Delta E/E$) and R_{noise} (≈ 0 for PMT readout) and, R_{sci} can be back calculated using equation (1). Using this framework, the 662 keV energy resolution of various spectrometers such as NaI(Tl)-PMT, CLLB-PMT was analyzed and the results are presented in **Table 4**.

Table 4. Analysis of the 662 keV Energy Resolution of Scintillator Spectrometers

<i>Detector</i>	<i>N_{phe} at 0.662 MeV</i> <i>(electrons)</i>	<i>R (%)</i> <i>FWHM</i>	<i>R_{phe} (%)</i> <i>FWHM</i>	<i>R_{sci} (%)</i> <i>FWHM</i>	<i>R_{noise}(%)</i> <i>FWHM</i>
NaI(Tl)-PMT	7,000	7	3.0	6.3	0
CLLB:2%Ce-PMT	11,000	2.9	2.4	1.62	0

The overall energy resolution R at 662 keV energy was measured to be 7% (FWHM) for NaI(Tl) coupled to PMT (as shown in **Figure 3**), while R_{phe} was estimated to be 3.0% (FWHM) using equation (3). R_{sci} was then calculated to be 6.3% (FWHM) from equation (1) by assuming that R_{noise} is negligible for PMT readout. Similar analysis of a CLLB:2%Ce crystal coupled to a PMT (Hamamatsu R6233S) has been performed and the results are listed in **Table 4**. As shown in **Figure 3**, the energy resolution, R , of CLLB:2%Ce-PMT at 662 keV was measured to be 2.9% (FWHM). R_{phe} for CLLB-PMT was calculated to be 2.4% (FWHM) from the known values of light output, incident γ -ray energy and PMT quantum efficiency. R_{sci} was then estimated to be 1.62% (FWHM). This study illustrates that due to its highly proportional response (see **Figure 2**), the photoelectron statistics (or R_{phe}) is the main broadening component for CLLB:Ce. In case of NaI(Tl), the non-ideal nature of the scintillator (or R_{sci}) is the dominant component due to highly non-proportional response (see **Figure 2**). This would indicate that as the scintillator light collection is improved, further improvement in energy resolution of CLLB:Ce should be possible.

Coincidence Timing Resolution

Coincidence timing resolution of CLLB:Ce crystals has been measured at RMD. This experiment involved irradiating a BaF₂ “reference” scintillator and a CLLB:Ce “test” scintillator

each coupled to a fast PMT (Hamamatsu H-6610) with 511 keV positron annihilation γ -ray pairs (emitted by a ^{22}Na source). The BaF_2 -PMT detector formed a “start” channel in the timing circuit, while the CLLB:Ce-PMT detector formed the “stop” channel. The signal from each detector was processed using a constant fraction discriminator and then fed into a time-to-amplitude converter (TAC) with a fixed delay added to the “stop” channel. The resulting timing distribution was recorded on a multi-channel analyzer. **Figure 11** shows a coincidence timing resolution plot acquired at room temperature in this manner with CLLB:Ce and BaF_2 scintillators and the timing resolution was measured to be 325 ps (FWHM). These results indicate that CLLB:Ce may provide time-of-flight (TOF) capability. The timing resolution of two BaF_2 detectors operating in coincidence was about 210 ps (FWHM). No energy gating was applied in these studies. Further improvement in CLLB timing resolution should be possible with energy gating as well as optimization of crystal quality and its doping level. While timing resolution is not important in SPECT, high timing resolution of CLLB:Ce improves its scope for broader utilization in nuclear physics and active interrogation studies for homeland defense as well as in specific cases for combined SPECT-PET imaging.

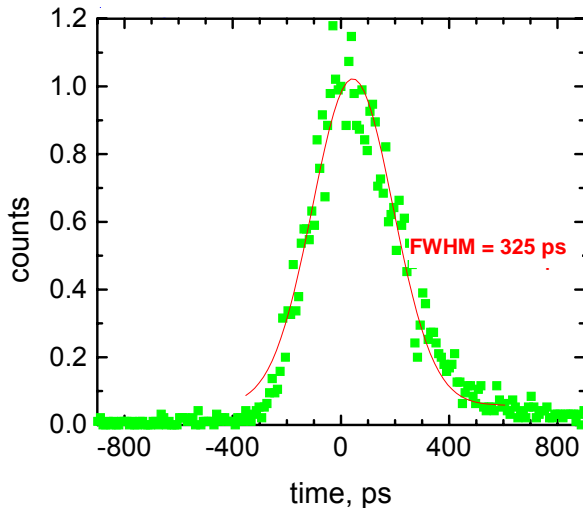


Figure 11. Timing resolution of a CLLB:Ce crystal showing normalized counts versus time.

Overall, these measurements clearly indicate that CLLB:Ce is a promising scintillator. It has high light output, fast response and shows excellent energy and timing resolution. The most promising aspects of CLLB for SPECT include its high light output, high proportionality and excellent energy resolution in the energy region of interest for SPECT. Its cubic crystal structure and low melting point indicate that the scale-up of this scintillator should be substantially easier compared to the lanthanum bromide scintillators and related rare earth trihalide compositions.

6.5 Eu^{2+} DOPED ALKALINE EARTH HALIDE SCINTILLATORS

6.5.1. Overview:

In this section we present our recent investigation of strontium iodide doped with Eu^{2+} as a scintillation material which has been carried out in collaboration with research groups at Lawrence Livermore National Laboratory (LLNL). SrI_2 belongs to the alkaline-earth iodide family. Some reports of scintillation from compositions belonging to alkaline-earth iodide family can be found in literature, originating from the work of Hofstadter on calcium iodide in 1960's [Hofstadter 64]. Calcium iodide exhibits very high light yield ($\geq 80,000$ photons/MeV) and it can be activated with various dopants such as Tl^+ and Eu^{2+} . However, CaI_2 has hexagonal, layered crystal structure and is very prone to basal cleavage [Hofstadter 64], which makes large volume growth of CaI_2 crystals very challenging. Hofstadter also reported scintillation from SrI_2 doped with Eu with light yield approaching that for NaI:Tl [Hofstadter 68], though very few subsequent publications can be found on this scintillator. Some reports on BaI_2 doped with Eu^{2+}

have also appeared in literature [Selling], though the reported light yield was not encouraging (only few thousand photons/MeV). In recent years, this class of materials has been largely ignored for scintillation studies.

We have recently undertaken an investigation of alkaline earth iodide compositions, particularly, SrI_2 doped with Eu^{2+} [Shah 09, van Loef 08, Wilson, Cherepy, Burger]. The hypothesis in this exploration is that since $\text{CaI}_2:\text{Eu}$ has already shown excellent light yield (but faces difficulties in large volume growth due to its hexagonal structure that is prone to cleavage), upon optimization, other alkaline earth iodides such as $\text{SrI}_2:\text{Eu}$ (which do not have layered crystal structure and therefore, do not cleave readily), may show scintillation performance similar to $\text{CaI}_2:\text{Eu}$ without the associated difficulties in crystal growth. Crystals of $\text{SrI}_2:\text{Eu}$ were grown at RMD by Bridgman method and their scintillation properties were evaluated, as discussed in detail in the next section. Limited evaluation of other binary and ternary alkaline earth halides with Eu^{2+} doping has also been performed and the results are summarized in a later section of this chapter.

6.5.2 Evaluation of $\text{SrI}_2:\text{Eu}$

6.5.2.1. Crystal Growth Aspects

SrI_2 is an orthorhombic composition (see **Figure 12**) belonging to alkaline-earth iodide family with density of 4.6 g/cm^3 . The melting point of SrI_2 is 540°C . In view of congruent melting of SrI_2 at relatively low temperature, we have produced crystals of this material using the



Figure 13a. Photograph of a $\text{SrI}_2:\text{Eu}$ crystal grown at RMD with 1 cm diameter, 2.4 cm length.

Bridgman process at RMD. Evacuated quartz ampoules were used as crucibles. SrI_2 crystals ($\sim 1 \text{ cm}^3$ and larger, doped with 0.5% to 10% Eu^{2+} on molar basis) were initially produced in our study. **Figures 13a & 13b** show photographs of $\text{SrI}_2:\text{Eu}^{2+}$ crystals grown at RMD. Due to the hygroscopic nature of these materials, they need to be protected from prolonged

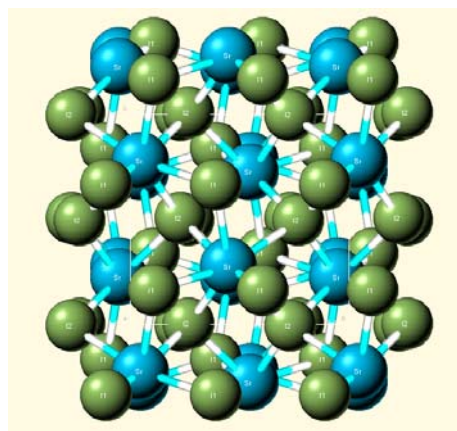


Figure 12. Illustration of orthorhombic crystal structure of SrI_2 ($a = 15.22 \text{ \AA}$, $b = 8.22 \text{ \AA}$, $c = 7.9 \text{ \AA}$, all angles between axes equal 90°). View down A-axis is shown.

exposure to moisture. Most of our studies were performed in moisture free chambers or with protected crystals. The scintillation properties of $\text{SrI}_2:\text{Eu}$ are discussed here. Few crystals of SrI_2 with Ce^{3+} doping were also grown and evaluated in our study.

6.5.2.2. Scintillation Properties of $\text{SrI}_2:\text{Eu}^{2+}$

Small crystals of $\text{SrI}_2:\text{Eu}$ (0.5 to 1 cm^3 size, doped with 0.5 to 8% Eu^{2+} on molar basis) were cut and polished from Bridgman grown boules. These crystals were characterized using X and γ -rays to



Figure 13b. Photograph of a $\text{SrI}_2:\text{Eu}$ crystal grown at RMD with 1" diameter, $\sim 2"$ length.

measure their emission and decay spectra as well as light output [Shah 09, van Loef 08, Wilson].

Emission Spectra

Optical emission spectra of the $\text{SrI}_2:\text{Eu}$ scintillators were measured at RMD. Each crystal was excited with radiation from a Philips X-ray tube having a copper target, with power settings of 30 KVp and 15 mA. The scintillation light was passed through a McPherson 0.2-meter monochromator and detected with a Hamamatsu C31034 PMT with a quartz window. The system was calibrated with a standard light source to correct for sensitivity variations as a function of wavelength. **Figure 14** shows the normalized emission spectrum for the $\text{SrI}_2:\text{Eu}$ crystal (0.5% Eu^{2+} doping) grown at RMD. As seen in the figure, the emission from $\text{SrI}_2:\text{Eu}$ occurs over a single, narrow band (420-480 nm), which is due to $d \rightarrow f$ transition of Eu^{2+} . The wavelength of maximum emission (λ_{max}) is 430 nm for $\text{SrI}_2:\text{Eu}$. Emission studies of SrI_2 crystals with higher Eu^{2+} doping (up to 10% Eu) were also conducted and the results were similar to that in **Figure 14**, though a slight shift to higher wavelengths was observed as the Eu^{2+} concentration increased (see **Table 5**). For example, the peak emission wavelength for SrI_2 with 10% Eu doping was measured to be ~435 nm (see **Table 5**). Emission spectra of Ce^{3+} doped SrI_2 crystals were also measured in similar manner and luminescence due to $d \rightarrow f$ transition of Ce^{3+} was observed with emission peaks at 405 and 430 nm. The emission spectra in **Figure 14** are normalized but in the raw data the emission intensity of Ce doped SrI_2 was substantially lower.

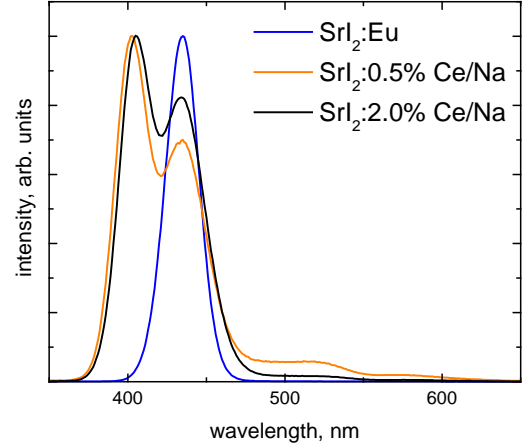


Figure 14. X-ray excited optical emission spectra of $\text{SrI}_2:\text{Eu}$ and $\text{SrI}_2:\text{Ce}$ crystals.

Decay Time Spectra

The fluorescent decay time spectrum of a SrI_2 crystal (with 5% Eu^{2+} doping) under 511 keV gamma-ray excitation (^{22}Na source) was measured at RMD [Bollinger]. The result is shown in **Figure 15**. From an exponential fit to the data, the principal decay time constant was estimated to be ~1.1 μs , which is attributed to Eu^{2+} luminescence. A single component fit is sufficient to cover much of the recorded emission. Decay studies were also conducted for small SrI_2 crystals with a fairly wide range of Eu^{2+} concentrations (0.5% to 10% Eu^{2+} doping) and the decay-times were found to increase with the increasing Eu^{2+} concentration as shown in **Table 5**. Decay time studies were also conducted with 0.5% Ce^{3+}

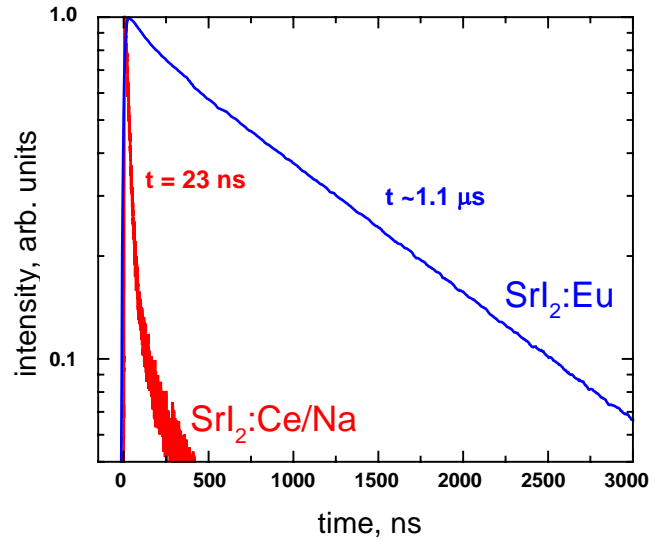


Figure 15. Decay time spectra of $\text{SrI}_2:\text{Eu}$ and $\text{SrI}_2:\text{Ce}$.

doped SrI_2 crystal (see **Figure 15**). The response shows a fast component with a decay constant of ~ 23 ns and a longer component with ~ 160 ns time constant.

3. Light Output Measurements

The light output of RMD grown $\text{SrI}_2:\text{Eu}$ crystals was measured using pulse height analysis. First, the photopeak position for thermally generated single photoelectrons in the PMT was measured for energy calibration. Next, a $\text{SrI}_2:\text{Eu}$ scintillator (with 5% Eu^{2+}), wrapped with several layers of Teflon tape, was coupled to the PMT using mineral oil and was irradiated with 60 keV gamma-rays. The PMT signal was shaped with Canberra spectroscopy amplifier (#2020) and shaping time of 4 μs was used. The pulse height spectra for single photoelectrons as well as 60 keV gamma-rays were then recorded with the Amptek MCA 8000-A multichannel analyzer under same operating conditions (see **Figure 16**). By comparing these photopeak positions, the light output of the SrI_2 crystal with 5% Eu^{2+} doping was estimated using the known value of the quantum efficiency of the PMT for $\text{SrI}_2:\text{Eu}^{2+}$ emission. Using this approach, we estimate the light output of $\text{SrI}_2:\text{Eu}^{2+}$ to be $\geq 100,000$ photons/MeV, which is remarkable. This light output is ~ 2.6 times higher than NaI:Tl and about 50% higher than $\text{LaBr}_3:\text{Ce}$ and is amongst the highest reported values for inorganic scintillators. High light output is important because in combination with proportionality of response, it governs energy resolution of the scintillator. Similar measurements were conducted for SrI_2 crystals with varying Eu^{2+} concentration and the results (shown in **Table 5**) indicate that the highest light output is achieved in SrI_2 at $\sim 5\%$ Eu^{2+} doping.

It is important to note that the response of $\text{SrI}_2:\text{Eu}$ has been observed to become slower as the crystal size increases (for fixed Eu^{2+} doping level) and as the Eu^{2+} doping level increases (for similar crystal sizes) due to light trapping associated to the Eu^{2+} activator [Glodo 09]. The time constants reported below are for relatively small crystal sizes. The effect of this light trapping on the energy resolution can be corrected using digital pulse processing and dedicated algorithms [Burger].

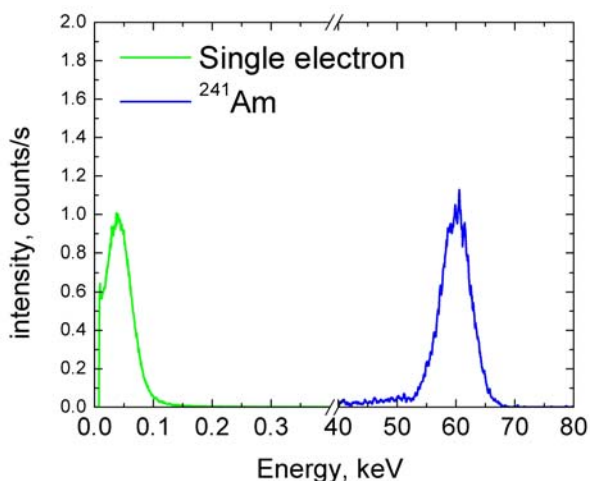


Figure 16. Estimation of light output of SrI_2 crystal (5% Eu^{2+} doping) coupled to a PMT by comparing its 60 keV peak position (^{241}Am source) with that for single electrons generated in the PMT photocathode. Knowing PMT quantum efficiency for $\text{SrI}_2:\text{Eu}$ emission, the light output of $\text{SrI}_2:5\% \text{Eu}$ was estimated to be $\geq 100,000$ photons/MeV.

Table 5. Scintillation Properties of SrI_2 with Different Eu^{2+} Concentrations

Eu^{2+} Concentration(%)	Light Output (photons/MeV)	Decay Time(s) (ns)	Emission Peak (nm)
0.5	78,000	620	429
2	92,000	900	431
5	100,000	1100	433
10	84,000	1650	436

Gamma-Ray Energy Resolution

^{137}Cs spectrum was recorded with $\text{SrI}_2:5\%\text{Eu}^{2+}$ crystal ($\leq 1\text{ cm}^3$ in size) coupled to a PMT (Hamamatsu R6233S), which is shown in **Figure 17**. The measured photopeak was fit to a Gaussian to evaluate the full-width-at-half-maximum (FWHM) to estimate the energy resolution. The energy resolution of $\text{SrI}_2:5\%\text{Eu}^{2+}$ crystal at 662 keV was estimated to be $\sim 2.7\%$ (FWHM) as shown in **Figure 17**. This energy resolution is more than two times higher than NaI:Tl and is very similar to for the state-of-the-art $\text{LaBr}_3:\text{Ce}$ crystals. At 122 keV γ -energy (^{57}Co source), the energy resolution of $\text{SrI}_2:\text{Eu}$ ($\sim 5.3\%$ FWHM, see **Figure 18**) is better than that for all the scintillators that we have evaluated at RMD. Since the energy of gamma-rays emitted by $^{99\text{m}}\text{Tc}$ (the most common radioisotope used in SPECT) is 140 keV, very similar to the 122 keV gamma-rays emitted by ^{57}Co , the results presented in **Figure 18** confirm the promise of $\text{SrI}_2:\text{Eu}$ in SPECT.

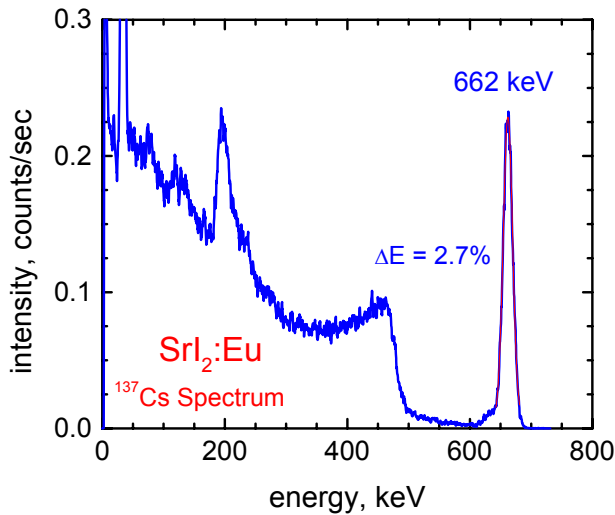


Figure 17. ^{137}Cs spectrum recorded with a $\text{SrI}_2:5\%\text{Eu}$ crystal coupled to a PMT.

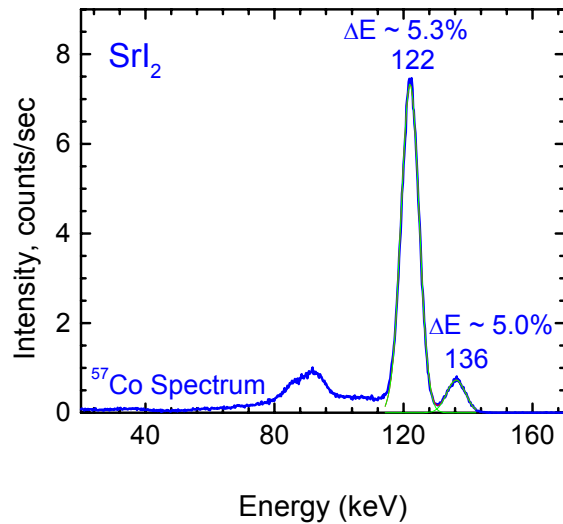


Figure 18. ^{57}Co spectrum (122 keV gamma-rays) with a $\text{SrI}_2:5\%\text{Eu}$ crystal coupled to a PMT.

Proportionality Studies

In addition to high light output, a scintillator needs to exhibit highly proportional response in order to demonstrate high energy resolution. As discussed here, we have characterized proportionality of response of $\text{SrI}_2:\text{Eu}$.

We have measured light output of $\text{SrI}_2:5\%\text{Eu}$ under excitation from isotopes such as ^{241}Am (60 keV γ -rays), ^{57}Co (122 keV γ -rays), ^{22}Na (511 keV and 1275 keV γ -rays) and ^{137}Cs (662 keV γ -rays). Pulse height measurements were performed using standard NIM equipment with the scintillator exposed to different isotopes. Same settings were used for PMT and pulse processing electronics for each isotope. From the measured peak position and the known γ -ray energy for each isotope, the light output (in photons/MeV) at each γ -ray energy was estimated. The data points were then normalized with respect to the light output value at 662 keV energy. **Figure 19** shows the relative light yield as a function of electron energy for $\text{SrI}_2:\text{Eu}$, compared to that of NaI:Tl, CLLB and $\text{LaBr}_3:\text{Ce}$. The proportionality of the light yield is excellent for $\text{SrI}_2:\text{Eu}$, and thus the contribution to energy resolution due to nonproportionality is expected to be small for $\text{SrI}_2:\text{Eu}$. It is important to note that $\text{SrI}_2:\text{Eu}$ is even more proportional than $\text{LaBr}_3:\text{Ce}$, particularly

at low energies. This in combination with very high light yield of $\text{SrI}_2:\text{Eu}$ indicate that as crystals with adequate quality become available, further improvement in the energy resolution of $\text{SrI}_2:\text{Eu}$ should be possible. Addressing the light-trapping issues associated to Eu^{2+} activator will be important in achieving high energy resolution with large $\text{SrI}_2:\text{Eu}$ crystals.

6.5.3. Summary of Scintillation Properties of Other Alkaline Earth Halides

We have also analyzed other similar alkaline earth halide compositions, $\text{BaI}_2:\text{Eu}$, $\text{CaI}_2:\text{Eu}$, $\text{SrBr}_2:\text{Eu}$, $\text{BaBr}_2:\text{Eu}$, as well as a ternary composition, $\text{Ba}_x\text{Sr}_{1-x}\text{I}_2:\text{Eu}$. Small crystals ($\leq 1 \text{ cm}^3$) of these compositions were grown using the Bridgman method. These crystals were cut and polished. Scintillation properties such as emission spectrum, light yield, and decay time were measured using the techniques described in the earlier sections. The results, presented in **Table 6**, indicate that while the light output of $\text{BaI}_2:\text{Eu}$, $\text{SrBr}_2:\text{Eu}$ and $\text{BaBr}_2:\text{Eu}$ is rather low, $\text{CaI}_2:\text{Eu}^{2+}$ shows bright luminescence, though its hexagonal layered crystal structure makes the growth of large crystals difficult. The ternary, $\text{Ba}_x\text{Sr}_{1-x}\text{I}_2:\text{Eu}$, has an orthorhombic structure and shows reasonable scintillation properties including bright luminescence.

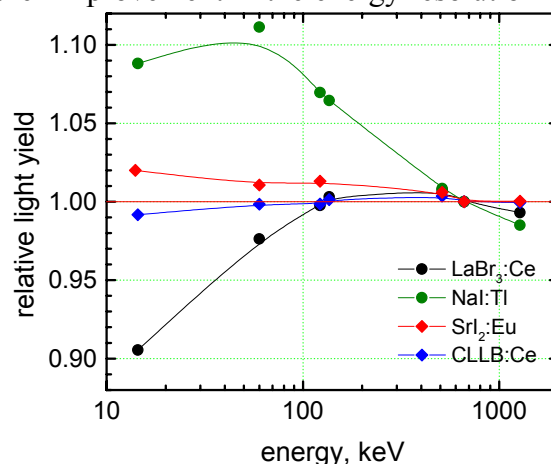


Figure 19. Proportionality of response for various scintillators measured at RMD using different isotopic sources.

Table 6. Properties of Other Alkaline Earth Halide Scintillators

Material	Light Output [Photons/MeV]	Wavelength of Maximum Emission [nm]	Principal Decay Time [ns]
$\text{SrI}_2:5\%\text{Eu}$	100,000	433	1100
$\text{BaI}_2:0.5\%\text{Eu}$	26,000	430	450
$\text{CaI}_2:0.5\%\text{Eu}$	>100,000	470	1150
$\text{SrBr}_2:0.5\%\text{Eu}$	26,000	415	720
$\text{BaBr}_2:0.5\%\text{Eu}$	11,500	410	560
$\text{Ba}_x\text{Sr}_{1-x}\text{I}_2:\text{Eu}$	~100,000	435	>1000

6.6 REFERENCES

- C. Alexander and E. Oberhausen. *Myocardial scintigraphy*, Semin Nucl Med **25**: 195-201 (1995).
- D.S. Berman, H. Kiat, et al. *Dual-isotope myocardial perfusion SPECT with rest thallium-201 and stress Tc-99m sestamibi*, Cardiol Clin **12**: 261-270 (1994).
- A. Bessiere, P. Dorenbos, C. W. E. van Eijk, K. W. Krämer, and H. U. Güdel, *Nucl. Instr. and Meth. A.*, **537**, 242-246 (2005).
- M. D. Birowosuto, P. Dorenbos, C. W. E. van Eijk, K. W. Krämer, and H. U. Güdel, *J. Phys-Condensed Matter*, **18**, 6133-6148 (2006).
- L. M. Bollinger and G. E. Thomas, *Measurement of the time dependence of scintillation intensity by a delayed-coincidence method*, Rev Sci Instr, vol. 32, pp. 1044, (1961).

- A. Burger et. al., Recent Developments in Strontium Iodide Detectors, Presented at IEEE NSS/MIC, Orlando, Oct. (2009).
- N. Cherepy, G. Hull, A. D. Drobshoff, S. A. Payne, E. van Loef, C. M. Wilson, K. S. Shah, *et. al.*, Strontium and Barium Iodide High Light Yield Scintillators, manuscript submitted to Applied Physics Letters, Nov. (2007).
- SR Cherry, JA Sorenson, ME Phelps: **Physics in Nuclear Medicine**, Third Edition, W.B. Saunders, Philadelphia, (2003).
- W.-S. Choong, K. M. Vetter, W. W. Moses, G. Hull, S. A. Payne, N. J. Cherepy, and J. D. Valentine, Design of a Facility for Measuring Scintillator Non-Proportionality, Submitted to IEEE Trans. Nuc. Sci. (2007).
- W. Cross "On minerals of the cryolite group recently found in Colorado," W.F. Hillebrand, Am. J. Sci. 26, 271, (1883)
- P. Dorenbos, *Light output and energy resolution of Ce³⁺ doped scintillators*, Nucl. Instr. and Meth., accepted for publication, (2001).
- P. Dorenbos, *et. al.*, *Non-Proportionality in the Scintillation Response and the Energy Resolution Obtainable with Scintillation Crystals*, IEEE Trans. Nuc. Sci., 42(6), p. 2190, (1995).
- J. Glodo, E.V.L. van Loef, N. Cherepy, S.A. Payne, C.M. Wilson, K.S. Shah, Concentration Effects in Doped SrI₂, Presented at SCINT 2009, Jeju, S. Korea, June (2009).
- J. Glodo, E. V. D. van Loef, W. M. Higgins, and K. S. Shah, *IEEE Nucl. Sci. Symposium Conference Record*, 1208-1211 (2006).
- J.A. Heanue, **Detector and Electronics Design Considerations for an Emission-Transmission Medical Imaging System**, Ph.D Dissertation, Univ. of California San Francisco, June (1996).
- J. Heo, I. Wolmer, et al., *Sequential dual-isotope SPECT imaging with thallium-201 and technetium-99m sestamibi*, J Nucl Med **35**: 549-553 (1994).
- R. Hofstadter, E. W. O'Dell, and S. T. Schmidt, IEEE Trans. Nucl. Sci. NS-11, 12 (1964).
- R. Hofstadter, "Europium-activated Strontium Iodide Scintillators," US Patent 3,373,279 (1968).
- L.L. Johnson, K. S. Lerrick, et al., *Measurement of infarct size and percentage myocardium infarcted in a dog preparation with single photon-emission computed tomography, thallium-201, indium-111 monoclonal antimyosin Fab.*, Circulation **76**: 181-190 (1987).
- L.L. Johnson, D. W. Seldin, et al., *Dual-isotope thallium and indium antimyosin SPECT imaging to identify acute infarct patients for further ischemic risk*, Circulation **81**: 37-45 (1990).
- H. Kiat, G. Germano, et al., *Comparative feasibility of separate vs. simultaneous rest thallium-201/stress technetium-99m-sestamibi dual-isotope myocardial perfusion SPECT*, J Nucl Med **35**: 524-528 (1994).
- P. Liu, R. J. Burns, et al., *Validation of cardiac single photon emission tomography of labeled intracoronary microspheres as a method to measure changes in distribution of coronary blood flow*, Can J Cardiol **6**: 362-367 (1986).
- J. Maddahi, E. Rodrigues, et al., *State-of-the-art myocardial perfusion imaging*, Cardiol Clin **12**: 199-222 (1994).
- G. Meyer "The Synthesis and structures of complex rare-earth halides," Prog. Sol. St. Chem. 14, 141-219, (1982)

- W.W. Moses, *Current Trends in Scintillator Detectors and Materials*, Nucl. Inst. And Meth., A 487, p. 123-128, (2002).
- J. Selling, M. D. Birowosuto, P. Dorenbos, S. Schweizer, J. Appl. Phys., 101, 034901 (2007).
- K.S. Shah, *et. al.*, *New Scintillators for SPECT*, Presented at SPIE Annual Meeting, San Diego, August, (2009).
- K.S. Shah, J. Glodo, W. Higgins, E.V.D. van Loef, *Search of Cerium Activated Scintillators based on Rare Earth Trihalide Compositions*, Presented at IEEE NSS, Honolulu, Oct. (2007)
- K.S. Shah, J. Glodo, W.W. Moses, S.E. Derenzo, M.J. Weber, "*LaBr₃:Ce Scintillators for γ -Ray Spectroscopy*," *IEEE Trans. Nuc. Sci.*, V50(6), p. 2410, (2003).
- C.W.E. van Eijk, J.T.M. de Haas, P. Dorenbos, K.W. Krämer, H.U. Güdel "*Novel inorganic thermal-neutron scintillators*,"in: Proc. SCINT 2005, Alushta, Crimea, Ukraine, Sep. 19-23, 2005, pp. 86-88 (2005)
- C.W.E. van Eijk, New inorganic scintillators – aspects of energy resolution, Nuc. Inst. and Meth. in Phys. Res. A 471 pp.244-248, (2001).
- E. V. van Loef, Cody M. Wilson, Jarek Glodo, Nerine J. Cherepy, Giulia Hull, Stephen A. Payne, Woon-Seng Choong, William W. Moses, Kanai S. Shah, *Crystal Growth and Scintillation Properties of Strontium Iodide Scintillators*, Presented at SORMA West Workshop, May, 2008
- E.V. D. van Loef, J. Glodo, W. M. Higgins and K. S. Shah, *IEEE Nucl. Sci.*, **52**, 1819-1822 (2005).
- E.V.D. van Loef, P. Dorenbos, and C.W.E. van Ejik, K. Kramer, and H.U. Gudel, *High Energy Resolution Scintillator: Ce³⁺ Activated LaBr₃*, Appl. Phys. Lett., 79(10), p.1573, (2001).
- C. Wilson, E.V.D. van Loef, J. Glodo, N. Cherepy, S. Payne, K.S. Shah, *Scintillation Properties of Alkaline Earth Halide Crystals*, Presented at IEEE NSS/MIC, Dresden, Oct. (2008)
- P. Yang, P. Doty *et. al.*, *Structure and Properties of Elpasolite Halide Scintillators*, Presented at MRS Spring Meeting, San Francisco, April, (2009)

Chapter 7: Position Sensitive Avalanche Photodiodes

7.1 OVERVIEW

This chapter covers design and implementation of position sensitive avalanche photodiodes. This chapter is based on the following publication: (i) *K.S. Shah et. al., Position Sensitive Avalanche Photodiodes for Gamma-Ray Imaging, IEEE Transactions on Nuclear Science V. 49(4), (2002)*. A partial version of this publication is presented in this chapter.

7.2 INTRODUCTION

Current and next generation experiments in nuclear and elementary particle physics require detectors with high spatial resolution, fast response, and accurate energy information [1-3]. Such detectors are required for spectroscopy and the imaging of optical and high energy photons. Additionally, they are of interest in areas such as medical imaging, diffraction, astronomy, nuclear treaty verification, nondestructive evaluation, geological exploration, and nuclear and high-energy physics research. Traditionally, scintillation crystals coupled to imaging detectors such as position sensitive or multi-anode photomultiplier tubes (PMT) are used for spectroscopy and imaging of high energy photons. However, PMTs have low optical quantum efficiency, are relatively bulky and fragile, and are sensitive to magnetic fields.

In order to overcome these limitations in the traditional imaging detectors, we have investigated imaging detector designs based on deep diffused, high-gain silicon avalanche photodiodes (APDs), which are discussed in this paper. Our new approach involves developing an APD design with inherent imaging capability. Such position sensitive avalanche photodiodes (PSAPDs) are similar to the planar APDs that have been developed at RMD [4], but incorporate a resistive layer on the back-face on which multiple contacts can be fabricated. These devices provide position information based on charge sharing amongst the contacts on the back face of the device. We have investigated a PSAPD design with four corner contacts on the back face of the APD. These devices have shown spatial resolution of about 0.3 mm over a device area of 14 mm x 14 mm. High energy and timing resolution have also been measured with such PSAPDs.

The main advantage of the PSAPDs is that the electronic readout requirements with these devices are minimal. It should be noted that the high gain of our APDs is an important factor in the PSAPD design, because it provides high signal to noise ratio for signals at the corner contacts, even when charge is shared amongst them. This enables accurate estimation of the event location. The PSAPDs can be fabricated using the planar processing method that RMD recently has developed.

7.3 POSITION SENSITIVE AVALANCHE PHOTODIODES

7.3.1 Design and Fabrication

We have been investigating a new approach to produce position sensitive avalanche photodiodes by using the high-gain planar APD technology. This involves the modification in the design of the back contact structure of the APD in order to enable determination of the position of interaction. A variety of anode structures, all of which involve charge sharing, has been explored with other detectors such as microchannel plates and silicon p-i-n detectors to provide position sensitivity [5], [1], [6-8]. For our investigation, we have selected a simple design where four contacts are placed on a resistive layer at corners as shown in Figure 1 and

geometric considerations are used to compute position based on signal collected at each corner contact.

Such a PSAPD was fabricated using the planar process that has been developed at RMD for APD array fabrication [4]. The PSAPD area was 14 mm x 14 mm and the device was packaged on a ceramic substrate. Figure 2 shows a photograph of a packaged PSAPD. The device was initially evaluated by connecting the four back contacts together and its gain, noise, and quantum efficiency were measured. The maximum gain of the device was measured to be ~5000, with operating gain (where the signal to noise ratio is maximized) of about 1000. The noise of the device was measured to be about 130 electrons rms. The quantum efficiency of the device was measured to be $\geq 70\%$ in the 350 to 700 nm region. The gain, noise, and quantum efficiency of the PSAPDs were found to be similar to that of standard planar non-imaging APDs.

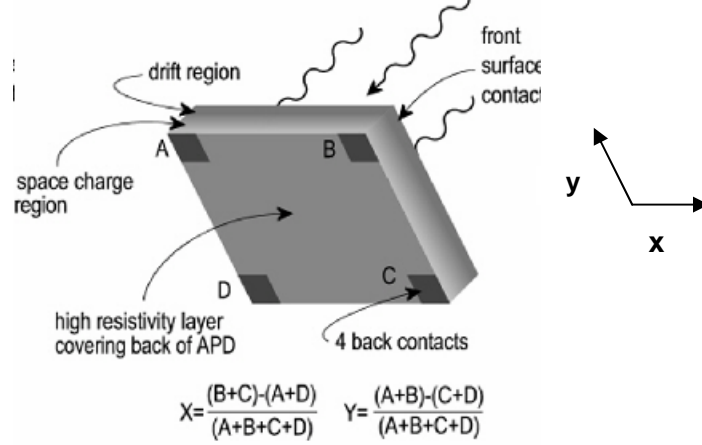


Figure 1. Schematic diagram of a position sensitive avalanche photodiode (PSAPD) with four corner contact design.

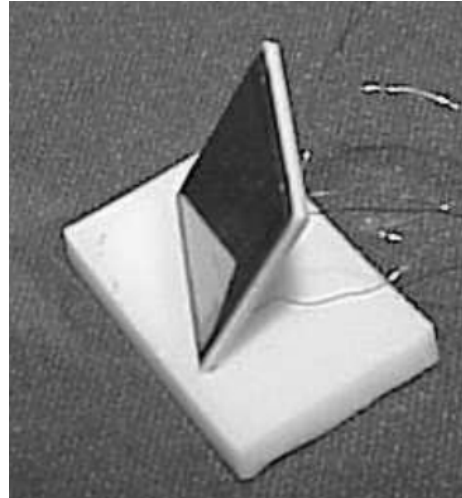


Figure 2. Photograph of PSAPD (with four-corner anode design).

7.3.2 Operational Scheme for Position Sensing and Energy and Timing Resolution of PSAPD

In order to collect accurate energy and position information, the PSAPD was operated as shown in Figure 3. The top contact of the APD acted as the entrance face and was connected to high voltage as well as a preamplifier using AC coupling. In addition, separate preamplifier channels were provided for each of the corner contacts on the back face. In this arrangement, the preamplifier channel connected to the top contact provided the sum of signal from each of the bottom corner contacts and was used to determine energy and timing information for a given interaction [1]. The signals collected from the four bottom contacts were analyzed using the equations summarized in Figure 1 to compute the position of interaction [1]. This operational arrangement is illustrated in the ^{22}Na γ -ray spectra (511 keV photons) collected at all five channels (see Figure 4) upon coupling the PSAPD to a CsI(Tl) scintillator ($1\times1\times1\text{ cm}^3$). The scintillator was placed close to the center of the front face.

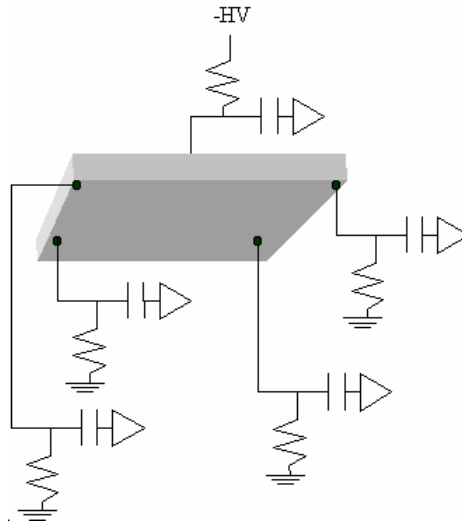


Figure 3. Schematic of the PSAPD test setup to obtain energy and time information from the top contact and position information from the bottom four contacts.

The spectra shown in Figure 4 confirm that the signal from the front face is indeed the sum of the signal collected from all four corner contacts on the back face. Also, as expected, the signal amplitude (as represented by the 511 keV pulse height) is very similar for all four corner contacts because the point of interaction is close to the center of the device. It is important to note that the operational arrangement shown in Figure 3 does not compromise the energy or time information of the APD. This was confirmed by recording a 511 keV spectrum in a similar manner but with all four corner contacts connected to ground, which is the traditional manner of operation for a conventional APD (without position sensing capability). The resulting 511 keV peak was very similar to that shown in Figure 4, confirming that no degradation in energy resolution and peak amplitude occurs upon incorporating the position sensing capability to an APD. The energy resolution for the 511 keV peak recorded by the top channel (representing the sum signal) in both cases was $<10\%$ (FWHM). Direct X-ray detection of 5.9 keV photons (^{55}Fe source) with a PSAPD was also performed with an energy resolution of 1.5 keV (FWHM).

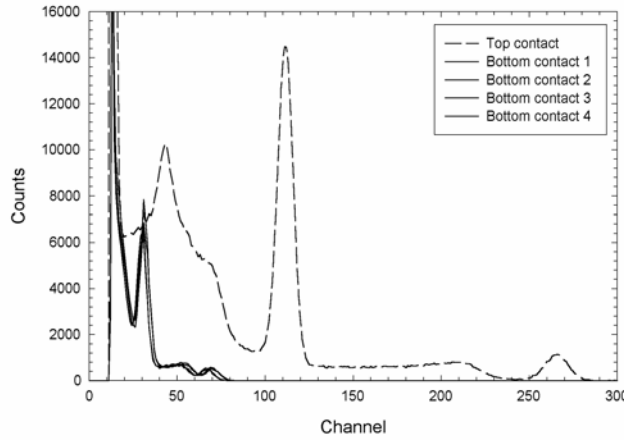


Figure 4. ^{22}Na spectra recorded with each of the five channels of the PSAPD upon coupling a CsI(Tl) scintillator to the PSAPD near the center of the device.

The timing properties of the PSAPDs have been measured. The risetime of a PSAPD was measured by irradiating its top surface with 5.5 MeV α -particles and recording the resulting signal from the top contact directly (without amplification) on a digital oscilloscope. The risetime was found to be ~ 1 ns, confirming the fast operation of the PSAPD. Coincidence timing resolution with a PMT coupled to one LSO crystal as the start channel and a PSAPD coupled to another LSO crystal as the stop channel has been measured to be 4 ns (FWHM), as shown in Figure 5. The PMT-LSO contribution is < 1 ns (FWHM).

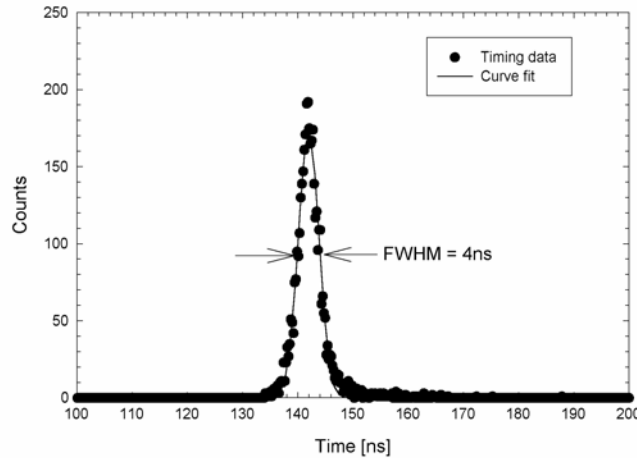


Figure 5. Timing resolution of the PSAPD in coincidence with a PMT (both coupled to LSO), with FWHM of 4ns.

7.3.3 Position Sensing Capabilities

The position sensing capability of the PSAPD has been characterized. In this experiment, an optical fiber with 1 mm diameter was placed at different locations on the PSAPD to create 7 x 8 rectangular pattern (1.85 mm spacing between adjacent points in both x and y directions). The other end of the optical fiber was coupled to a blue LED (controlled with a pulser). The optical pulse reaching the PSAPD face was about 10,000 photons which is comparable to light emission

from an LSO crystal upon interaction with 511 keV photons. The signal collected from each corner contact was fed to a shaping amplifier, and then sent to a multi-channel analyzer to produce a pulse height spectrum. The peak position was recorded for each contact (for a given fiber position) and this information was used to compute the event location. Figure 6 shows the resulting 7 x 8 array plot depicting the event location estimated with PSAPD for each position of the fiber on the PSAPD. Some pincushion type distortion is observed in the plot shown in Figure 6, which is expected for the simple four corner contact geometry. Such distortions can be corrected in most cases using a previously measured response map for the PSAPD. For imaging with segmented scintillators, these distortions have limited impact as long as the crystal of interaction can be located unambiguously. Despite the pincushion distortion, Figure 6 confirms the position sensing capability of the PSAPD, and indicates that the position resolution of the device is much less than 2 mm since the data points can be readily distinguished in the figure.

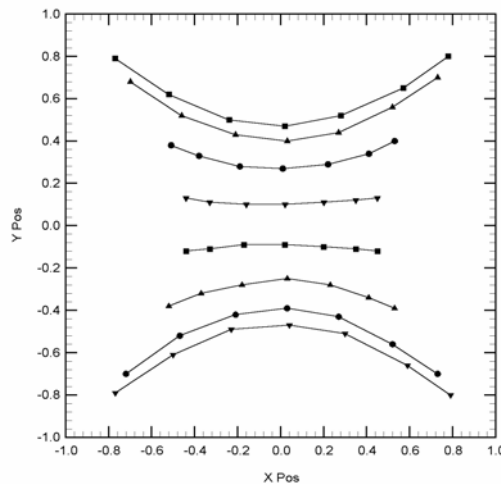


Figure 6. Estimated optical fiber position map with the PSAPD for fiber placement in a rectangular 7 x 8 pattern on the PSAPD. The spacing between the adjacent fiber positions was 1.85 mm in both directions.

An experiment was then conducted to acquire a flood histogram for a 4 x 4 array of segmented CsI(Tl) crystals placed on a PSAPD. The pixel size of the CsI(Tl) array was 2 mm x 2 mm x 5mm and a ^{137}Cs (662 keV γ -rays) source was used. The resulting flood histogram, which is shown in Figure 7, clearly demonstrates that the PSAPD can provide unambiguous identification of crystal of interaction. A line profile through one of the rows in the flood histogram is also shown in Figure 7, and the average peak to valley ratio is ~ 20 . We are in process of instituting an algorithm to correct for the distortions in the flood histogram using a previously generated response map, and a corrected histogram for the 4 x 4 CsI(Tl) array is also shown in Figure 7.

Next, we conducted experiments to determine the spatial resolution capability of the PSAPD. In this experiment, a 635nm laser was focused onto the PSAPD with a spot size of approximately 25 μm and with an optical intensity of about 10,000 photons/pulse. The laser was pulsed at a high frequency and the output voltages of the four bottom contacts were recorded directly out of the preamplifiers by a digital oscilloscope. This was repeated until 100 measurements were taken at the same laser position on the PSAPD. The x- and y-positions were

calculated and plotted and the FWHM of the event histogram provided the position resolution of the PSAPD at the location of laser exposure. These measurements were performed at two laser positions on the PSAPD: near the center of the device and near one of its corners. The results are shown in Figure 8 for one co-ordinate. The FWHM was $\sim 240 \mu\text{m}$ and $\sim 280 \mu\text{m}$ at center and corner, respectively. This shows that the position resolution of our PSAPD is excellent over the $14 \text{ mm} \times 14 \text{ mm}$ active area. Position resolution was found to be comparable for the y co-ordinate in our measurements.

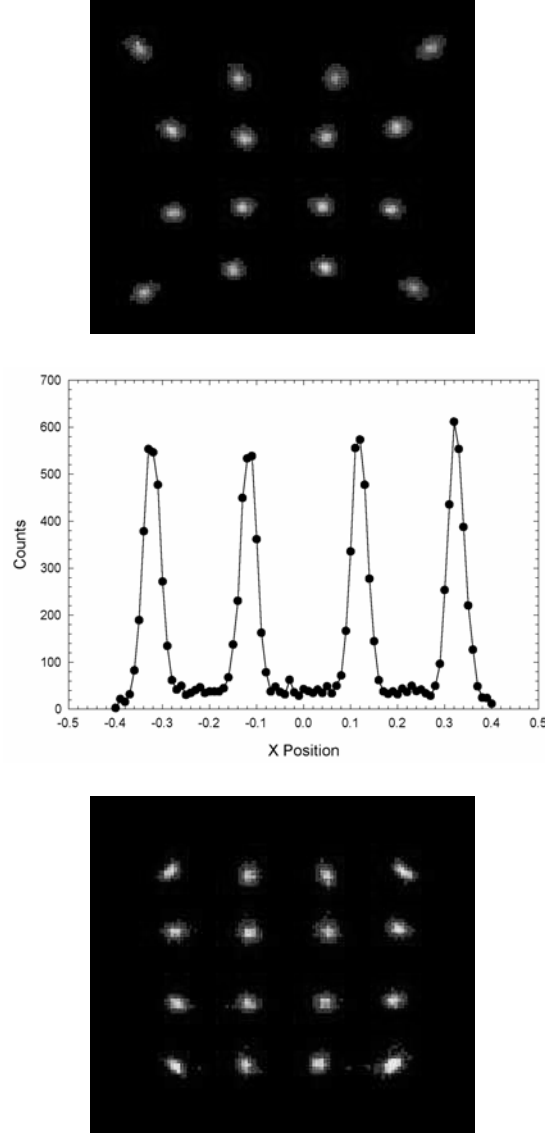


Figure 7. Flood field image of a 4×4 CsI(Tl) array (2 mm pitch) mounted on a PSAPD using 662 keV γ -rays (top), a line profile through one row of the histogram (middle), and a histogram corrected to minimize distortions (bottom).

These results indicate that PSAPDs are indeed promising for gamma ray imaging. These devices have high quantum efficiency, low noise, and high gain. They have demonstrated high energy, timing, and position resolution. An important aspect of the PSAPDs is the reduction in

the electronic readout requirements. As discussed earlier, for a 14 mm x 14 mm device, only five readout channels were required and a spatial resolution < 1 mm (FWHM) was observed. For a multi-element array with discrete pixels and individual readout per pixel, the electronic readout channels are significantly larger. For example, in the case of an array with 14 mm x 14 mm area and 1 mm pixels, the number of readout channels would be 196. Thus, PSAPDs would provide a multiplexing factor of almost 40 in the electronic channels.

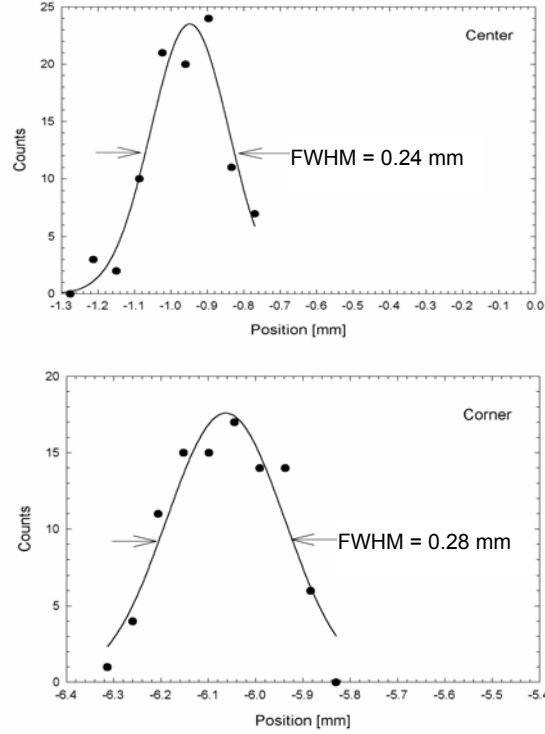


Figure 8. Position resolution of PSAPD near center and corner of the device for x-direction. FWHM of the histograms is ~ 240 μm and ~ 280 μm at center and corner, respectively. Based on device symmetry, spatial resolution is similar for y-direction.

7.3.4 Simulation Studies

We have conducted modeling studies to understand, predict, and minimize the distortions observed in PSAPDs. The distortions (see Figure 6) arise due to majority carrier transport effects within the resistive layer on which the anodes have been constructed. We have used circuit simulation techniques to understand the majority carrier transport using SPICE (Simulation Program with Integrated Circuit Emphasis) for the PSAPDs. Figure 9 shows a unit circuit cell that was used to perform a SPICE simulation of the majority carrier transport for a PSAPD with four corner contact design.

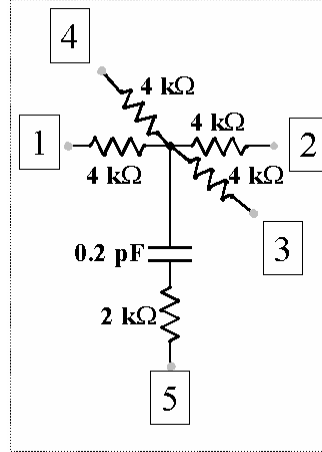


Figure 9. Unit cell for a SPICE simulation of a PSAPD with four corner contacts.

A square array of 22 x 22 unit cells was simulated to be connected together with rows being connected by contacts 1 and 2 and columns being connected by contacts 3 and 4 and each of the four outermost contacts in such chains was connected to a load resistance. Contact 5 was connected to a common ground plane. The imaging performance of such a device was simulated by assuming that photocurrent was injected from a point source into one of the unit cells. By varying the position of the point source over the device in a square 8 x 8 pattern (1.9 mm spacing between adjacent points in both directions for 14x14 mm² PSAPD), the imaging performance of the PSAPD was simulated and the result is shown in Figure 10. This simulation result is in reasonably good agreement with the experimental results shown in Figure 6 and both cases show pincushion type distortion with the data points in the middle of each row or column pushed towards the center.

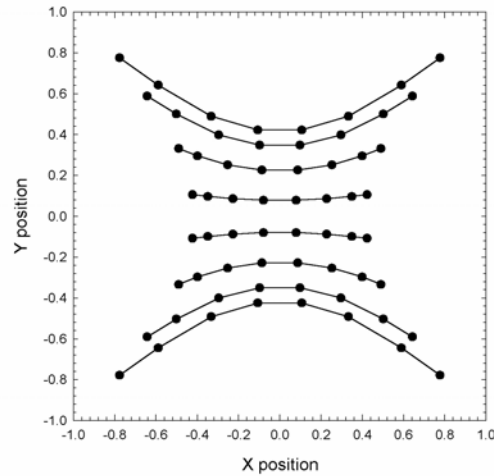


Figure 10. Simulation results showing imaging performance of PSAPD with four corner contacts when the charge input test pattern (from a point source) is an 8 x 8 square array (1.85 mm spacing between adjacent points in both directions) covering the entire device area.

It should be noted that while the pincushion type of distortion may be detrimental in some applications, it is not a problem for γ -ray imaging using individual or segmented scintillation elements. This is because the spatial resolution of the PSAPD is very good, and even if the

device provides a distorted image of the scintillator segments, as long as the correct crystal of interaction is located, software corrections can be applied using a previously generated calibration map.

7.4 SUMMARY

Position sensitive avalanche photodiodes have been investigated for spectroscopy and the imaging of high-energy photons. A PSAPD design with four corner contacts has been fabricated using a planar process with device area of 14 mm x 14 mm. Such PSAPDs have shown high gain, low noise, and high quantum efficiency, which are characteristic of deep diffused APDs. Good energy, timing and position resolution have been observed with such PSAPDs. Furthermore, the electronic readout requirements for such PSAPDs are minimal. Simulation studies (using SPICE) also have been performed to understand distortions in the imaging response of these devices. In our research, new PSAPD designs with minimal distortions, and large area PSAPDs (~2.5 cm x 2.5 cm) are now being explored. Our investigation has shown that PSAPDs are promising devices for nuclear and high energy physics research, medical imaging, non-destructive evaluation, materials science studies, and geological exploration.

7.5 REFERENCES

- P. Burger, M. Keters, L. Van Buul, and J. Verplancke, "New generation of position sensitive silicon detectors," *presented at the Fall MRS Meeting*, Boston, USA, 1997.
- G. F. Knoll, *Radiation Detection and Measurement*, 2nd ed., New York: John Wiley and Sons, 1989.
- K. Kleinknecht, *Detectors for Particle Radiation*, 2nd ed., Cambridge, U.K.: Cambridge University Press, 1998.
- K. S. Shah, R. Farrell, R. Grazioso, R. Myers, and L. Cirignano, *Large-area APDs and monolithic APD Arrays*, IEEE Transactions on Nuclear Science, vol. 48, p. 2352, (2001).
- M. Lampton and C. W. Carlson, "Low-distortion, resistive anodes for two-dimensional position sensitive MCP systems," *Rev. Sci. Instrum.* vol. 50(9), pp. 1093-1097, Sept. 1979.
- T. Doke et al., "A new two-dimensional position sensitive detector with a good linear response," *Nucl. Instr. Meth. A* 261, pp. 605-609, 1987.
- C. Martin, P. Jelinsky, M. Lampton, R. F. Malina, and H. O. Anger, "Wedge and strip anodes for centroid-finding position sensitive photon and particle detectors," *Rev. Sci. Instrum.* vol. 52(7) pp. 1067-1074, Jul. 1981.
- J. L. Alberi and V. Radeka, "Position sensing by charge division," *IEEE Trans. on Nucl. Sci.*, vol. 23, no. 1, pp. 251-258, 1976.

CHAPTER 8: POSITION SENSITIVE APDs FOR SMALL ANIMAL PET

8.1 OVERVIEW

This chapter covers evaluation of position sensitive avalanche photodiodes (PSAPDs) for small animal PET imaging. This chapter is based on the publication: *K.S. Shah et. al., Position Sensitive APDs for Small Animal PET Imaging, IEEE Transactions on Nuclear Science V. 51(1), (2004)*. Complete version of this publication is presented in this chapter.

8.2 INTRODUCTION

Positron Emission Tomography (PET) is an in vivo analog of autoradiography and has the potential to become a powerful new tool in imaging biological processes in small laboratory animals. With the ever increasing number of human disease models (including cancer) in the smaller animals such as mice and rats, high resolution PET imaging of small animals can contribute unique information. The critical advantage of PET is that it allows functional information to be obtained non-invasively, so each animal can be studied repeatedly.

While the attractions of small animal imaging with PET are obvious, the challenges are also very significant. A new generation of very high resolution, high sensitivity and inexpensive PET scanners need to be developed for these demanding, but exciting applications. The main barriers to using PET in studies of laboratory animals have traditionally been poor spatial resolution, cost and accessibility. A number of groups have recently started to challenge these barriers [1]-[6] with the result that small dedicated animal PET scanners with improved resolution and lower cost than clinical PET scanners are now available. Most contemporary designs have opted for the use of very small scintillator elements, read out by position sensitive or multi-channel photomultiplier tubes to achieve high spatial resolution, using high light output scintillators such as lutetium oxyorthosilicate (LSO), or yttrium aluminum pyrovanadate (YAP).

Other readout technologies such as silicon avalanche photodiodes (APDs) are also being considered in small animal PET designs. One of the primary motivations for using APDs is that these silicon-based detectors could ultimately be made very cheaply in high volumes. APDs also offer high optical quantum efficiency (up to a factor of 4 higher than PMTs), wide spectral response, and insensitivity to magnetic fields. Due to these factors, APDs are being actively investigated for small animal PET [3], [7]-[9]. In all such efforts, individual APD pixels are coupled to scintillation crystals to determine the crystal of interaction and provide energy and timing information and there is no multiplexing of signal.

In this paper, an APD design that provides intrinsic position sensing capability and therefore can provide significant reduction in the number of electronic channels that are required is discussed. This is particularly important now, because newer design of high resolution, small animal PET systems have a large number of LSO crystals (10,000 to 20,000), which can have severe impact on the electronic readout requirements for APD-based PET system. The new position sensitive avalanche photodiodes (PSAPD) would simplify the readout requirements in such PET designs and thereby reduce cost as well as complexity of small animal PET systems.

8.3 POSITION SENSITIVE AVALANCHE PHOTODIODES

A new approach of using the high gain planar APD technology to produce position sensitive avalanche photodiodes has been explored. This involves modification in the design of the back contact structure of the APD in order to enable determination of the position of interaction. A variety of anode structures, all of which involve charge sharing, have been explored with other detectors such as microchannel plates and silicon p-i-n detectors to provide position sensitivity [10]-[14]. For our investigation, we have selected a simple design where four contacts are placed on a resistive layer at corners as shown in Fig. 1 and geometric considerations are used to compute position (based on signal collected at each corner contact). In this design, the signal from the top contact is the sum of the signal from the four bottom contacts. The top contact is used to generate energy and timing information for an event while the bottom four contacts provide the position of an event.

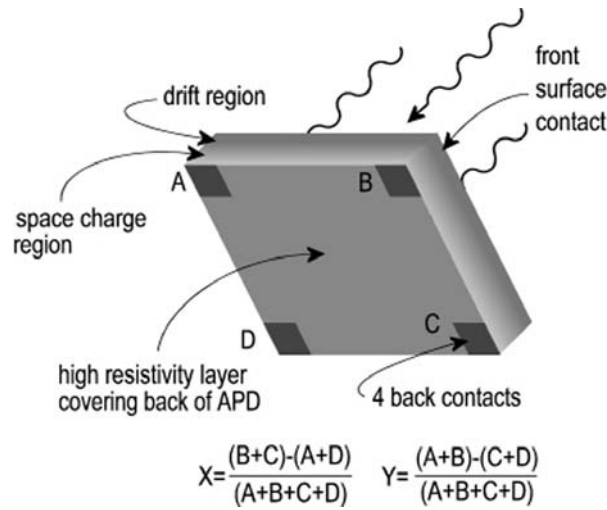


Figure 1. Schematic diagram of a position sensitive avalanche photodiode (PSAPD) with four corner contact design.

Such PSAPDs were fabricated with areas of $8 \times 8 \text{ mm}^2$ and $14 \times 14 \text{ mm}^2$ using the planar process and were packaged on ceramic substrates. We have characterized gain and noise properties of these devices. The operating gain (where the signal to noise ratio is optimized) was ~ 1000 for both PSAPD sizes, while the corresponding noise was 200 and 300 electrons (FWHM) for $8 \times 8 \text{ mm}^2$ and $14 \times 14 \text{ mm}^2$ devices, respectively. The quantum efficiency for these devices was measured to be $\geq 70\%$ in the 350 to 700 nm region. The intrinsic spatial resolution of these devices was measured to be $< 1 \text{ mm}$ (FWHM) and their risetime was $\sim 1 \text{ ns}$ [15]. The imaging response of these devices shows pincushion distortion, which is an intrinsic property of a device with four corner anode design. This distortion can be corrected by processing the image using a previously generated spatial response for the device [15]. For imaging segmented scintillation arrays, this distortion is not critical as long as individual scintillation segments are correctly identified. Thus, PSAPDs are attractive for PET imaging and these devices have been evaluated for PET imaging by coupling them to LSO crystals and arrays.

8.4 EVALUATION OF PSAPD-LSO PET DETECTOR MODULES

PET detectors and modules were constructed by coupling PSAPDs to single LSO crystals and arrays and their energy resolution and timing resolution were measured when irradiated with 511 keV γ -rays. Flood histogram studies were also conducted with PSAPDs coupled to LSO arrays (under illumination with 511 keV γ -rays). Finally, depth of 511 keV γ -ray interaction in LSO crystals was measured by comparing the signal measured with two PSAPDs coupled to opposite faces of the LSO crystals.

For PSAPD evaluation, a five-channel readout system was used. Each channel consisted of a pre-amplification stage (Cremat #101D), a shaping stage (Canberra #2020), and a sample-and-hold stage. The static detector signals were sampled by a 12-bit analog conversion card. Upon a lower-level-discriminator trigger on the 5th input (top contact), the digitizer simultaneously captured and converted all 5 signals from the PSAPD readout sample-and-hold circuitry. Four of the signals (from bottom contacts) were used to generate position and the fifth, the trigger signal, was used for pulse-height and timing analysis. The digitizer was installed in a laboratory computer running Microsoft (MS) Windows 98. MS Visual BASIC and DriverLINX were used to control the I/O card, and to manipulate, display and store the results.

8.4.1 Energy Resolution Measurements

Initially a $14 \times 14 \text{ mm}^2$ PSAPD was coupled to an LSO crystal ($3 \times 4 \times 20 \text{ mm}^3$) and the energy resolution for 511 keV gamma rays was measured. The resulting energy spectrum collected from the top contact of PSAPD is shown in Fig. 2. As seen in the figure, an energy resolution of 12% (FWHM) was recorded at room temperature. Encouraged by this result, we coupled 8×8 element LSO array ($1 \times 1 \times 20 \text{ mm}^3$ pixels) to the $8 \times 8 \text{ mm}^2$ PSAPD and acquired ^{22}Na spectrum (see Fig. 3) at room temperature. The energy resolution of the 511 keV photopeak was 19% (FWHM) at 20°C . Overall, these results are promising and indicate that high energy resolution is achievable with LSO crystals coupled to PSAPDs including LSO samples

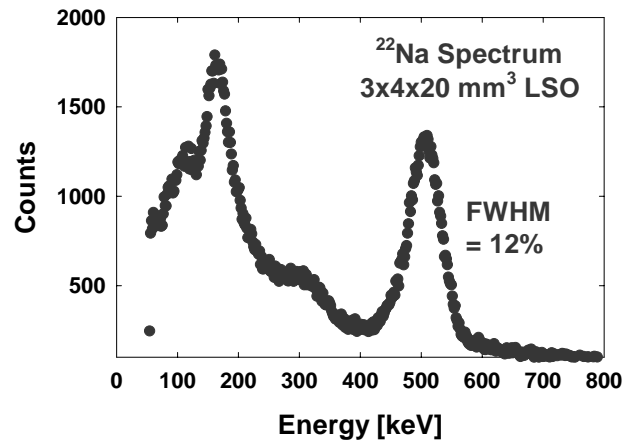


Figure 2. 511 keV γ -ray energy spectrum recorded at 20°C with LSO crystal ($3 \times 4 \times 20 \text{ mm}^3$) coupled to $14 \times 14 \text{ mm}^2$ PSAPD.

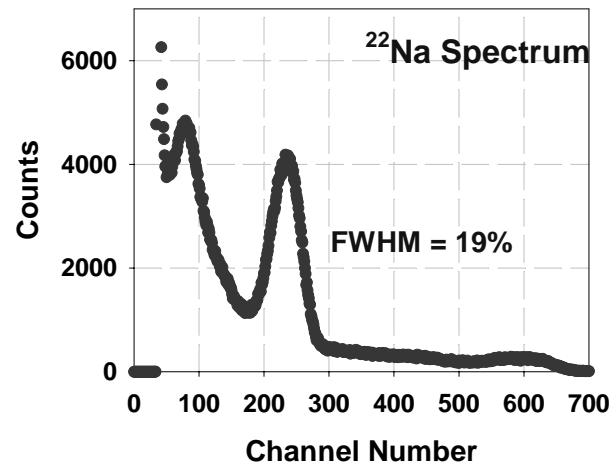


Figure 3. ^{22}Na spectrum collected with 8×8 element LSO array ($1 \times 1 \times 20 \text{ mm}^3$ pixels) mated to $8 \times 8 \text{ mm}^2$ PSAPD at 20°C .

having 1 mm² cross-section. The difference in the energy resolution in Fig. 2 and 3 is probably due to differences in the quality and the aspect ratio of the LSO crystals. Similar energy resolution results were obtained with the 14 x 14 mm² PSAPDs coupled to 1 x 1 x 20 mm³ LSO.

8.4.2 Timing Resolution Studies

Coincidence timing resolution studies have also been performed with the PSAPDs coupled to LSO samples. Two 8 x 8 mm² PSAPDs, each coupled to 1 x 1 x 20 mm³ LSO samples were operating in a coincidence timing circuit. Signal from each channel was processed with a timing filter amplifier (TFA), constant fraction discriminator (CFD) and gate/delay generator and then fed to a time-to-amplitude converter (TAC). These detectors were irradiated with 511 keV positron annihilation γ -ray pairs and a coincidence-timing spectrum, with resolution of 3.2 ns (FWHM) acquired at 20° C is shown in Fig. 4.

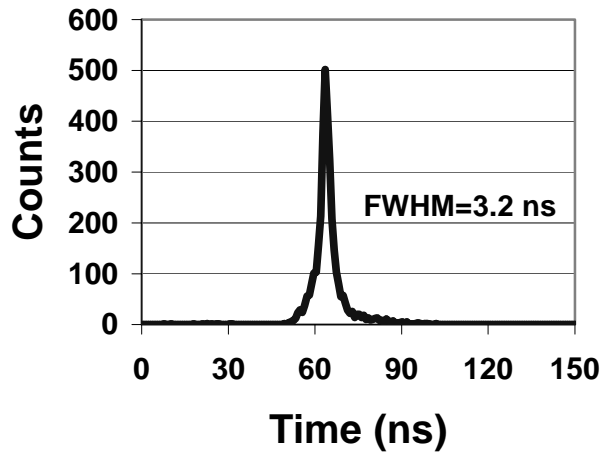


Figure 4. Timing resolution with two 8 x 8 mm² PSAPDs (each coupled to 1 x 1 x 20 mm³ LSO) operating in coincidence at 20° C.

8.4.3 Flood Histogram Studies

Imaging studies have been conducted by coupling 8 x 8 mm² PSAPD to segmented LSO arrays with 1 mm pixels that were 20 mm thick. The LSO array had 8 x 8 element format. The pixel pitch of the LSO array was ~1.2 mm and as a result, the PSAPD covered 6 x 6 elements of the LSO array. 511 keV gamma rays (²²Na source) irradiated the LSO array and the resulting flood histogram, acquired at room temperature is shown in Fig. 5 in a three-dimensional representation. As seen in the figure, all pixels of the 6 x 6 LSO array are well identified and the average peak to valley ratio for the imaging data is ~6. Pincushion distortion can be seen in the histogram, which is an inherent property of the device with four-corner anode design. Such distortion can be readily corrected using previous calibration map of the device.

Overall, these γ -ray imaging studies confirmed that PSAPDs are capable of providing very high spatial resolution. This result, in combination with their high-energy resolution and excellent timing resolution, makes PSAPDs very attractive for high resolution PET applications such as small animal imaging.

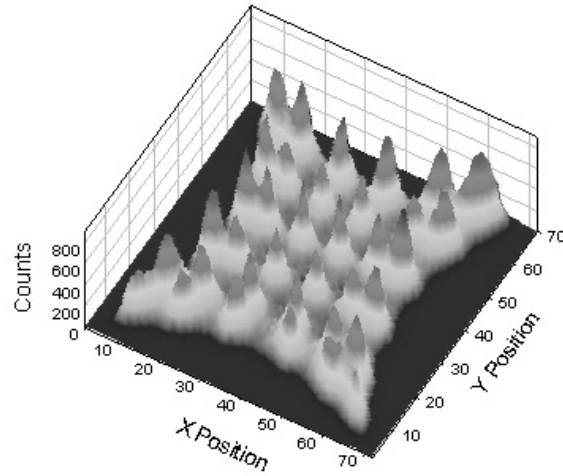


Figure 5. Three dimensional plot of the flood histogram data collected upon coupling a 8×8 mm² PSAPD to an LSO array (1 mm pixels, 20 mm tall) at 20° C. ²²Na source (511 keV gamma rays) was used.

8.4.4 Depth of Interaction Measurements

It is challenging to design high efficiency gamma ray detectors for use in small diameter, very high resolution positron emission tomography (PET) systems for small animal imaging. To fulfill the requirements of high efficiency and high resolution simultaneously suggests the need for long and very narrow scintillation crystals. Such long crystals in a small diameter gantry lead to significant depth of interaction (DOI) or parallax errors, resulting in progressive worsening of image resolution as the imaging location is moved away from the center of the scanner.

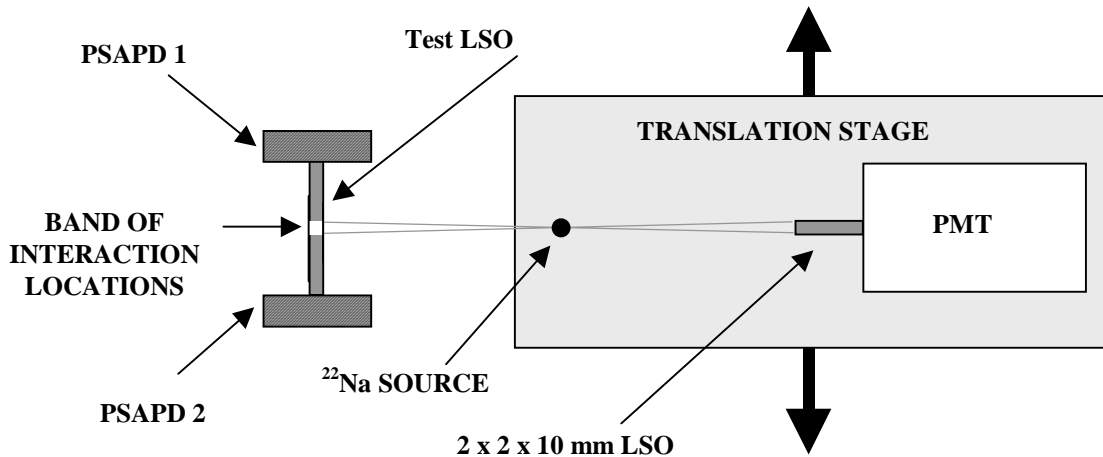


Figure 6. Schematic representation of the experimental setup used to collect DOI data with two PSAPDs.

One approach to estimate the depth of interaction involves collecting optical signal from both ends of the LSO crystals and comparing their relative magnitude [16]. This can be

accomplished by placing two PSAPDs on opposite ends of the LSO crystal. The thin cross-section of PSAPDs ensures that there is minimal attenuation of the incoming gamma-ray flux. The ratio of the PSAPD signals can be used to determine DOI, where the high gain and high signal-to-noise characteristics of these PSAPDs are very important. Fig. 6 shows a schematic representation of the experimental setup that was used to perform DOI measurements.

A special holder was used to perform these measurements which required very careful alignment of the detectors and the source. Both ends of the test LSO crystal ($1 \times 1 \times 20 \text{ mm}^3$) were coupled to PSAPDs which were read out by charge sensitive pre-amplifiers (Cremat #101D). A second LSO crystal ($2 \times 2 \times 10 \text{ mm}^3$) was coupled to a 1.5" diameter single channel PMT for electronically collimating the interactions at different DOI positions. This second detector was mounted on a translation table for 3D positioning with respect to the test LSO crystal that was coupled between the PSAPDs. A ^{22}Na point source (1 mm diameter), which was located inside a source holder attached to the translation table, was placed between the two crystals, 35 mm from each crystal. The holder ensured reproducible positioning of the detectors and source for test crystals. By moving the translation table, interactions at different DOI locations in the test LSO crystal were selected by acquiring coincidence events between the two LSO crystals. The energy thresholds were set just above the noise level. The data acquisition trigger was generated from coincidences between the PSAPD signals and the PMT signal. During the measurement, all electronics settings, including amplifier gains, were kept the same in order to measure the signal change due to scintillation light collection. Data were collected at five DOI locations (2.5 mm, 5 mm, 10 mm, 12.5 mm and 16 mm) on the test LSO crystal at 20° C. These DOI locations represent distances from PSAPD2. Energy spectra were acquired from both PSAPDs (in coincidence with the PMT) for each DOI location. Such energy spectra at three central DOI locations (5 mm, 10 mm, and 16 mm) are shown in Fig. 7. The peak 511 keV positions for both PSAPDs at all five DOI locations are plotted in Fig. 8.

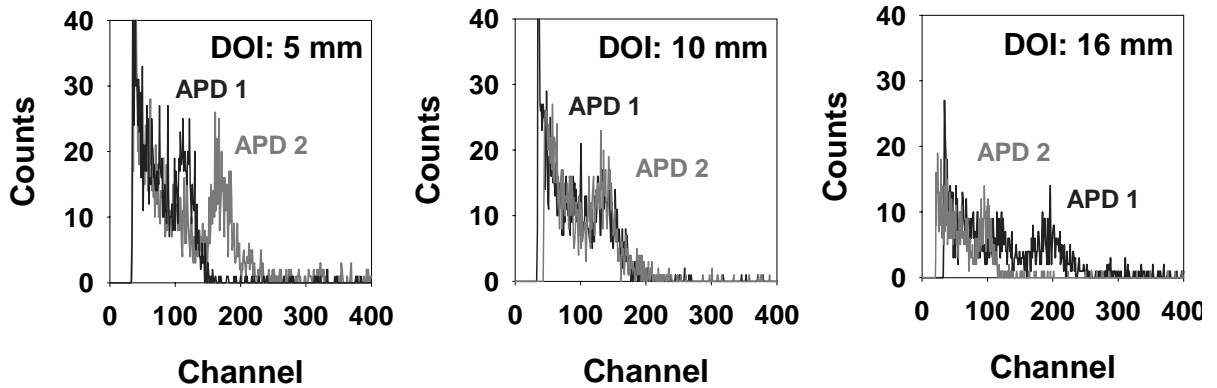


Figure 7. 511 keV energy spectra collected with two PSAPDs coupled to opposite ends of a test LSO crystal ($1 \times 1 \times 20 \text{ mm}$) at room temperature. Gated spectra are collected at different DOI (which represents distance from PSAPD2). For DOI location near center, peak positions for both PSAPDs are similar, while the peak position is higher for both PSAPDs when the DOI location is closer to them, confirming that our approach can provide high DOI resolution.

The trends in the plot clearly indicate that this approach would allow estimation of DOI with good accuracy. Quantification of DOI resolution has been performed using the data shown in Fig. 7 and 8. The DOI location is proportional to the parameter - $\text{APD1}/(\text{APD1}+\text{APD2})$,

where APD1 and APD2 refer to the signals from two PSAPDs. The error in the parameter - $APD1/(APD1+APD2)$ has been estimated using measured 511 keV peak positions and peak broadening for both PSAPDs at all five DOI locations. Gaussian fits to the 511 keV peaks were used to estimate broadening for each spectrum. By performing propagation of error analysis, we estimate the DOI resolution to be < 4.5 mm (FWHM) over the measurement range, which is consistent with the data shown in Fig. 7 and 8.

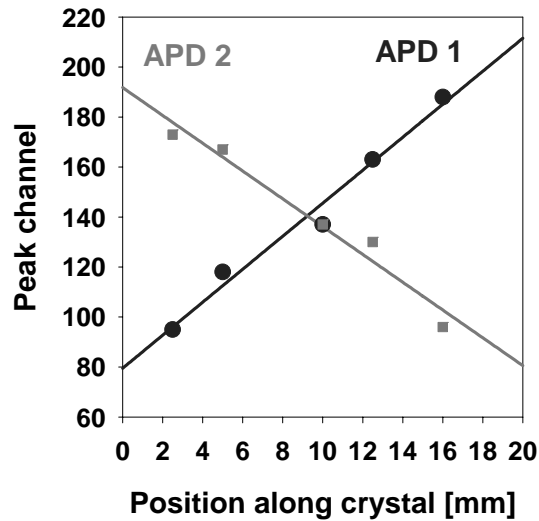


Figure 8. 511 keV peak position with two PSAPDs versus DOI location for 1x1x20 mm LSO crystal. Data are shown for five DOI locations and the solid lines are linear regression fits to the data points.

Overall, these studies indicated that the approach of coupling an avalanche photodiode at either end of a LSO crystal allows accurate estimation of depth of interaction, even for LSO samples with 1 mm cross-section. This in conjunction with high energy, timing, and position resolution obtained with PSAPDs indicates that these devices can be used to build a high resolution, high sensitivity PET system.

8.5 SUMMARY

Position sensitive avalanche photodiodes have been investigated for PET imaging applications. A PSAPD design with four corner contacts has been fabricated using planar process with device area of $8 \times 8 \text{ mm}^2$ and $14 \times 14 \text{ mm}^2$. Such PSAPDs have shown high gain, low noise, and high quantum efficiency, which are characteristic of deep diffused APDs. Good energy, timing, DOI, and position resolution has also been observed with such PSAPDs. Furthermore, the electronic readout requirements for such PSAPDs is minimal. In addition to PET and other nuclear medicine imaging applications, PSAPDs are also promising for nuclear and high energy physics research, non-destructive evaluation, materials science studies, and geological exploration.

8.6 CURRENT STATUS: EXAMPLES OF SMALL ANIMAL PET SCANNERS BUILT WITH PSAPDs

In last few years, PSAPDs with the four corner anode design have generated considerable interest in the field of small volume PET imaging and several high resolution, small animal PET

scanners are being built now with the PSAPD technology [17-22]. Dr. Simon Cherry's team at the University of California, Davis (UC-Davis) is actively collaborating with RMD on implementation of PSAPD technology for small animal PET imaging. In this section, a synopsis of two small animal PET scanners built at UC-Davis using PSAPD technology is provided.

8.6.1 MRI Compatible PET Scanner

UC-Davis team in collaboration with RMD has developed an MRI compatible PET insert that can be placed inside a high-field MRI system to permit simultaneous PET and MR imaging [22]. The system is based on RMD's PSAPD technology and uses short optical fibers (~ 10 cm long) to couple PSAPDs to LSO crystals. Each detector module (**Figure 9a**) consists of an 8×8 array of LSO crystals each measuring $1.43 \times 1.43 \times 6 \text{ mm}^3$, arranged with a pitch of 1.51 mm that are coupled via a 6×6 element double clad optical fiber bundle to a $14 \times 14 \text{ mm}^2$ PSAPD. Charge-sensitive preamplifiers (CR-110, Cremat, Inc.), mounted on printed circuit boards populated with non-magnetic components, are used to readout the PSAPDs. The PET scanner insert (see **Figure 9b**) consists of 16 of these modules arranged in a 12 cm diameter ring. Approximately 5 meter long non-magnetic subminiature coaxial cables (SM 50, Axon' Cable, Inc.) connected the outputs of the amplifiers to standard NIM electronics are used to process the data. A multiplexer was developed to reduce the number of channels from 64 to 8. Two PowerDAQ-II PD2-MFS-C-UT (United Electric Industries, USA) data acquisition boards digitize these channels. Software previously developed for these boards [23] is used for data acquisition. Example simultaneous PET/MRI images acquired with this system are shown in **Figure 9c**. To date, ~ 40 phantom and ~ 50 animal studies have been performed with this system.

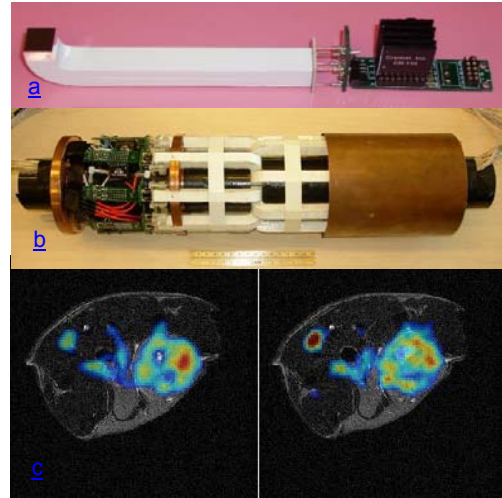


Figure 9: a) PS-APD detector module and b) complete MRI-compatible PET scanner insert. c) Simultaneous PET and MRI images of a mouse showing FDG accumulation in a tumor. Two transverse slices are shown.

8.6.2 Small Animal PET System with Depth-Encoding Detectors

UC Davis team in a collaboration with RMD has also built a small prototype PET system using the dual-ended readout scheme shown in **Figure 6** which utilized PSAPDs as optical detectors (see **Figure 10**). After detailed optimization and characterization at the single crystal and then single detector module level [19, 17], two planar detector panels each consisting of four detector modules have been built (**Figure 10a**). The scanner consists of two detector plates, each with

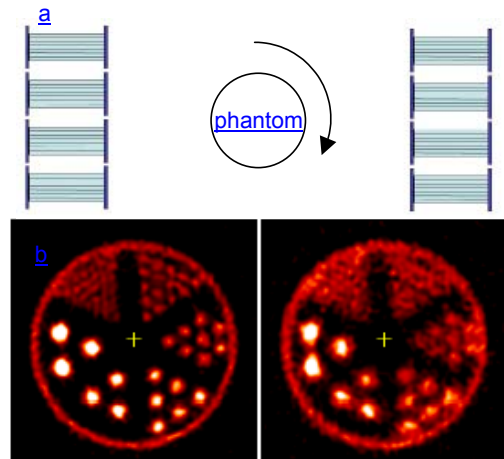


Figure 10: a) Geometry of prototype system with dual-ended readout of LSO arrays with PS-APDs. b) Reconstructed images of Derenzo phantom from system showing results using DOI information (left) and without DOI information (right).

4 detector modules. In each module, there are 7 x 7 LSO arrays, with a crystal size of 0.9 x 0.9 x 20 mm and a pitch of 1.0 mm. The arrays are read out by two 8 x 8 mm² PSAPDs placed at opposite ends of each array. This simple system allows tomographic imaging and study of the depth-of-interaction capabilities by rotating a phantom between the detectors. **Figure 10b** shows images of a Derenzo phantom (with rod diameters of 0.75, 1.0, 1.35, 1.70, 2.0 and 2.4 mm) with and without the DOI encoding provided by the dual ended readout, demonstrating significant resolution improvements from the DOI resolution (which is ~3 mm in these detectors). With DOI encoding, 1 mm diameter rods are well-resolved, which is not the case when DOI encoding is not used.

More recently, UC-Davis team has successfully implemented PET modules that use LSO arrays that have sub-mm elements (0.5x0.5x20 mm³) with dual ended readout using RMD's 8x8 mm² and 14x14 mm² PSAPDs [20], opening up pathways for ultra-high resolution small animal imaging.

One issue with the PSAPDs is the temporal delay in the signal associated to the RC effects in the back layer on which the corner anodes are constructed. This delay is position dependent and the interactions closer to the anodes have smaller delay than those farther away. For example, in the DOI encoding PET modules used to construct the bench-top PET scanner shown in **Figure 10**, a time delay of up to 12.5 ns has been measured between the events generated in a corner scintillation element and one in the center [18]. One consequence of such position dependent delay is that if the summed signal from the whole module is used to create timing signal, the timing resolution degrades. For example, taking the case of the modules used in **Figure 10**, the average timing resolution for individual crystals is about 5.5 ns (FWHM), while that for the entire array degrades to about 9 ns (FWHM). It should be noted that this is not a fatal drawback and most PET scanner electronics used now have the capability to perform crystal-by-crystal time alignment. This approach has been used to correct the observed position dependent timing shift for PSAPD based PET modules [24].

8.7 REFERENCES

- [1] Cherry SR, et al.. MicroPET: a high resolution PET scanner for imaging small animals. IEEE Trans Nucl Sci 44: 1161-1166 (1997)
- [2] Del Guerra A, de Notaristefani F, Di Domenico G, Giganti M, Pani R, Piffanelli A, Turra A, Zavattini G. Use of a YAP:Ce Matrix Coupled to a Position-Sensitive Photomultiplier for High Resolution Positron Emission Tomography. IEEE Transactions on Nuclear Science, 43: 1958-1962 (1996).
- [3] Lecomte R., et al. P. Initial results from the Sherbrooke Avalanche Photodiode Positron Tomograph. IEEE Trans. Nucl. Sci. 43: 1952-1957 (1996)
- [4] C. J. Marriott, J. E. Cadorette, R. Lecomte, V. Scasnar, J. Rousseau, and J. E. van Lier, "High-resolution PET imaging and quantitation of pharmaceutical biodistributions in a small animal using avalanche photodiode detectors," J of Nuclear Medicine, vol. 35, pp. 1390-6, 1994.
- [5] Weber, S., Terstegge, A., Herzog, H., Reinartz, R., Reinhart, P., Rongen, F., Muller-Gartner, H.W. and Halling, H. The design of an animal PET: flexible geometry for achieving optimal spatial resolution or high sensitivity. IEEE Trans Med Imag 16: 684-9 (1997).

- [6] Jeavons AP, Chandler RA, Dettmar CAR. A 3D HIDAC-PET Camera with sub-millimetre resolution for imaging small animals. IEEE Trans on Nuclear Science, 46: 468-73 (1999).
- [7] Shao, Y. et al., Dual APD array Readout of LSO crystals: Optimization of Crystal Surface Treatment, presented at IEEE Nuc. Sci. Symp., Lyon, France, October, (2000).
- [8] S.I. Ziegler, B.J. Pilcher, G. Boening, M. Rafecas, W. Pimpl, E. Lorenz, N. Schmitz, M. Schwaiger, A prototype high-resolution animal positron tomograph with avalanche photodiode arrays and LSO crystals, Eur J Nucl Med, 28: 136-143, (2001)
- [9] Fries, O., Bradbury, S.M., Gebauer, J., Holl, I., Lorenz, E., Renker, D. and Ziegler, S.I. A small animal PET prototype based on LSO crystals read out by avalanche photodiodes. Nucl Inst Meth A387: 220-4 (1997).
- [10] M. Lampton and C.W. Carlson, Low-distortion, resistive anodes for two-dimensional position sensitive MCP systems, Rev. Sci. Instrum. 50(9) Sept. (1979).
- [11] C. Martin, P. Jelinsky, M. Lampton, R.F. Malina, and H.O. Anger, Wedge and strip anodes for centroid-finding position sensitive photon and particle detectors, Rev. Sci. Instrum. 52(7) Jul. (1981).
- [12] T. Doke et al., A New Two-Dimensional Position Sensitive Detector with a good linear response, Nuc. Inst. and Meth. in Phys. Res., A261, p. 605, (1987).
- [13] P. Burger, M. Keters, L. Van Buul, J. Verplancke, New Generation of Position Sensitive Silicon Detectors, Presented at the Fall MRS Meeting, Boston, December (1997).
- [14] J.L. Alberi and V. Radeka, Position Sensing by Charge Division, IEEE Trans. Nuc. Sci. NS-23(1), 1976.
- [15] Shah, K.S., R. Farrell et al., APD Designs for X-ray and Gamma Ray Imaging, presented at IEEE Nuclear Science Symposium, San Diego, CA, Nov. (2001).
- [16] Moses WW, et al. A room temperature LSO/PIN photodiode PET detector module that measures depth of interaction. IEEE Trans Nucl Sci 42: 1085-1089 (1995)
- [17] Y.F. Yang, P.A. Dokhale, et. al., Depth of interaction measurements for a high resolution PET detector using position sensitive avalanche photodiodes, Physics in Medicine and Biology, 51(9), 2131-2142, (2006)
- [18] Y.F. Yang, Y.B. Wu, et. al., A prototype PET scanner with DOI encoding detectors, J Nucl Med, 49, 1132-40, (2008)
- [19] P. Dokhale, R.W. Silverman, K.S. Shah, R. Grazioso, R. Farrell, J. Glodo, M.A. McClish, G. Entine, V.-H. Tran, and S.R. Cherry, *Performance Measurement of a Depth Encoding PET Detector Module Based on Position Sensitive APD Readout*, Presented at IEEE NSS/MIC, Portland, Or, Oct, (2003).
- [20] S. St. James, Y.F. Yang, et. al., Experimental characterization and system simulations of depth of depth of interaction PET detectors using 0.5 mm and 0.7 mm LSO arrays, Phys. Med. & Biol., 54, 4605-4619, (2009).
- [21] J. Zhang, A.M.K. Foudray, P.D. Olcott and C.S. Levin, 2005 IEEE NSS-MIC conference record, 2478-2482.
- [22] C. Catana, S.R. Cherry et. al, *Optical fiber coupled APDs for the readout of LSO crystals in a simultaneous PET-MRI scanner*, Presented at IEEE NSS/MIC Conference, Puerto Rico, Oct., (2005); C. Catana, Y. Wu, M. S. Judenhofer, J. Qi, B. J. Pichler, P. Dokhale, K. S. Shah, R. Farrell, S. R. Cherry, *Initial Performance Tests of a PSAPD-Based MRI Compatible PET Scanner*, Presented at IEEE MIC, San Diego, Oct., (2006).

- [23] M.S. Judenhofer, B.J. Pichler, S.R. Cherry, *Evaluation of high performance data acquisition boards for simultaneous sampling of fast signals from PET detectors*, Phys. Med. Biol. 50 29-44, (2005)
- [24] K. Burr, J. LeBlanc, S. Zelakiewicz, A. Ganin, C.L. Kim, D.L. McDaniel, K.S. Shah, R. Grazioso, R. Farrell, J. Glodo, *Evaluation of Position Sensitive Avalanche Photodiodes for PET*, presented at IEEE NSS/MIC, Norfolk, VA, Nov, (2002).

CHAPTER 9: SOLID-STATE PHOTOMULTIPLIERS AS PHOTODETECTORS FOR PET

9.1. INTRODUCTION

Positron Emission Tomography (PET) is a functional imaging technique with potential to quantify the rates of biological processes *in vivo* [Bushberg]. PET imaging can provide diagnosis for symptoms of diseases such as Alzheimer's disease, head trauma, and stroke [Phelps]. PET technology is also playing a prominent and an increasingly visible role in modern cancer research, clinical diagnosis and oncology [Phelps, Beyer]. While PET is a powerful imaging tool, the performance of current clinical PET systems is limited by the available detector technology and there is an urgent need for improvement in PET instrumentation in order to exploit the full potential of this promising technique. Modern PET camera designs use inorganic scintillator blocks to stop the incoming gamma-rays, coupled to an array of photomultiplier tubes (PMTs) to detect the position of the scintillated light. The overall performance, size, weight, and cost of these clinical PET cameras are strongly influenced by the photomultiplier tubes used. In particular, the relatively low quantum efficiency, high cost, inability to function in high magnetic fields, and bulkiness of PMTs are limiting factors in clinical as well as small animal PET cameras.

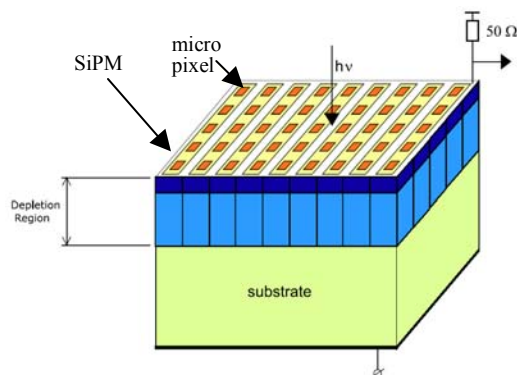


Figure 1. Schematic of a silicon photomultiplier (SiPM).

To overcome the limitations of PMTs in PET imaging, an investigation of an emerging photodetector technology, silicon photomultiplier (SiPM), for PET imaging is discussed in this chapter. SiPM is a solid-state photodetector and its schematic representation is shown in **Figure 1**. A SiPM consists of a large number of micro-pixels (see **Figure 1**) that are joined together on a common silicon substrate and are operated with a common output [Buzhan 03, Dolgoshein 03 & 05, Saveliev]. These micro-pixels are typically 20-30 μm in size and thus, even a 1 mm^2 SiPM consists of a large number of micro-pixels (~ 500 or more) that are electrically isolated from each other.

These micro-pixels are operated in a Geiger mode where the bias voltage is about 10-15% higher than the breakdown voltage. When a photon strikes the micro-pixel biased above the breakdown, it responds with a very high gain ($\sim 10^6$), which is independent of the input photon energy. In this mode each pixel is actually a binary device. An entire array of pixels coupled to a light emitting detector (such as a scintillator) works as an analog device. The light output of the scintillation detector is proportional to the energy of the radiation, so more intense radiation will cause more pixels to trigger. In the solid-state photomultiplier, the total energy is represented by

the number of triggered pixels produced by the scintillation event. The dynamic range of the detector depends on the number of micro-pixels in the SiPM.

The gain of a micro-pixel of the SiPM in Geiger mode is governed by the charge storage capacity of the micro-pixel. This charge storage capacity is essentially the product of micro-pixel capacitance (C_{pixel} with typical value of ~ 100 fF) and the over-bias applied to the device over breakdown ($V_{bias} - V_{breakdown} \approx$ few volts). From these parameters, the stored charge is ~ 200 fC and the corresponding micro-pixel gain is $\sim 10^6$, comparable to that of the PMTs. Due to very high gain of the micro-pixels and their common output, the electronic readout of SiPMs can be simpler compared to other solid-state photodetectors. Furthermore, the operating bias required for these devices is only 25-50 V, which is significantly lower than that for traditional PMTs and APDs. The SiPMs are inherently very fast devices [Buzhan 01, 03 & 06, Dolgoshein 03]. Their depletion width is very thin, typically $< 1 \mu\text{m}$, and the Geiger discharge is a very fast process (< 500 ps). These processes govern the device rise time, which is typically faster than 1 ns. After the Geiger discharge, the device, with passive (resistor-based) quenching, recovers with decay time constant of $R_{quench} \bullet C_{pixel}$ (≈ 30 ns). The combination of such fast response and excellent signal-to-noise ratio for SiPMs indicates that these devices should be capable of excellent timing resolution. Pioneering research on SiPMs has been carried out in Russia and these devices have been fabricated using metal-resistor-semiconductor (MRS) structures [Buzhan 03 & 05, Dolgoshein 03 & 05, Saveliev].

Recently, we have developed a complementary metal-oxide-semiconductor (CMOS) compatible design capable of supporting large arrays of Geiger photodiode (GPD) pixels [Stapels, Shah 07a] for fabricating analogous SiPMs, which we refer to as solid-state photomultipliers (SSPMs). Such CMOS-SiPMs (or SSPMs) retain all major features of the devices fabricated using MRS structures such as high gain and fast response and have comparable optical detection efficiency. CMOS processing also provides an option for monolithic integration of SSPM structures with other readout elements. Our prior investigation of CMOS GPD pixels has shown that these pixels show gain of up to 1,000 in linear mode, in addition to detecting single optical photons when operated in Geiger mode [Stapels]. In Geiger mode, the CMOS GPD pixels produce large pulses (with gain of $\sim 10^6$) for each absorbed optical photon. The dark count rate normalized with respect to the GPD pixel area is ~ 0.3 to 0.7 MHz/mm² at room temperature for operating bias of about 1-2 volts above the breakdown value. Optical quantum efficiency of the GPD pixels is reasonably high over 400 to 550 nm, where many common scintillators emit, though improvement at wavelengths below 400 nm is required. By overlapping the emission spectra of LYSO and BGO with the spectral response of the GPD pixels, we estimate that the overall quantum efficiency of the GPD pixels to be as high as 47% for LYSO and $>50\%$ for BGO. Overall, these CMOS-GPD micro-pixels have shown adequate characteristics for construction of CMOS-SSPMs.

We believe that upon sufficient advancement, these SSPMs will become very attractive photodetectors to read out scintillators in PET applications. They offer very high gain (10^6) and fast response. Very high timing resolution, expected from these devices, would enable excellent rejection of randoms. The high timing resolution of SSPMs could also offer time-of-flight (TOF) capability, which would provide further improvement in the signal-to-noise ratio and image quality. Adequate energy resolution and scatter rejection should be possible with these

devices. Also, because the SSPMs are compact devices, they can be placed on opposite ends of the scintillation crystals (see **Figure 2**) to determine the depth-of-interaction (DOI) of 511 keV γ -rays in the scintillators. Such DOI information would reduce the parallax error in the resulting PET scanners. Silicon based sensors such as SSPMs are also expected to be insensitive to magnetic fields, which creates possibility of combining PET imaging with MRI to allow co-registration of functional images (acquired using PET) with high resolution anatomical images (acquired using MRI). There is an emerging interest in such multi-modality imaging [Grazioso].

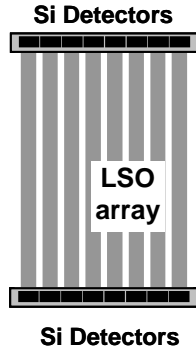


Figure 2. Schematic of a PET module with dual ended read out of scintillators using Si detectors.

Our research, presented in this chapter, has focused on construction and evaluation of large format arrays of GPD micro-pixels with common output to build SSPMs. Evaluation of such SSPMs for PET imaging has been conducted.

9.2. LAYOUT AND FABRICATION OF PROTOTYPE SSPMs

From our prior research, a *p on n-well* CMOS micro-pixel design was selected and the next step was to construct solid-state photomultipliers using a large number of such micro-pixels. Two versions of SSPMs were initially built. The first version was designed to have 100 micro-pixels in 4x25 layout, with each pixel being 20 μm in diameter with 46- μm pitch. The effective area of this SSPM would be $\sim 0.17 \times 1.1 \text{ mm}^2$. **Figure 3** shows the layout of this SSPM.

In addition, a larger SSPM with 3x3 mm^2 area and 785 pixels with 30 μm diameter (in 28x28 pixel format, 100- μm pitch) was also designed and its layout is shown in **Figure 4**. The main consideration with the larger device was to choose a relatively safe design (in terms of inter-pixel spacing) to enable construction of functional devices, again due to limited fabrication runs that can be performed.

Once the layouts of the selected SSPMs were developed, these devices were fabricated using the MOSIS consortium, which is a multi-user service. MOSIS provides prototyping and small-volume production services for VLSI and ASIC circuit development. Mask generation, wafer processing, and device packaging are contracted to leading industry vendors. MOSIS keeps the cost of fabricating prototype quantities low by aggregating multiple designs onto one mask set. This allows customers to share the costs associated with mask making, photolithography, wafer fabrication, and assembly. MOSIS provides access to a wide variety of semiconductor processes offered by many different foundries. A variety of CAD tools and libraries, both foundry-specific and vendor-independent, can be used to prepare designs for

MOSIS. Typically, the production run yielded 15 packaged prototype chips. **Figures 5 & 6** show photographs of prototype SSPMs built by CMOS process [Shah 07a].

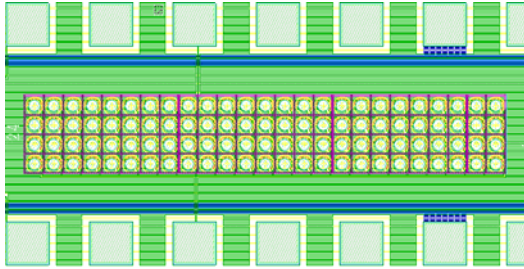


Figure 3. Layout of 4x25 CMOS micro-pixel array with 20-micron diameter pixels at a pitch of 46 microns. The square contact pads around the edges of the chip are 100 microns on a side.

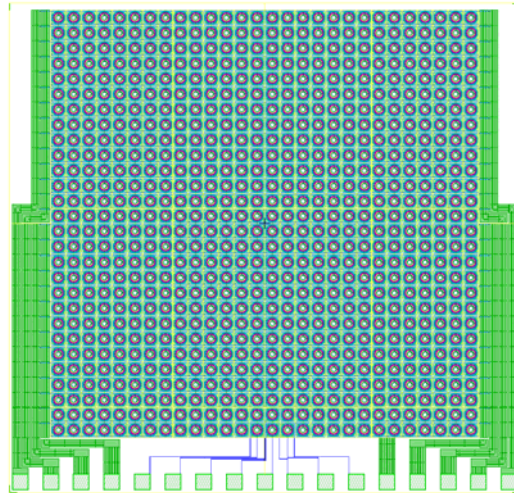


Figure 4. Layout of a 3x3 mm² SSPM with 28x28 Geiger micro-pixels (100 micron pitch).

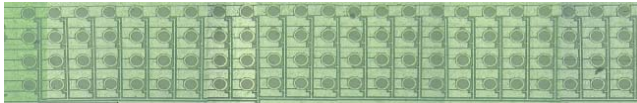


Figure 5 A photograph of a prototype CMOS based, 100 micro-pixel, SSPM with 4x25 micro-pixel format (46 μ m pitch).

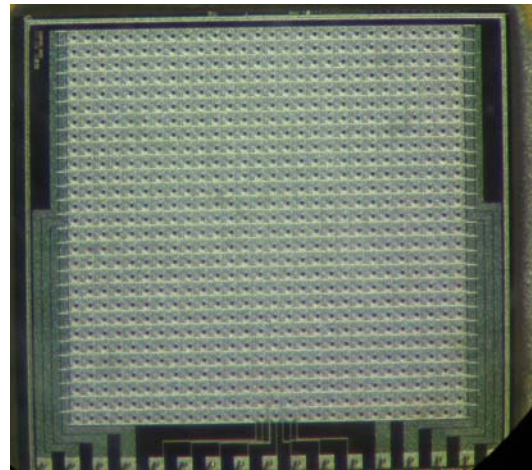


Figure 6. Photograph of 3x3 mm² SSPM with 28x28 Geiger micro-pixels (100 micron pitch).

9.3. BASIC SSPM CHARACTERIZATION

Once prototype CMOS SSPMs were built, their performance was characterized. Initial studies involved measurement of dark count-rate, gain and single photoelectron spectrum. Cross-talk and after-pulsing issues were also explored. Evaluation of SSPMs with 100 micro-pixels (20- μ m diameter micro-pixels with 46- μ m pitch) is discussed first. We have measured the average dark count-rate (DCR) as a function of over-voltage above breakdown. The measurement was performed at 24 °C using the 100-pixel SSPM shown earlier in **Figure 5**. The average DCR was measured by counting the number of pulses with a rate meter during a specified time interval at a given over-voltage above breakdown. As shown in **Figure 7**, the average DCR increases linearly with increased voltage and that the average DCR per pixel is low (< 1 kHz) over the entire voltage range. The normalized dark count-rate at over-bias of 1-2 volts

above breakdown is below 1 MHz/mm^2 , which matches the results measured for single CMOS-GPD micro-pixel.

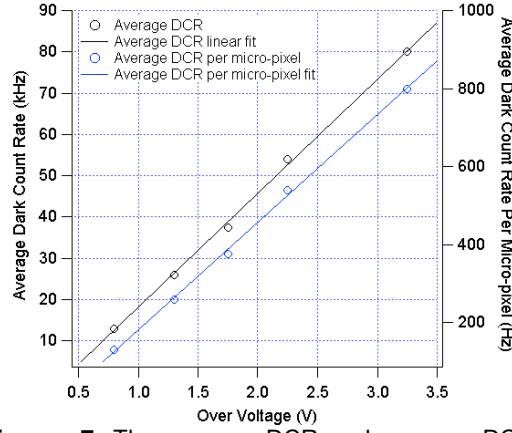


Figure 7. The average DCR and average DCR per micro-pixel versus over-voltage for the prototype 100 pixel CMOS SSPM.

Next, we illuminated SSPM with 100 micro-pixels with a low light intensity 632-nm LED at room temperature and recorded the resulting pulse height distribution (see **Figure 8**). The SSPM was operated at over-bias of 1.3 V above breakdown. No preamplifier was used in this study and the output of the SSPM was shaped using a spectroscopy amplifier (Canberra #2020). The amplifier signal was fed to a multichannel analyzer (Amptek 8000A) connected to a personal computer. The peaks corresponding to single and multiple photoelectrons are clearly resolved in the pulse height spectrum with a mean photoelectron value of ~ 9 . The high photoelectron resolution is indicative of a low excess noise factor, good micro-pixel gain uniformity, and very low electronic noise.

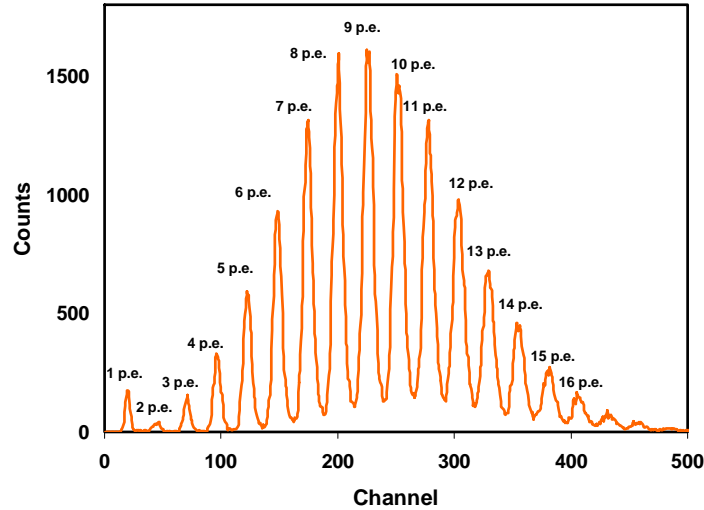


Figure 8. Pulse height spectrum recorded with a CMOS-SSPM (with 100 micro-pixels) upon irradiation with a low intensity pulsed LED (635 nm) at room temperature. Detection of single and multiple photoelectrons is clearly visible.

We also measured the gain of the SSPM operating near breakdown ($\sim 27 \text{ V}$) by comparing the amplitude for the single photoelectron peak with that for a calibrated charge input. Next, by

tracking the position of the single electron peak in the pulse height spectrum as a function of applied bias we measured gain versus bias relationship for the SSPM. The resulting gain versus bias plot for the SSPM is shown in **Figure 9**. As seen in the figure, gain values greater than 10^5 are readily achieved with the SSPMs upon applying bias that is few volts (1-3 V) above breakdown value of ~ 27 V. The operating bias applied to the device is between 27 and 30 V. The relationship between the gain of the micro-pixel (G_{pixel}) and the amount of over-voltage (ΔV) can be expressed as follows:

$$G_{pixel} = \frac{Q_{pixel}}{e} = \frac{C_{pixel}}{e} \Delta V$$

where e is the electron charge, ΔV is the over-voltage, and G_{pixel} , Q_{pixel} , and C_{pixel} are the single micro-pixel gain, charge, and capacitance respectively. Since G_{pixel} increases linearly with voltage above breakdown, the slope of a linear fit to the data shown in **Figure 9** can be used to calculate C_{pixel} . Using such an analysis, we estimate C_{pixel} to be ~ 26 fF, which agrees reasonably well the theoretical value calculated using micro-pixel dimensions.

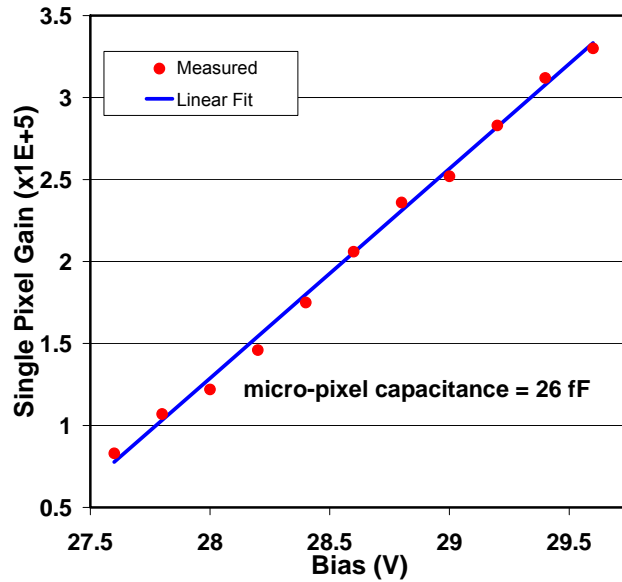


Figure 9. Single micro-pixel gain versus bias for a 100 element SSPM (20- μ m diameter for micro-pixels, 46- μ m pitch). From the slope, the micro-pixel capacitance (C_{pixel}) is estimated to be 26 fF.

SSPMs are expected to be fast devices due to the very thin width of their depletion layer and the very short time for a Geiger discharge (~ 500 ps). In addition, the Geiger discharge for a given micro-pixel is quickly quenched in a time span determined by the micro-pixel's capacitance and quenching resistance ($R_{quench} \bullet C_{pixel}$). **Figure 10** is a digital oscilloscope screen capture of the SSPM output without a light source present. The response, due to dark counts, shows very fast risetime (< 1 ns) and rapid recovery time of ≤ 10 ns.

We have also investigated optical cross-talk in the new CMOS SSPMs. The optical cross-talk in the silicon photomultipliers is due to the light emitted by a micro-pixel undergoing Geiger discharge ($\sim 10^{-5}$ photons/electron) [Dolgoshein 03]. These photons can be detected by other micro-pixels causing cross-talk. In some of our recent SSPMs, the micro-pixels have active

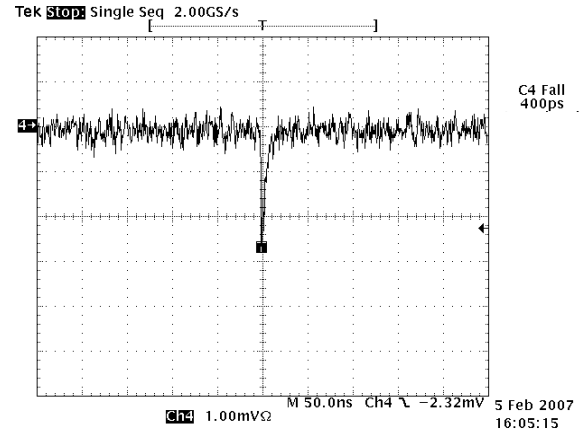


Figure 10. An oscilloscope screen capture of the SSPM output (with 100 micro-pixels) showing the pulse waveform due to dark counts. Fast risetime (~ 400 ps) and rapid recovery time (≤ 10 ns) are observed.

diameter of 20 μm with a pitch of 46 μm . We have evaluated cross-talk in these devices and the results are very encouraging. The cross talk gain (or XTG), which represents the average number of pixels that actually fire for a single initiating event, is plotted in **Figure 11** as a function of excess bias (over breakdown value) for a pixel pitch of 46 μm . At a reasonable operating bias of up to 2 volts above breakdown (where the micro-pixel gain, G_{pixel} , is $>10^5$), the cross-talk is $\leq 6\%$, which is encouraging.

Finally, after-pulsing effects in these CMOS micro-pixels has also been studied. The after-pulsing effect arises due to delayed release of the electrons that are trapped during Geiger discharge [Dolgoshein 05]. Visual inspection of the oscilloscope trace for micro-pixel signal from the two prototype SSPMs show very little after-pulsing. In a more quantitative study for the 100-pixel SSPM (20 μm pixels with a pitch of 46 μm), each Geiger event for a passively quenched pixel was gated and the gate width was adjusted from 0.2 to 30 μs to examine after-pulsing. The results indicated that the contribution of after-pulsing effect was less than 5% over several hundred microseconds. Furthermore, because these after-pulses are not time correlated from pixel to pixel, these events are generally below the threshold set to eliminate dark counts. As a result, the contribution of after-pulsing, when these SSPMs are coupled to scintillators for gamma-ray spectroscopy, is expected to be minimal.

Similar studies of dark count-rate, gain and cross-talk were also conducted for the larger 3x3 mm^2 SSPMs with 785 micro-pixels (30 μm diameter). The normalized dark count-rate was measured to be $<1 \text{ MHz/mm}^2$, which is similar to the normalized value recorded for individual micro-pixels (with 30- μm diameter) operating in Geiger mode. Gain measurements for the

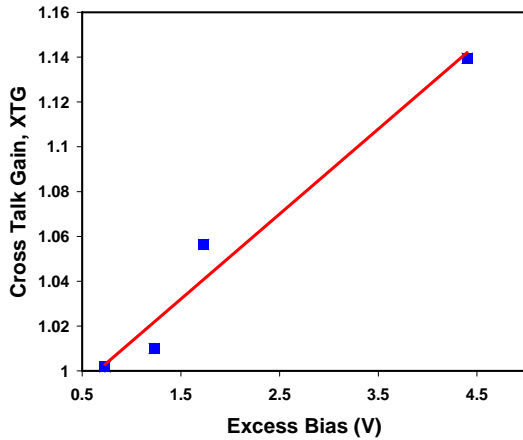


Figure 11. Cross-talk gain (XTG), which represents the average number of pixels that actually fire for a single initiating event as a function of excess bias for a 100 pixel SSPM (20 μm diameter, 46 μm pitch).

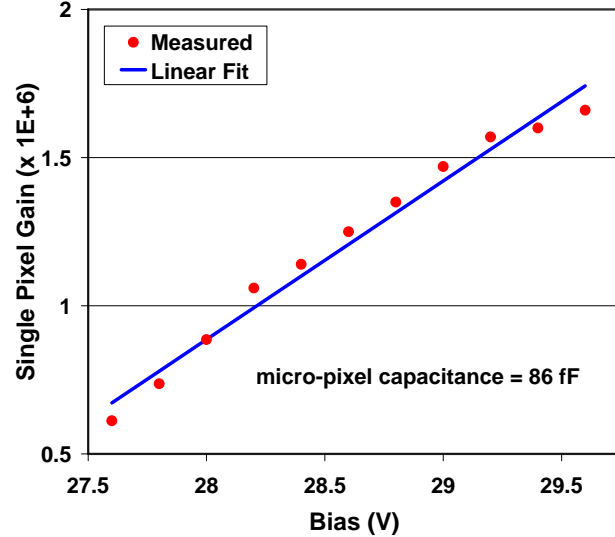


Figure 12. Single micro-pixel gain versus bias for 3x3 mm^2 SSPM with 785 micro-pixels (30 μm diameter). From the slope, the micro-pixel capacitance (C_{pixel}) is estimated to be 86 fF.

larger 3x3- mm^2 SSPM were also carried out using the approach similar to that for the smaller 100-pixel SSPM. The gain versus bias plot for the 3x3- mm^2 SSPM is shown in **Figure 12**. As seen in the figure, gain values $>10^6$ are readily achieved at excess bias of few volts above the breakdown value of $\sim 27 \text{ V}$. From the slope of the gain versus bias plot shown in **Figure 12**, the

micro-pixel capacitance was estimated to be ~ 86 pF. The higher gain of the larger SSPM is partly due to larger micro-pixel size, which leads to higher micro-pixel capacitance. Cross-talk measurements were also conducted using the larger 3×3 mm² SSPM. Due to larger inter-pixel spacing used in construction of these devices (100- μ m pitch), virtually no cross-talk was measurable up to excess bias value of 3 V. Finally, effect of temperature on the gain of 3×3 mm² SSPM was studied over -15 °C to $+30$ °C temperature range. The gain variation (at a constant applied bias, 29 V) over this temperature range was found to be linear with a slope of $\sim 2.5\%/^{\circ}\text{C}$. An adjustment in bias (of few volts) can be used to maintain constant gain over the expected operating temperature range.

Overall, the measured parameters for the smaller SSPM with 100 micro-pixels and larger SSPM with 785 micro-pixels were found to be fairly consistent. These experiments confirmed the basic performance parameters of SSPMs such as high gain, low dark counts and low cross-talk and after-pulsing effects.

9.4. EVALUATION OF 3×3 mm² SSPMS WITH LSO/LYSO CRYSTALS FOR PET

Once the basic evaluation of the SSPMs was completed, we characterized their performance for PET imaging [Shah 07a]. This investigation was conducted using 3×3 mm² SSPMs (785 pixels with 30 μ m diameter in 28×28 pixel format, 100- μ m pitch), which were coupled to LSO/LYSO scintillators with 3×3 mm² cross-section and 15 to 20 mm depth. Energy resolution, timing resolution, and depth of interaction measurements were then conducted with these detectors using 511-keV gamma-rays (²²Na source).

Energy Resolution Studies

The Geiger mode operation of the micro-pixels in the SSPM greatly simplifies the necessary readout electronics. The Geiger mode avalanche signal output from a micro-pixel is constant for a given bias and is relatively large (with gain in 10^5 to 10^6 range). Therefore, the signal output, or current pulse, from all pixels can be summed. The amplitude of the summed signal output from all micro-pixels is directly related to the energy of the input pulse. A pulse height distribution, therefore, represents an energy spectrum of the radiation seen by the scintillation crystal coupled to the SSPM. We coupled our 3×3 -mm² SSPM to a matching LYSO crystal with 3×3 -mm² cross-section and 15-mm depth. The scintillation crystal was wrapped in Teflon tape and optical coupling grease was used at the SSPM-LYSO interface in order to enhance overall light collection. The detector was irradiated with 511-keV gamma-rays (²²Na source). Due to large gain of the SSPMs, the common output of SSPM was directly fed to the shaping amplifier (Canberra # 2020) without any preamplifier. The amplifier output (with 250 ns shaping time) was processed using a multichannel analyzer (Amptek 8000A) connected to a PC. **Figure 13** shows the ²²Na spectrum collected with the SSPM-LYSO detector. The energy resolution of the 511-keV photopeak is $\sim 22\%$ (FWHM), which is promising considering the very early stage of SSPM development. At this stage, the energy resolution is primarily limited by the relatively low fill-factor (9%) of the SSPMs used. By improving the fill-factor of the SSPMs, considerable improvement in energy resolution should be possible.

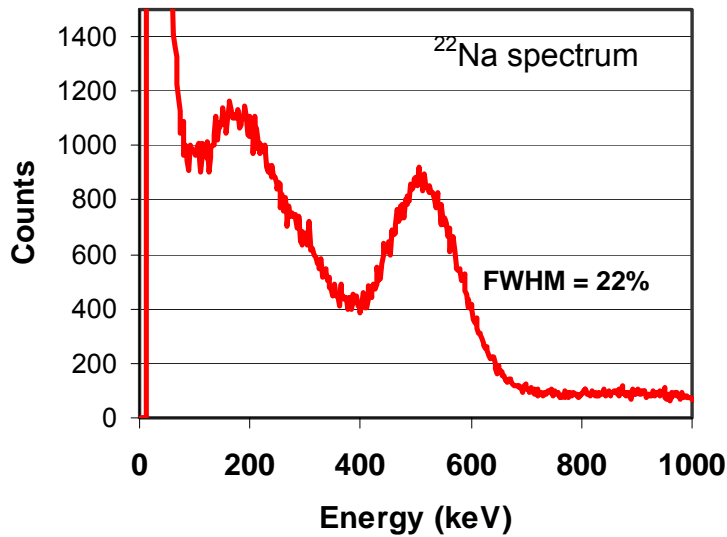


Figure 13. ^{22}Na spectrum recorded with a $3 \times 3 \text{ mm}^2$ SSPM upon coupling it to LYSO scintillator ($3 \times 3 \text{ mm}^2$ cross-section, 15 mm depth).

Timing Resolution Studies:

Timing spectra were measured in order to determine the coincidence timing resolution capability of the LYSO/SSPM detector when irradiated with 511-keV gamma-rays emitted by a ^{22}Na source. As shown in **Figure 14**, LYSO crystal ($3 \times 3 \times 15 \text{ mm}^3$) was coupled to a $3 \times 3 \text{ mm}^2$ SSPM, which was operated in coincidence with a fast PMT (Hamamatsu H6533) coupled to 2 mm x 2 mm x 10 mm LSO crystal. The SSPM and PMT outputs were shaped with Canberra 2111 timing filter amplifiers. Each amplifier output was fed to a constant fraction discriminator (CFD, Canberra #1428). The output from the PMT channel was used as the “start” signal and the output from the SSPM channel (with an appropriate delay) provided the “stop” signal. Both signals were fed to a time-to-amplitude converter (TAC, Canberra Time Analyzer Model 2043) and its output was analyzed by a MCA (Amptek 8000A) connected to a personal computer.

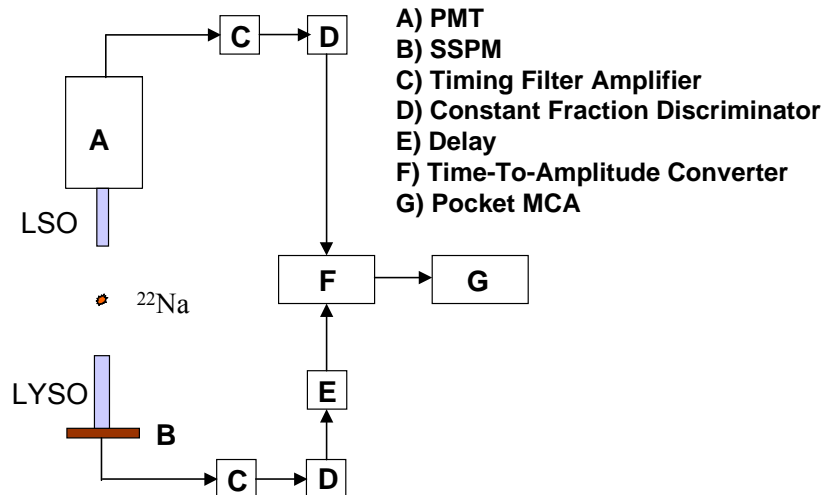


Figure 14 Experimental arrangement used to measure timing resolution of SSPM-LYSO detector operating in coincidence with PMT-LSO detector.

Energy windows were set around the 511-keV peak for PMT and SSPM channels. The timing filter amplifier time constants were adjusted to optimize the signal-to-noise ratio and pulse rise-time. A timing spectrum obtained with this setup is shown in **Figure 15**. The coincidence timing resolution was estimated to be ~ 1.6 ns (FWHM), which is encouraging, considering the low fill-factor ($\sim 9\%$) of the SSPMs used. The relatively high timing resolution of SSPMs is primarily due their fast response, high gain and high signal-to-noise ratio. The timing resolution of two PMT-LSO detectors was measured to be ~ 300 ps (FWHM). Further improvement in timing resolution is expected upon optimization of the light collection efficiency of these SSPMs, which should be possible with the devices having higher fill-factor.

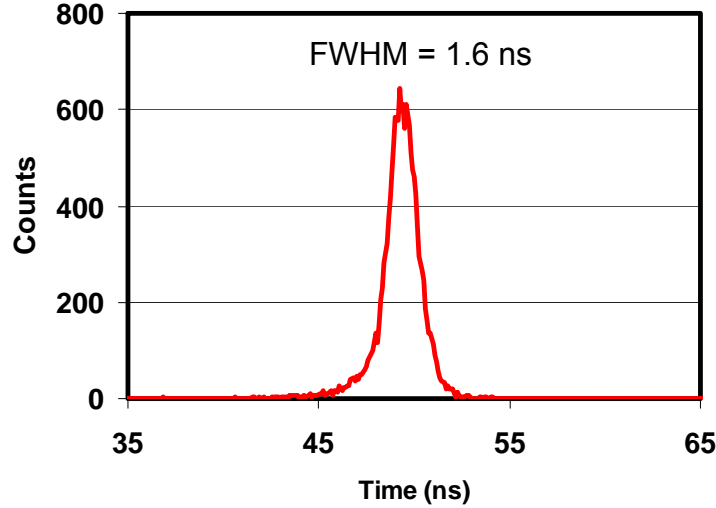


Figure 15. Timing resolution spectrum for SSPM-LSO crystal operating in coincidence with a PMT-LSO detector upon irradiation with 511 keV gamma-ray pairs.

Depth of Interaction Studies:

Depth of interaction (DOI) measurements were conducted using SSPMs. The basic method involved coupling two SSPMs to opposite ends of a LSO crystal with 3×3 mm² cross-section and 20 mm depth. The crystal was cut with a saw and only its two 3×3 mm² faces (to be coupled to SSPMs) were polished. Different depths within the LSO crystal were irradiated with 511-keV gamma-rays (²²Na source) using electronic collimation. By comparing the signal from two SSPMs for each depth of interaction, the DOI location was estimated. The signal from each SSPM would depend on DOI and as the DOI location moves closer, its signal would be expected to increase. **Figure 16** shows a schematic diagram of the experimental design used in conducting the DOI measurements, while **Figure 17** shows a photograph of a corresponding experimental setup.

A slab of LSO (2x2x10 mm³, coupled to a PMT) and a ²²Na point source are mounted on a translation table. This PMT-LSO detector projects a 2 mm wide beam of 511 keV gamma-rays on the $3 \times 3 \times 20$ mm³ test LSO crystal that is sandwiched

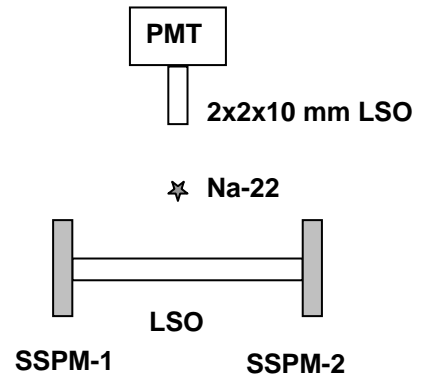


Figure 16: Setup for measuring DOI resolution.

between two SSPMs. Events corresponding to interactions at one depth in the LSO array are selected by coincidence measurement of the 511 keV annihilation photons between the LSO-PMT detector and the test LSO crystal of the SSPM-LSO-SSPM detector. The ratio of the signal amplitude (E_2) of SSPM-2 to the sum of the signal amplitudes in both SSPMs ($E_2/(E_1+E_2)$) is used to calculate the DOI. As shown in **Figure 18**, the interaction location was moved from one end of the module (near SSPM-1) to the other end (near SSPM-2) by moving the source and the LSO-PMT detector using the translation table and the signal amplitude of each SSPM was measured as a function of DOI. As expected, the amplitude of each SSPM decreased as the interaction depth moved farther away from it, which confirms that DOI information can be estimated by comparing the signal of two SSPMs.

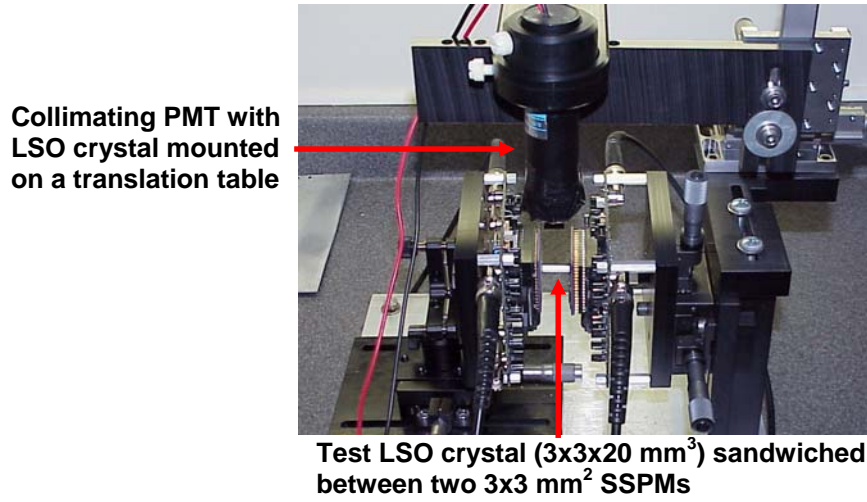


Figure 17. Photograph of the experimental setup used for DOI measurements.

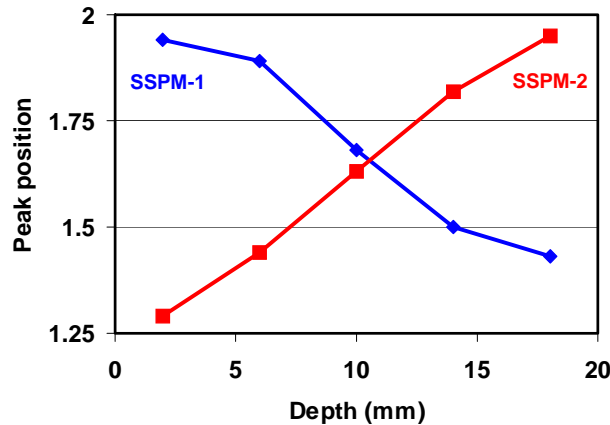


Figure 18. Response of two SSPMs as DOI is moved from SSPM-1 to SSPM-2.

Depth profiles were generated by recording large number of events with both SSPMs at each DOI location and estimating the DOI location (using expression: $E_2/(E_1+E_2)$) on an event-by-event basis). Resulting depth profiles at various DOI locations are shown in **Figure 19**. By estimating the broadening of each depth profile, the DOI resolution was estimated as a function

of depth and the results are presented in **Figure 20**. From these figures, we estimate the average DOI resolution across the detector module to be ~ 5.4 mm (FWHM).

Overall, these results are encouraging and indicate that a solid-state photomultiplier, fabricated using standard CMOS processing, is a promising new photodetector for readout of scintillation crystals in PET imaging. Reasonably high energy, timing and DOI resolution has been achieved with the SSPMs coupled to LSO/LYSO detectors. One limitation of these 1st generation SSPMs, particularly the larger 3×3 mm² devices, was their relatively low fill-factor.

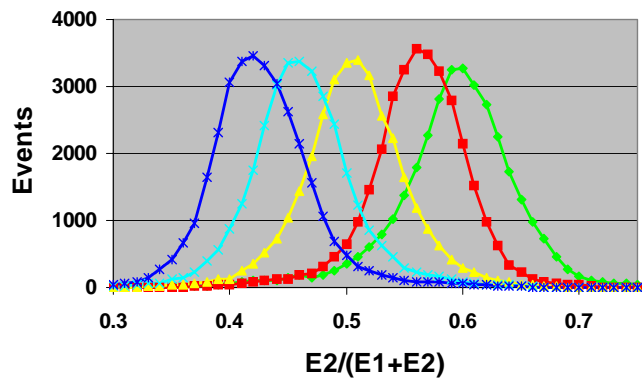


Figure 19. Depth profiles for various DOI locations. DOI is estimated on an event-by-event basis using expression: $[E_2/(E_1+E_2)]$, where E_1 and E_2 are signals from SSPM-1 and SSPM-2, respectively. The values of 0 and 1 for $[E_2/(E_1+E_2)]$ corresponds to DOI locations near SSPM-1 and SSPM-2, respectively.

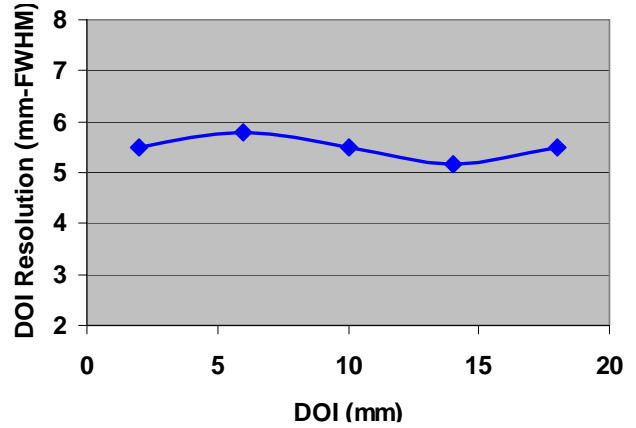


Figure 20. DOI resolution (in mm-FWHM) as a function of depth for the SSPM-LSO-SSPM module.

9.5. SECOND GENERATION SSPMS

Encouraged by the overall performance of the 1st generation SSPMs with 3×3 mm² size, we have designed and built second generation devices that have up to seven times higher fill-factor than the 1st generation devices [Shah 07b]. These new SSPMs used square micro-pixels. The design approach for these 2nd generation devices is shown in **Figure 21** where a CMOS chip (3×3 mm² area) with four separate SSPM designs (each with 1.5×1.5 mm² area), one in each quadrant is shown. The design parameters for the SSPMs in each quadrant (*a*, *b*, *c*, and *d*) are listed in **Table 1**.

TABLE I
Design and Operating Parameters of 2nd Generation SSPMs

Active area [mm ²]	Pixel size/Pixel Pitch	# of pixels	Fill factor	Gain @ 30 V	Breakdown voltage
(a) 1.5×1.5	$30 \mu\text{m}/56 \mu\text{m}$ (square)	576	29%	1×10^6	27.5 V
(b) 1.5×1.5	$30 \mu\text{m}/43 \mu\text{m}$ (square)	961	46%	1×10^6	27.5 V
(c) 1.5×1.5	$50 \mu\text{m}/76 \mu\text{m}$ (square)	324	43%	3.5×10^6	27.5 V
(d) 1.5×1.5	$50 \mu\text{m}/63 \mu\text{m}$ (square)	441	61%	3.5×10^6	27.5 V

We have conducted scintillation studies (energy and timing resolution) with these SSPMs and the results are reported here for the $1.5 \times 1.5 \text{ mm}^2$ SSPM with $30 \text{ }\mu\text{m}$ pixels and 46% fill-factor (design *b* in **Figure 21** and **Table 1**). This SSPM was coupled to a matching LYSO crystal ($1.5 \times 1.5 \text{ mm}^2$ cross-section, 10 mm length). Upon irradiating this detector at room temperature with 511 keV gamma-rays (^{22}Na source), energy resolution (FWHM) of $\sim 11\%$ was measured (see **Figure 22**). There was a non linearity between 511 keV and 1275 keV. Therefore, the linearity of the detector was studied. It was observed that the detector was almost linear up to 511 keV. Energy resolution of the same scintillator was $\sim 10.5 \%$ when coupled to a PMT with a bialkali photocathode, which is very close to the resolution recorded with SSPM-LYSO detector.

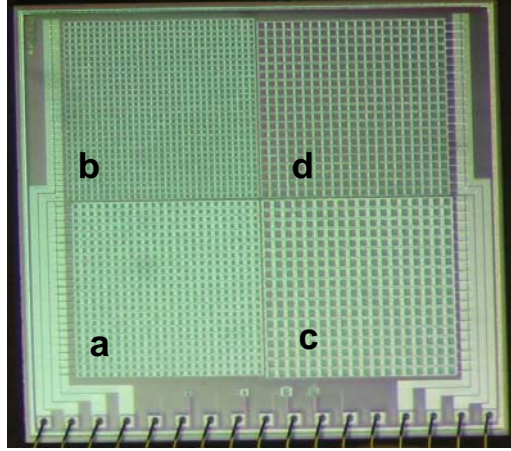


Figure 21. Photograph of $3 \times 3 \text{ mm}^2$ CMOS chip which is a 2×2 array of $1.5 \times 1.5 \text{ mm}^2$ SSPMs. The design parameters for each SSPM is presented in **Table 1**.

To measure timing resolution, the SSPM-LYSO detector was then operated in coincidence with a PMT-LSO reference detector using the setup shown earlier in **Figure 14**. Each detector was irradiated with 511 keV gamma-ray pairs and upon processing these events using fast electronics, timing resolution of 530 ps (FWHM) was measured at room temperature (see **Figure 23**). This result is exciting and confirms potential of SSPMs for TOF-PET imaging. The energy and timing resolution results reported in this section (**Figures 22 & 23**) are significantly superior to those reported in previous section (**Figures 13 & 15**), which is primarily due to much higher fill-factor of the new, 2nd generation SSPMs.

Depth of interaction (DOI) measurements were also conducted using the 2nd generation SSPMs (design *b* in **Figure 21** and **Table 1**). A detector module was constructed by coupling a $1.5 \times 1.5 \times 20 \text{ mm}^3$ LYSO scintillator with two $1.5 \times 1.5 \text{ mm}^2$ SSPMs at either ends. The $1.5 \times 1.5 \text{ mm}^2$ surfaces of LYSO were optically polished while other four lateral surfaces were as-cut. The lateral surfaces of the crystal were wrapped with Teflon tape and two polished ends were kept open. The experimental design and measurement techniques were same as described in the previous section (see **Figures 16 & 17**). As before, a dual ended readout approach was used to determine the DOI. The distribution of the ratio signals, $\text{SSPM2}/(\text{SSPM1}+\text{SSPM2})$, calculated on an event-by-event basis is shown in **Figure 24**. Each curve in the **Figure 24** corresponds to the distribution of ratio signals for interactions at one particular DOI position. The DOI

resolution was estimated from the broadening of these depth profiles. **Figure 25** shows the change in DOI resolution with respect to the depth. The DOI resolution was ~ 2.5 mm along the entire length of the scintillator. Once again the DOI resolution shown in **Figure 25** is superior to that reported in **Figure 20** due to much higher fill-factor of the new, second generation SSPMs. Even higher performance should be possible upon further optimization of the overall SSPM photodetection efficiency and by using brighter and faster scintillators (such as $\text{LaBr}_3\text{:Ce}$, CeBr_3 and $\text{LuI}_3\text{:Ce}$).

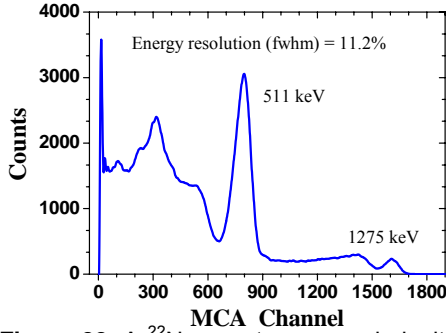


Figure 22. A ^{22}Na spectrum recorded with a $1.5 \times 1.5 \times 10 \text{ mm}^3$ LYSO coupled to a $1.5 \times 1.5 \text{ mm}^2$ SSPM (46% fill factor) at room temperature.

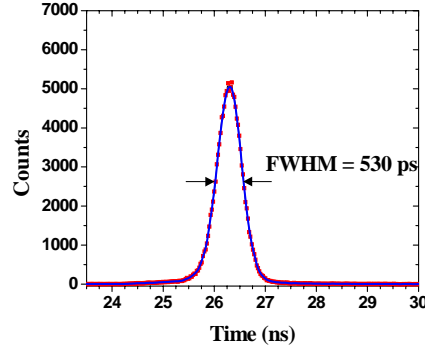


Figure 23. Timing spectrum recorded for a $1.5 \times 1.5 \times 10 \text{ mm}^3$ LYSO coupled to a $1.5 \times 1.5 \text{ mm}^2$ SSPM and a LSO-PMT detector operating in coincidence at room temperature. The coincidence timing resolution was measured to be 530 ps (FWHM).

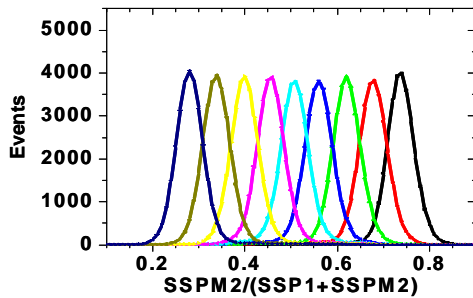


Figure 24. Distribution of signal ratio on an event-by-event basis calculated at 9 different DOI locations 2 mm apart over 20 mm depth of the scintillator.

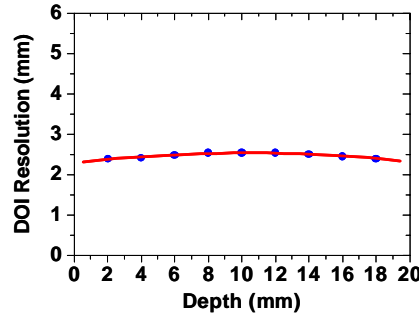


Figure 25. DOI resolution as a function of interaction depth.

9.6. STUDY OF POSITION SENSITIVE SSPMs (PS-SSPMs)

In the ultimate use of SSPMs for PET imaging, it would be useful to consider signal multiplexing schemes in some situations because of large number of scintillation crystals and associated electronic channels that are needed in PET systems. Fortunately, the high gain of SSPMs allows the use of a simple resistor network to create charge sharing that allows signal multiplexing [Shah 07b, Dokhale]. We have recently performed a feasibility evaluation of such a position sensitive SSPM (or PS-SSPM) configuration. This imaging detector, which is shown in **Figure 26**, consisted of an array of 4×4 SSPMs (each with $1.5 \times 1.5 \text{ mm}^2$ size with $30 \mu\text{m}$ diameter micro-pixels, $100 \mu\text{m}$ pitch). Each SSPM element was coupled to an LYSO

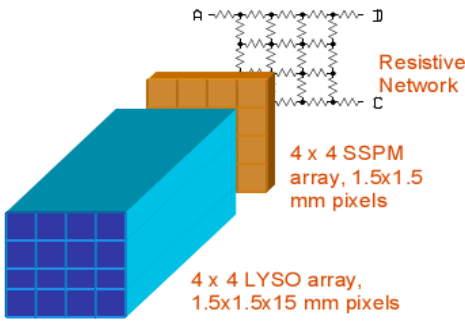


Figure 26. Position sensitive detector based on 4x4 array of LYSO-SSPM detectors readout by a resistive network that provides charge division with four outputs (A, B, C and D). The event location is determined from the signal collected at the four outputs using expression:

$$X = [(D+C)-(A+B)]/(A+B+C+D)$$

$$Y = [(A+D)-(B+C)]/(A+B+C+D)$$

reduction in the number of electronic channels for the detector shown in **Figure 26**. In order to test this concept, the SSPM-LYSO array illustrated in **Figure 26** was irradiated with 511 keV gamma-rays (^{22}Na source). The resulting flood image is shown in **Figure 27**. Each element is well resolved in the image, indicating successful implementation of resistive charge division for signal multiplexing to create PS- SSPMs.

scintillation crystal ($1.5 \times 1.5 \text{ mm}^2$ cross-section, 15 mm depth) as shown in the figure. In place of individual readout of each SSPM, the output of each element was connected to a simple resistor network that provided charge division and had four outputs. Comparison of the signal collected at each of the four outputs provided position information (using the equations summarized in **Figure 26**), while the sum of the four signals provided energy and timing information for the event. Thus, in this PS-SSPM, the charge division provided position encoding with only four outputs, thereby providing a four-fold

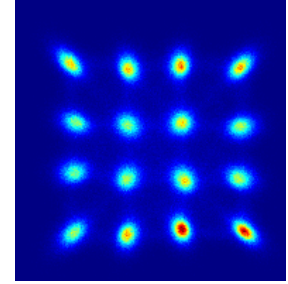


Figure 27. Flood image (^{22}Na source, 511 keV photons) with 4x4 SSPM-LYSO array shown in **Figure 26**. External resistive network was used between SSPMs for charge division and each element is well resolved in the image.

9.7. MICRO-PIXEL LEVEL POSITION SENSITIVE SSPMs

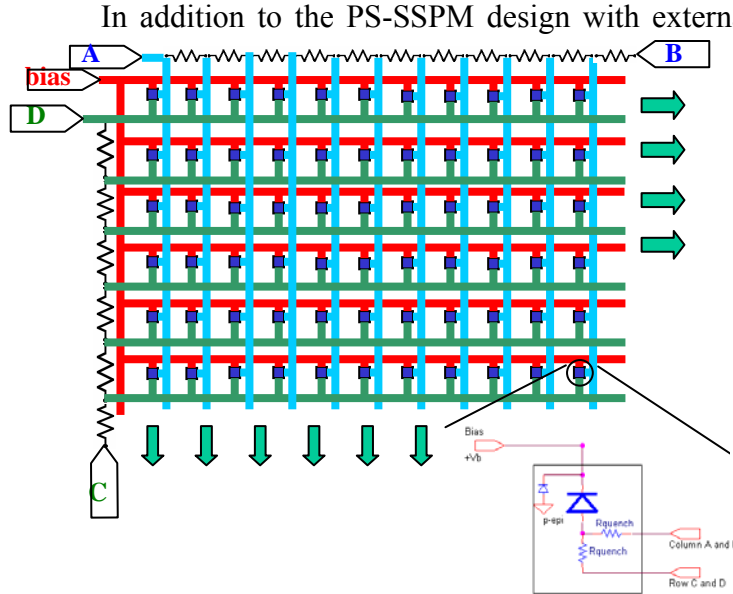


Figure 28. Schematic of a PS-SSPM design that provides spatial information at a micro-pixel level. Each micro-pixel has two resistive outputs (see the inset), one connected to a row bus and other to a column bus. These row and column buses have resistors for charge division to provide position information. For this configuration, we estimate X & Y locations using expressions: $X = (B-A)/(A+B)$ and $Y = (D-C)/(C+D)$.

In addition to the PS-SSPM design with external resistive network (see **Figure 26**), we have also designed, built and evaluated other configurations of PS-SSPMs, where the individual micro-pixels provide position information [Shah 09]. **Figure 28** shows one design of such a new PS-SSPM, where each micro-pixel of the SSPM has two resistive outputs, one connected to the row bus and the other to the column bus. These row and column buses have a resistive network as shown in **Figure 28** which allow identification of the micro-pixel where event occurs based on charged sharing (using equations summarized in **Figure 28**). CMOS-technology allows creating the resistive network directly on the

SSPM chip, thereby minimizing the external components required. The PS-SSPM design shown in **Figure 28** can provide much higher spatial resolution compared to that shown in **Figure 26** with an external resistive network between the SSPM elements. A small format PS-SSPM with design shown in **Figure 28** has been designed and built at RMD (see **Figure 29**). This 1.5x1.5 mm² PS-SSPM had 30 μ m (square) micro-pixels, 46% fill-factor with 1 k Ω resistors in the row and column buses that are integrated on the PS-SSPM chip itself.

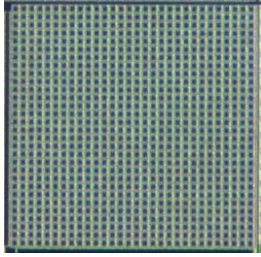


Figure 29. Photograph of a 1.5x1.5 mm² PS-SSPM with design shown in **Figure 28** (30 μ m micro-pixels, 1 k Ω resistors in row and column buses).

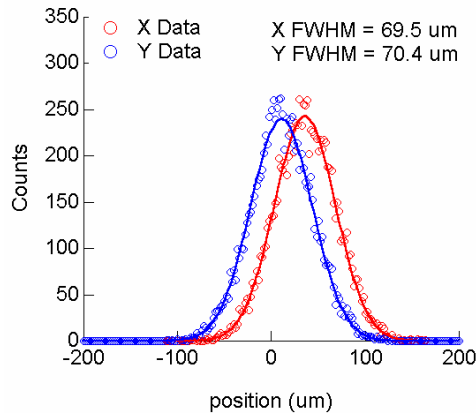


Figure 30. Intrinsic spatial resolution of 1.5x1.5 mm² PS-SSPM shown in **Figure 29** (30 μ m micro-pixels, 1 k Ω resistors in row and column buses) measured using a 635 nm laser spot (15 μ m size). 10K events were processed at a fixed position and a histogram of x and y values provided \sim 70 μ m (FWHM) spatial resolution.

gamma-rays on the 1.5x1.5x20 mm³ test LYSO crystal that was sandwiched between two 1.5x1.5 mm² micro-pixel level PS-SSPMs. Events corresponding to interactions at one depth in the LYSO array were selected by coincidence measurement of the 511 keV annihilation photons between the LSO-PMT detector and the test LYSO crystal of the PSSSPM-LYSO-PSSSPM detector. At each depth, for all events, the signals from both PS-SSPMs were collected and processed. Since DOI is represented by the ratio: (PSSSPM1/PSSSPM1+PSSSPM2), at

The intrinsic spatial resolution of this PS-SSPM was measured to be \sim 70 μ m by focusing a 635 nm laser spot (15 μ m size) on the PS-SSPM surface, processing 10,000 events at a fixed location to generate x and y locations using equations listed in **Figure 28** and plotting histograms of x and y locations (see **Figure 30**). This study confirms very high spatial resolution of the new PS-SSPMs. Successful imaging of 500 μ m LYSO elements (5 mm thick) with high spatial linearity has been accomplished with this new PS-SSPM upon exposure to 511 keV γ -rays (see **Figure 31**), confirming its promise. With the PS-SSPM shown in **Figure 29**, we have also conducted energy and timing resolution measurements by coupling it to a 1.5x1.5x20 mm³ LYSO crystal. Upon exposure to 511 keV gamma-rays (²²Na source), energy resolution of 15% (FWHM) and 1-ns timing resolution have been achieved with these micro-pixel level PS-SSPMs and LYSO scintillators [Shah 09].

We have also conducted depth of interaction measurements with these new micro-pixel level PS-SSPMs. A 1.5x1.5x20 mm³ LYSO crystal was sandwiched between two 1.5x1.5 mm² PS-SSPMs. The crystal was cut with a saw and only its two 1.5 x 1.5 mm² faces (coupled to the SSPMs) were polished to provide depth-dependence of the signal. Different depths (at 2 mm intervals) within this LYSO crystal were irradiated using electronic collimation provided by a separate PMT-LSO detector. This PMT-LSO detector along with a ²²Na point source were mounted on a translation table and projected a beam of 511 keV

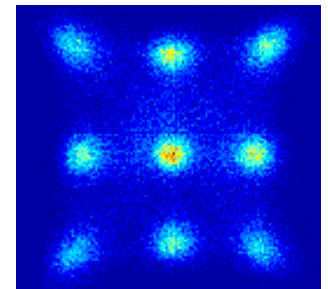


Figure 31. Image of LYSO array (500 μ m pixels, 5 mm depth) with 1.5 mm PS-SSPM shown in **Figure 29** upon exposure with 511 keV γ -rays (²²Na source).

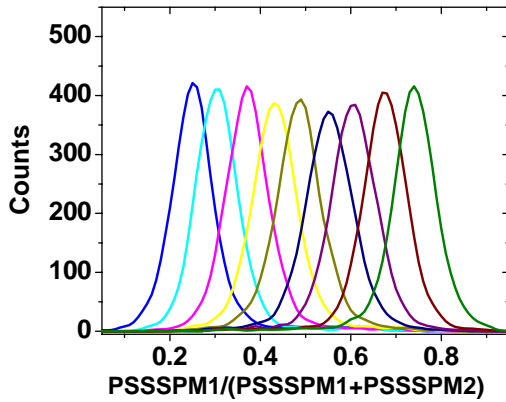


Figure 32. Distribution of ratio signals on an event-by-event basis calculated from signals acquired at 9 different DOI locations 2 mm apart.

These results confirm the promise of these new micro-pixel level PS-SSPMs for small animal PET, including combined PET imaging. Other micro-pixel SSPM designs where a 2-D resistive network is created at the micro-pixel level or an active source follower configuration links the output of the micro-pixels to the resistive row and column buses are also being investigated for high resolution PET [Shah 09].

9.8. CONCLUSIONS

The results of SSPM evaluation are encouraging and indicate that CMOS techniques can be used to build silicon photomultipliers with high gain, low dark count-rate and fast response. Good energy, timing and DOI resolution as well as position sensitivity (upon signal multiplexing with resistive charge division) can also be obtained with these devices. Compared to other solid-state photodetectors, the main advantages offered by SSPMs for PET include much higher gain, faster response and low bias requirements. Particularly encouraging aspect of SSPMs is their excellent timing resolution (in sub-nanosecond range), which makes it feasible to consider SSPMs for TOF PET studies. On-going research is focusing on further improvement in fill-factor, blue response and overall photodetection efficiency of SSPMs. Fabrication of monolithic multi-element arrays as well as position sensitive structures (with the resistive network integrated on chip itself) is also being carried out. Simultaneous PET-MR studies are also being conducted with CMOS SSPMs [Dokhale 08].

9.9. REFERENCES

- Beyer, T., Townsend, D. W., Brun, T., Kinahan, P. E., Charron, M., Roddy, R., Jerin, J., Young, J., Byars, L., and Nutt, R., *A combined PET/CT scanner for clinical oncology*, Journal of Nuclear Medicine, 41(8), 1369-79.
- J.T. Bushberg, J.A. Seibert, E.M. Leidholdt, and J.M. Boone, **The Essential Physics of Medical Imaging**, Williams and Wilkins, (1994).

each DOI location, a large number of events were processed to generate a depth profile. In **Figure 32**, such depth profiles are shown for all DOI locations. The broadening of these depth profiles provides an estimation of DOI resolution as a function of depth (shown in **Figure 33**). As seen in the figure, the average DOI resolution for all depths is about 3.4 mm (FWHM). The actual DOI resolution is possibly better than 3.4 mm given that for our geometry, a 2 mm wide band of gamma rays irradiated the test LYSO crystal at each DOI location.

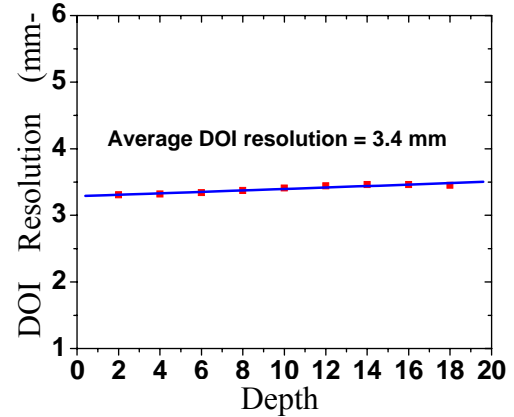


Figure 33. DOI resolution (in mm) versus interaction depth, with an average resolution across all depths of 3.4 mm (FWHM).

- P. Buzhan, B. Dolgoshein et al., *An Advanced Study of Silicon Photomultiplier*, ICFA. Instrum.Bull.23:28-41, (2001).
- P. Buzhan, B. Dolgoshein, L. Filatov, A. Ilyin, V. Kantserov, V. Kaplin, A. Karakash, F. Kayumov, S. Klemin, E. Popova, and S. Smirnov, *Silicon photomultiplier and its possible applications*, *Nuclear Instruments and Methods in Physics Research, Section A*, vol. 504, (2003).
- P. Buzhan, B. Dolgoshein, E. Garutti, M. Groll, A. Karakash, V. Kaplin, V. Kantserov, F. Kayumov, S. Klyomin, N. Kondratieva, A. Pleshko, E. Popova, F. Sefkow, *Timing by Silicon Photomultiplier: A possible application for time of flight measurements*, Nucl. Inst. & Meth. In Phys. Res. A 567, pp 353-355, (2006)
- P. A. Dokhale, R. Nagarkar, R. Robertson, M. McClish, C. Stapels, J. Christian, G. Entine, M. Squillante and K.S. Shah et al., "Performance measurements of CMOS-SSPM as a PET detector," IEEE Conference record, (2007).
- P.A. Dokhale, Y. Wu, et al. "Performance of a LYSO-SSPM PET detector for combined PET/MRI applications," presented at IEEE NSS-MIC, Dresden, Germany, (2008).
- B. Dolgoshein, et al., *Silicon photomultipliers in particle physics: possibilities and limitations*. Proceedings of 42nd Workshop "Innovative Detectors for Supercolliders" Erice, Italy, 28 Sep - 4 Oct (2003), people.roma2.infn.it/~elettronica/SiPM/Cartella2/other/Dolgoshein.doc
- B. Dolgoshein, Large area Silicon Photomultipliers: Performance and Applications, presented at New Developments in Photodetectors, Beaune, June, (2005), www.jlab.org/~rondon/sane/mtg8/Dolgoshein.pdf
- R. Grazioso, R. Ladebeck, M. Schmand, R. Krieg, APD-Based PET for Combined PET-MR Imaging, Proc. Intl. Soc. Mag. Res. Med., Vol.13, (2005).
- Phelps, M. E., *Positron emission tomography provides molecular imaging of biological processes*, Proc Natl Acad Sci, 97(16), 9226-9233, (2000).
- V. Saveliev, V. Golovin "Silicon avalanche photodiodes on the base of metal-resistor-semiconductor (MRS) structures" *Nuclear Instruments and Methods in Physics Research A* 442, p.223, 2000
- K.S. Shah, et al., Position Sensitive Solid-State Photomultipliers, Systems and Methods, U.S. Provisional Patent Appl. No. 61/185,169, (2009)
- K.S. Shah, Final Report on DOE SBIR Phase I Project "A Fast, High Gain Photodetector for PET", (Principal Investigator – Kanai S. Shah), U.S. Department of Energy, April, (2007a)
- K.S. Shah, "RMD's CMOS SSPM", poster presented to Defense Threat Reduction Agency, June (2007b).
- C. J. Stapels, W. G. Lawrence, F. L. Augustine, and J. F. Christian, "Characterization of a CMOS Geiger Photodiode Pixel," IEEE Transactions on Electron Devices, vol. 53, pp. 631, (2006).

CHAPTER 10: CONCLUSIONS AND FUTURE TRENDS

The field of scintillators is undergoing a major renaissance at present. The discovery of new materials as well as optimization of already established materials is occurring at a furious pace. This activity is driven by synergy in demands of various applications such as medical imaging, nuclear physics, nuclear non-proliferation monitoring, materials research, well-logging, non-destructive evaluation and other related fields. While some demands may diverge amongst these applications, many desired features are indeed common. This includes high light output, high proportionality, high-energy resolution, reasonably fast response and low cost.

The intense efforts aimed at search of new scintillation crystals have lead to discovery of several compositions that have light output approaching 100,000 photons/MeV. This includes Ce^{3+} doped compositions such $\text{LuI}_3:\text{Ce}$ and Eu^{2+} doped compositions such as $\text{SrI}_2:\text{Eu}$ (which were reported earlier). In terms of selection of the scintillators covered in this thesis for medical imaging as well as other potential applications, in addition to performance parameters, the feasibility of producing crystals of these materials in large sizes in a cost effective manner is also a key consideration.

As discussed earlier, growth of large $\text{LaBr}_3:\text{Ce}$ crystals is indeed being carried out by a commercial company (Saint Gobain) and these crystals are finding use in homeland security monitoring, well-logging and physics research. A prototype, clinical TOF-PET scanner based on LaBr_3 (with 5% Ce) doping is under exploration at the University of Pennsylvania (U-Penn) with focus being to illustrate the advantage of higher energy and timing resolution of LaBr_3 on the eventual image quality. On-going U-Penn results appear to validate this expectation [Karp]. U-Penn team is also exploring LaBr_3 crystals with Ce doping of 30% as well as CeBr_3 crystals in view of their potential to provide higher timing resolution (due to their faster response compared to $\text{LaBr}_3:5\%\text{Ce}$) without any major compromise in light output or energy resolution. The crystal growth aspects of $\text{LaBr}_3:30\%\text{Ce}$ and CeBr_3 are similar to those for $\text{LaBr}_3:5\%\text{Ce}$ using the Bridgman growth being performed at RMD. Initial bench-top results at U-Penn do confirm faster rise-time performance of $\text{LaBr}_3:30\%\text{Ce}$ and CeBr_3 [Karp]. A wider set of experiments with prototype arrays are now planned to explore the full potential of $\text{LaBr}_3:30\%\text{Ce}$ and CeBr_3 in TOF-PET.

Regarding $\text{LuI}_3:\text{Ce}$, while the scintillation properties are exceptional (high gamma-ray stopping efficiency, fast response and very high light yield and proportionality), its complex, rhombohedral structure with cleavage planes makes growth of high quality, large crystals very challenging. This makes implementation of traditional PET modules using 20-30 mm thick scintillation blocks and arrays very difficult. One recent approach has been to employ $\text{LuI}_3:\text{Ce}$ in form of a layered PET detector where each layer is only 2-3 mm thick and has its own optical readout. This concept may allow demonstration of unique capabilities of $\text{LuI}_3:\text{Ce}$ in an actual PET module.

Two new scintillator families, alkaline earth halides doped with Eu^{2+} and elpasolites doped with Ce^{3+} while not very promising for PET (due to relatively low gamma-ray stopping efficiency and slow response), appear to be very attractive for single photon emission computed tomography (or SPECT). Here the high luminosity and excellent proportionality of the scintillators allow them to provide high energy resolution at low gamma-ray energies of interest in SPECT. For example, at 122 keV gamma-ray energy (similar to 140 keV gamma-ray energy for the most common SPECT radioisotope, $^{99\text{m}}\text{Tc}$), the energy resolution of selected

compositions such as $\text{SrI}_2\text{:Eu}$ and $\text{Cs}_2\text{LiLaBr}_6\text{:Ce}$ is below 6% (FWHM), an encouraging result that should enable better scatter rejection in SPECT.

Silicon based photodetectors are making in-roads in several small animal PET and PET-MR imaging systems. The main challenges they face in getting adapted for clinical PET imaging systems are their timing properties (particularly for APDs) and their cost (for both APDs and SSPMs). Because the SSPMs are fabricated using the standard CMOS process, they can benefit from the economies of scale offered by this method upon mass production. Integration of next stage of signal processing to the SSPM elements in the same fabrication run is an additional advantage. APDs do provide higher optical detection efficiency than SSPMs at present, which can be important in resolving ultra-high resolution scintillation segments. System designers will have to consider the cost, performance, robustness and flexibility aspects in selecting the appropriate photodetectors.

References:

J. Karp, Enabling Technology for Time-of-Flight PET Imaging, Presented at SORMA XII, Ann Arbor, MI, May (2010).

CHAPTER 11: SUMMARY

The focus of this thesis is on new detection technologies that can be used in advancing nuclear medicine modalities, particularly positron emission tomography (PET). Several detection technologies are covered in this thesis. First, new Ce^{3+} doped rare earth trihalide scintillators that can be used in advancing PET imaging are discussed. Here, the particular attention is paid to high light output and high proportionality to achieve high-energy resolution (for good scatter rejection) and fast response for high timing resolution along with possibility of providing time-of-flight data collection (to reduce randoms and to reduce noise in the reconstructed image). In addition to discussion of new scintillators for use in PET, two classes of new scintillators (Ce^{3+} doped elpasolites and Eu^{2+} doped alkaline earth halides) that provide high proportionality as well as energy resolution over a broad range of energies for use in single photon emission computed tomography (or SPECT) are also covered. The main scintillation characteristics such as light output, peak emission wavelength and decay time constant(s) for all the scintillators discussed in this thesis are presented in **Table 1**.

In addition to new scintillators, two solid state photodetector technologies are also covered in this thesis. This includes silicon avalanche photodiodes (APDs) and silicon based solid state photomultipliers (SSPMs). Standard as well as position sensitive versions of these photodetectors are covered with particular attention paid to the use of these new devices in small volume PET imaging. PET module designs with an ability to provide depth of interaction (in the scintillator element) in order to overcome parallax error in image reconstruction are discussed. A comparison of some of the important parameters of APDs, SSPMs and PMTs is provided in **Table 2**.

In **chapter 1** of this thesis, the emerging needs in nuclear medicine modalities, such as high energy resolution for PET and SPECT and high timing resolution (including TOF capability) and DOI encoding capability for PET are discussed. These needs are tied to the characteristics of the scintillators and photodetectors required to fulfill them.

In **chapter 2**, the main techniques for growing $\text{LaBr}_3\text{:Ce}$, CeBr_3 and $\text{LuI}_3\text{:Ce}$ as well as Ce^{3+} doped elpasolite and Eu^{2+} doped alkaline earth halide crystals are discussed. An overview of methods used to measure scintillation performance of these compositions is also provided.

In **chapter 3**, the scintillation properties of $\text{LaBr}_3\text{:Ce}$ are covered with particular emphasis on the improvement in the timing response of $\text{LaBr}_3\text{:Ce}$ as the Ce^{3+} doping level is increased from 0.5% to 30% (on molar basis). It is interesting to note that this improvement in timing occurs without any significant degradation in the light output. This is particularly relevant for applications that demand high timing resolution (such as PET). A brief discussion of on-going efforts to use $\text{LaBr}_3\text{:Ce}$ in time-of-flight PET imaging is presented.

In **chapter 4**, the scintillation properties of CeBr_3 are discussed. In many ways, the scintillation properties of CeBr_3 are similar those for LaBr_3 with high Ce^{3+} content. The proportionality of response while being high for CeBr_3 is not as high as $\text{LaBr}_3\text{:Ce}$ so far. Due to its fast response, excellent timing resolution has been achieved with CeBr_3 , making it a viable alternative to LaBr_3 (with high Ce content) in TOF-PET. Due to lack of any self-activity in CeBr_3 , it can be a useful scintillator in applications demanding high energy resolution with very

low intrinsic background. In such applications, the self activity of $\text{LaBr}_3\text{:Ce}$ (due to ^{133}La) can be a problem.

In **chapter 5**, the scintillation characteristics of $\text{LuI}_3\text{:Ce}$ are discussed. In terms of physical and scintillation properties, $\text{LuI}_3\text{:Ce}$ appears to be a very exciting scintillator for PET. It combines high gamma-ray stopping power with exceptionally high light output and fast response. The effect of Ce^{3+} doping level on the scintillation properties of LuI_3 is discussed and optimal Ce^{3+} doping level is identified. The main challenge in the advancement of this scintillator for PET (and other gamma-ray spectroscopy applications) is in growth of large volume crystals with high optical quality, where the layered rhombohedral crystal structure of LuI_3 is a disadvantage. Alternative PET module designs that utilize thin layers of scintillators with photodiode readout can be considered until high quality, large volume single crystals become available.

In **chapter 6**, a discussion of new Ce^{3+} elpasolite and Eu^{2+} alkaline earth scintillators is provided. Due to their relatively low density and/or slow response, both these classes of scintillators are not appropriate for PET imaging. However, their gamma-ray stopping efficiency and speed are adequate for SPECT imaging. Very high proportionality demonstrated by both these scintillator classes over a broad energy range and their high light output make these scintillators very attractive for SPECT. In fact, over typical energy range used in SPECT (such as 140 keV gamma-rays emitted $^{99\text{m}}\text{Tc}$), the energy resolution of selected compositions in both these classes is superior to that for even $\text{LaBr}_3\text{:Ce}$.

In **chapter 7 & 8**, properties and performance of silicon avalanche photodiodes (operating in proportional mode) are discussed. Particular attention is given to a position sensitive APD design where by depositing four corner contacts on a resistive layer on the back face, event location can be deduced by comparing the signals collected at the four corner electrodes. Such a device provides position information due to charge sharing and requires only four contacts to image very large areas (such as $8 \times 8 \text{ mm}^2$ and $14 \times 14 \text{ mm}^2$) while successfully resolving $\leq 1 \text{ mm}$ LYSO scintillation elements. Evaluation results for PET modules designs based on such PSAPDs for small animal PET imaging with DOI encoding capability are presented. A brief discussion of some new small animal PET systems for simultaneous PET-MR imaging as well as ultra-high resolution PET imaging with DOI encoding is presented.

In **chapter 9**, properties and performance of silicon photomultipliers built using standard CMOS process, which are referred to as solid-state photomultipliers (SSPMs) are discussed. Fundamental characteristics such as gain, dark count-rate and speed of response for these devices are discussed. Basic evaluation results of energy and timing resolution of the SSPMs coupled to LYSO crystals are presented. Very high timing resolution (in sub-ns range) of SSPMs makes them a viable candidate for TOF-PET systems. Position sensitive SSPM designs based on charge sharing between separate SSPM elements as well as between micro-pixels within a single SSPM are discussed. Successful imaging results of high-resolution LYSO arrays using such PS-SSPMs are presented. DOI encoding studies using SSPMs as well as PS-SSPMs are also presented. Based on their overall performance, the SSPM technology appears to be well suited for high resolution, small volume PET with DOI encoding as well as for future time-of-flight PET systems.

Table 1. Summary of Scintillation Properties

Crystal	Light Yield photons/MeV	Emission nm	Principal Decay Time, ns
LaBr ₃ :0.5%Ce	70,100	360	26
LaBr ₃ :5% Ce	70,500	360	16
LaBr ₃ :10% Ce	64,500	360	16
LaBr ₃ :20% Ce	64,000	360	17
LaBr ₃ :30%Ce	69,000	360	18.6
CeI ₃	≤5,000	514	-
CeBr _{1.5} Cl _{1.5}	65,000	370	17
CeBr ₃	68,000	370	17
CeCl ₃	45,500	355	23
LuI ₃ :0.5%Ce	≥100,000	475	40
LuI ₃ :2%Ce	≥100,000	475	30
LuI ₃ :5%Ce	≥100,000	475	25
LuI ₃ :10%Ce	70,000	475	28
LuI ₃ :10%Ce	38,000	525	30
Cs ₂ NaLaI ₆ :Ce	54,000-60,000	455	50
Cs ₂ LiLaI ₆ :Ce	≥55,000	450	50
Cs ₂ NaLaBr ₆ :Ce	12,000	400	55
Cs ₂ LiLaBr ₆	35,500	390, 420	2300
Cs ₂ LiLaBr ₆ :0.5%Ce	56,200	390, 420	55, ≥270
Cs ₂ LiLaBr ₆ :2%Ce	60,000	390, 420	55, ≥270
Cs ₂ LiLaBr ₆ :5%Ce	50,000	420	55, ≥270
Cs ₂ LiLaBr ₆ :10%Ce	55,000	420	55, ≥270
Cs ₂ LiLaCl ₆ :Ce	36,000	390	90
Cs ₂ NaCeBr ₆	32,000	415	115
Cs ₂ NaGdI ₆ :Ce	21,000	445	55
Cs ₂ NaLuI ₆ :Ce	27,000	450	35
Cs ₂ LiLuI ₆ :Ce	12,000	490	45
Cs ₂ LiYCl ₆ :Ce	20,000	370	37
SrI ₂ :0.5%Eu	78,000	429	620
SrI ₂ :2%Eu	92,000	431	900
SrI ₂ :5%Eu	100,000	433	1100
SrI ₂ :10%Eu	84,000	436	1650
BaI ₂ :0.5%Eu	26,000	430	450
CaI ₂ :0.5%Eu	>100,000	470	1150
SrBr ₂ :0.5%Eu	26,000	415	720
BaBr ₂ :0.5%Eu	11,500	410	560
Ba _x Sr _{1-x} I ₂ :Eu	~100,000	435	>1000

Table 2 Comparison of Photodetectors

Device	Gain	Excess Noise Factor (ENF)	QE (> 400 nm)	Voltage	Rise time	Magnetic sensitivity
SSPM	$\sim 10^6$	~ 1.3	$\sim 20\%^*$	$\sim 30\text{ V}$	$\sim 0.5\text{ ns}$	No
Si APD	$\sim 10^3$	~ 2	$\sim 80\%$	$> 1\text{ KV}$	1-2 ns	No
PMT	$\sim 10^6$	~ 1.2	$> 30\%^{**}$	$> 1\text{ KV}$	$\sim 0.1\text{ ns}$	Yes

*This value is the 'photon detection efficiency (= geometric efficiency•Geiger probability•quantum efficiency)

**This QE is for super bi-alkali photocathode, higher QE (>40%) has been reported with ultra-bi-alkali photocathode

HOOFDSTUK 11: SAMENVATTING

De focus van dit proefschrift ligt op nieuwe detectietechnologieën die gebruikt kunnen worden bij de verbetering van nucleaire geneeskundige modaliteiten, met name positron emissie tomografie (*PET*). Verschillende detectietechnologieën worden in dit proefschrift besproken. In de eerste plaats worden nieuwe Ce^{3+} gedoopte zeldzame-aard trihalogenide scintillatoren besproken die gebruikt kunnen worden in *PET*. In het bijzonder wordt aandacht besteed aan de hoge lichtopbrengst en de hoge lineariteit om een hoge energieresolutie te bereiken, en aan een snelle respons voor hoge *timing* resolutie, tezamen met de mogelijkheid van het uitvoeren van *time-of-flight* (*TOF*) datacollectie (ter vermindering van het aantal toevallige coïncidenties en van de ruis in het gereconstrueerde beeld). In aanvulling op de bespreking van nieuwe scintillatoren voor gebruik in *PET*, komen twee typen nieuwe scintillatoren (Ce^{3+} gedoopte elpasoliten en Eu^{2+} gedoopte aardalkali halogeniden) aan bod die een hoge lineariteit als wel energieresolutie over een breed spectrum van energieën hebben voor gebruik in *single photon emission computed tomography* (*SPECT*). De belangrijkste kenmerken zoals scintillatielichtopbrengst, de piekmissiegolflengte en de vervalstijdsconstante van alle scintillatoren besproken in dit proefschrift zijn samengevat in **Tabel 1**.

Naast nieuwe scintillatoren komen ook twee vaste-stof fotodetectietechnologieën aan bod in dit proefschrift. Deze omvatten *silicon avalanche photodiodes* (*APDs*) en vaste-stof fotomultiplicatorbuizen (*PMTs*) gebaseerd op silicium (*SSPMs*). Zowel standaard als positie gevoelige versies van deze fotodetectoren worden besproken, in het bijzonder met betrekking tot het gebruik van deze nieuwe sensoren in klein-volume *PET*. Ook worden ontwerpen van *PET*-modules besproken met het vermogen *depth-of-interaction* (in de scintillator elementen - *DOI*) te bepalen teneinde parallaxfouten in de beeldreconstructie te voorkomen. Een vergelijking van enkele van de belangrijkste parameters van *APDs*, *SSPMs* en *PMTs* is gegeven in **Tabel 2**.

In **hoofdstuk 1** van dit proefschrift worden de opkomende behoeften in nucleaire geneeskundige modaliteiten, zoals hoge energie resolutie voor *PET* en *SPECT*, hoge *timing* resolutie (met inbegrip van *TOF*) en *DOI*-codering voor *PET*, besproken. Deze behoeften worden gekoppeld aan de kenmerken van scintillatoren en fotodetectoren die nodig zijn om hieraan te voldoen.

In **hoofdstuk 2** worden de belangrijkste technieken voor de kristalgroei van $\text{LaBr}_3\text{:Ce}$, CeBr_3 en $\text{LuI}_3\text{:Ce}$ alsmede Ce^{3+} gedoopte elpasoliten en Eu^{2+} gedoopte aardalkali halogenide kristallen besproken. Een overzicht van de gebruikte methoden om de scintillatie prestaties te meten wordt ook gegeven.

In **hoofdstuk 3** worden de scintillatieeigenschappen van $\text{LaBr}_3\text{:Ce}$ besproken, met bijzondere nadruk op de verbetering van de *timing* eigenschappen van $\text{LaBr}_3\text{:Ce}$ als de Ce^{3+} concentratie wordt opgevoerd van 0,5% tot 30% (op molaire basis). Het is interessant om op te merken dat de verbetering in *timing* plaatsvindt zonder significante achteruitgang in de lichtopbrengst. Dit is met name relevant voor toepassingen die een hoge *timing* resolutie vereisen (zoals *PET*). Een korte bespreking van lopend onderzoek naar het gebruik van $\text{LaBr}_3\text{:Ce}$ in *time-of-flight* *PET* wordt gepresenteerd.

In **hoofdstuk 4** worden de scintillatieeigenschappen van CeBr_3 besproken. In veel opzichten zijn de scintillatieeigenschappen van CeBr_3 vergelijkbaar met die van LaBr_3 met een hoge Ce^{3+} concentratie. De proportionaliteit, alhoewel lineair voor CeBr_3 , is niet zo goed als die voor $\text{LaBr}_3\text{:Ce}$ (tot nu toe). Echter, door de snelle respons wordt een uitstekende *timing resolutie* bereikt, waardoor CeBr_3 een goed alternatief voor LaBr_3 (met een hoog gehalte aan Ce) in *TOF-PET* is. Wegens afwezigheid van intrinsieke radioactiviteit in CeBr_3 kan het een nuttige

scintillator zijn in toepassingen die een hoge energieresolutie vereisen met een zeer lage intrinsieke achtergrond. In dergelijke toepassingen kan de intrinsieke activiteit van $\text{LaBr}_3\text{:Ce}$ (als gevolg van ^{133}La) een probleem zijn.

In **hoofdstuk 5** worden de scintillatieeigenschappen van $\text{LuI}_3\text{:Ce}$ besproken. In termen van fysieke eigenschappen en scintillatie lijkt $\text{LuI}_3\text{:Ce}$ een veelbelovende scintillator voor PET te zijn. Zij combineert een hoge *gamma-ray stopping power* met een uitzonderlijk hoge lichtopbrengst en een snelle respons. Het effect van de Ce^{3+} concentratie op de scintillatie eigenschappen van LuI_3 wordt besproken, en de optimale Ce^{3+} concentratie vastgesteld. De belangrijkste uitdaging in de vooruitgang van deze scintillator voor PET (en andere *gamma-ray* spectroscopietoepassingen) is de groei van grote kristallen met een hoge optische kwaliteit. Hierbij is de gelaagde rhombohedrische kristalstructuur van LuI_3 een nadeel. Alternatieve PET-module ontwerpen die gebruik maken van dunne lagen van scintillatoren met fotodiode uitlezing zouden kunnen worden gebruikt totdat grote kristallen beschikbaar komen.

In **hoofdstuk 6** wordt een discussie gevoerd met betrekking tot nieuwe Ce^{3+} elpasoliten en Eu^{2+} aardalkali scintillatoren. Door hun relatief lage dichtheid en / of trage scintillatie zijn beide type scintillatoren niet geschikt voor PET. Echter, hun *gamma-ray stopping efficiëntie* en snelheid zijn geschikt voor SPECT. De zeer hoge lineariteit over een groot energiebereik van beide typen scintillatoren en hun hoge lichtopbrengst maken dat deze scintillatoren zeer aantrekkelijk zijn voor gebruik in SPECT. Gezien de energieën die gebruikt worden in SPECT (zoals 140 keV gammastralen van $^{99\text{m}}\text{Tc}$), is de energieresolutie van beide typen scintillatoren zelfs superieur aan die van $\text{LaBr}_3\text{:Ce}$.

In **hoofdstuk 7 & 8** worden de eigenschappen en prestaties van *silicon avalanche photodiodes (APDs)* besproken. Bijzondere aandacht wordt gegeven aan positiegevoelige APD ontwerpen waarbij, door het maken van vier hoek-contacten op een resistieve laag op de achterkant van de APD, de locatie van een interactie kan worden afgeleid door het vergelijken van de signalen van elke van de vier hoek-contacten. Een dergelijk ontwerp biedt informatie over de positie ten gevolge van het delen van lading, en vereist slechts vier contacten om afbeeldingen over zeer grote gebieden (zoals $8 \times 8 \text{ mm}^2$ en $14 \times 14 \text{ mm}^2$) te verkrijgen. Tergelijkertijd kan een resolutie van $\leq 1 \text{ mm}$ met LYSO scintillatie elementen worden bereikt. Een evaluatie van de resultaten van PET-module ontwerpen op basis van dergelijke PSAPDs voor *small-animal* PET systemen met DOI-codering wordt gepresenteerd. Een korte bespreking van enkele *small-animal* PET systemen voor PET-MRI als ultra-hoge resolutie PET beeldvorming met DOI codering wordt gepresenteerd.

In **hoofdstuk 9** worden de eigenschappen en prestaties van silicium fotomultiplicatorbuizen, gebouwd met behulp van een standaard CMOS-proces (aangeduid als vaste-stof fotomultiplicatie buizen, *SSPMs*), besproken. Fundamentele kenmerken zoals versterking, ruis en snelheid van deze sensoren worden besproken. Een evaluatie van de resultaten van de energie- en de *timing* resolutie van de SSPMs gekoppeld aan LYSO kristallen wordt gepresenteerd. De zeer hoge *timing* resolutie (in sub-ns bereik) van de SSPMs maakt hen goede kandidaten voor TOF-PET-systemen. Positiegevoelige SSPM ontwerpen gebaseerd op ladingsdeling tussen de afzonderlijke SSPM elementen alswel tussen micro-pixels binnen een SSPM worden besproken. De succesvolle resultaten van beeldvorming met hoge-resolutie LYSO blokken in combinatie met PS-SSPMs worden gepresenteerd. DOI codering studies met behulp van SSPMs en PS-SSPMs worden ook gepresenteerd. Op basis van hun algemene prestaties lijkt de SSPM technologie goed geschikt voor hoge resolutie, klein-volume PET met DOI-codering alsmede voor toekomstige *time-of-flight* PET-systemen.

Tabel 1. Samenvatting van scintillatieeigenschappen

Kristal	Lichtopbrengst fotonen/MeV	Emissie golflengte nm	Vervalsconstante ns
LaBr ₃ :0.5%Ce	70,100	360	26
LaBr ₃ :5% Ce	70,500	360	16
LaBr ₃ :10% Ce	64,500	360	16
LaBr ₃ :20% Ce	64,000	360	17
LaBr ₃ :30%Ce	69,000	360	18.6
CeI ₃	≤5,000	514	-
CeBr _{1.5} Cl _{1.5}	65,000	370	17
CeBr ₃	68,000	370	17
CeCl ₃	45,500	355	23
LuI ₃ :0.5%Ce	≥100,000	475	40
LuI ₃ :2%Ce	≥100,000	475	30
LuI ₃ :5%Ce	≥100,000	475	25
LuI ₃ :10%Ce	70,000	475	28
LuI ₃ :10%Ce	38,000	525	30
Cs ₂ NaLaI ₆ :Ce	54,000-60,000	455	50
Cs ₂ LiLaI ₆ :Ce	≥55,000	450	50
Cs ₂ NaLaBr ₆ :Ce	12,000	400	55
Cs ₂ LiLaBr ₆	35,500	390, 420	2300
Cs ₂ LiLaBr ₆ :0.5%Ce	56,200	390, 420	55, ≥270
Cs ₂ LiLaBr ₆ :2%Ce	60,000	390, 420	55, ≥270
Cs ₂ LiLaBr ₆ :5%Ce	50,000	420	55, ≥270
Cs ₂ LiLaBr ₆ :10%Ce	55,000	420	55, ≥270
Cs ₂ LiLaCl ₆ :Ce	36,000	390	90
Cs ₂ NaCeBr ₆	32,000	415	115
Cs ₂ NaGdI ₆ :Ce	21,000	445	55
Cs ₂ NaLuI ₆ :Ce	27,000	450	35
Cs ₂ LiLuI ₆ :Ce	12,000	490	45
Cs ₂ LiYCl ₆ :Ce	20,000	370	37
SrI ₂ :0.5%Eu	78,000	429	620
SrI ₂ :2%Eu	92,000	431	900
SrI ₂ :5%Eu	100,000	433	1100
SrI ₂ :10%Eu	84,000	436	1650
BaI ₂ :0.5%Eu	26,000	430	450
CaI ₂ :0.5%Eu	>100,000	470	1150
SrBr ₂ :0.5%Eu	26,000	415	720
BaBr ₂ :0.5%Eu	11,500	410	560
Ba _x Sr _{1-x} I ₂ :Eu	~100,000	435	>1000

Tabel 2. Vergelijking van Fotodetectoren

Apparaat	Verster- king	Excess Ruisfactor (ENF)	QE (> 400 nm)	Voltage	Stijgtijd	Magnetische gevoeligheid
SSPM	$\sim 10^6$	~ 1.3	$\sim 20\%^*$	$\sim 30\text{ V}$	$\sim 0.5\text{ ns}$	No
Si APD	$\sim 10^3$	~ 2	$\sim 80\%$	$> 1\text{ KV}$	1-2 ns	No
PMT	$\sim 10^6$	~ 1.2	$> 30\%^{**}$	$> 1\text{ KV}$	$\sim 0.1\text{ ns}$	Yes

*Deze waarde is de fotondetectie-efficiëntie (= geometrische efficiëntie Geiger probability quantum efficiëntie)

**Deze QE is voor de super-bialkalifotokathodes, een hogere QE (> 40%) wordt verkregen met ultra-bialkalifotokathodes

ACKNOWLEDGEMENTS

I am very grateful for the support provided by all my friends and colleagues at Radiation Monitoring Devices (RMD), Inc., in this endeavor. Contributions of V. Biteman, J. Christian, L. Cirignano, P. Dokhale, R. Farrell, J. Glodo, R. Grazioso, R. Hawrami, W. Higgins, C. Hines, M. Klugerman, M. McClish, U. Shirwadkar, C. Stapels, J. Vagini, and E. van Loef, all at RMD, have directly impacted this research. The environment of openness and flexibility created at RMD by Dr. Gerald Entine, Dr. Michael Squillante and Joanne Gladstone has made this project possible and I appreciate their encouragement on this effort. I would like to thank Mr. Martin Waters at RMD for providing help in the format of this document.

Contributions of my various research collaborators have been vital in this project. This includes the teams of Dr. Simon Cherry at University of California, Davis; Dr. Bruce Hasegawa at the University of California, San Francisco; Dr. Joel Karp at the University of Pennsylvania; Dr. William Moses at the Lawrence Berkeley National Laboratory; and Dr. Stephen Payne at the Lawrence Livermore National Laboratory.

Funding provided by the US federal agencies, particularly the Department of Homeland Security (Dr. Alan Janos and Dr. Mark Wrobel), Department of Energy (Dr. David Beach, Dr. Peter Vanier, Dr. Manouchehr Farkhondeh and Dr. Prem Srivastava), Dr., Department of Defense (Maj. Brad Beaty, Dr. James Howell and Dr. Elizabeth Bartosz) and the National Institute of Health (Dr. Houston Baker) has made this research possible, so I gratefully acknowledge their support.

My thesis advisors at TU Delft, Dr. Carel van Eijk and Dr. Pieter Dorenbos, have provided the guidance and support to get this project completed. Their insightful comments on the early drafts have been educational and have led to considerable improvement in the quality of the final version. I also appreciate their patient and encouraging attitude when the progress was slow. Ms. Jose Buurman at TU Delft's Radiation Detection and Medical Imaging division has also provided support in getting this manuscript printed as well as in shepherding me through other aspects of the thesis defense.

The affection of my parents, my sister (Aditi Nanavati) and my brother (Utpal Shah) as well as the extended family and friends scattered all over the world is a blessing that has allowed me to undertake adventures such as this project.

Finally, the love and encouragement of my wife, Sheela Shodhan-Shah, have been a major source of inspiration for me and I thank her for all things large and small. Regarding my children, my daughter (Ananya Shah) and my son (Ishaan Shah), their smiles make everything worthwhile.

CURRICULUM VITAE

Kanai S. Shah was born in Ahmedabad (India) on September 02, 1961. He graduated from the Gujarat Law Society High School in 1979. Mr. Shah obtained his undergraduate training in Chemical Engineering at the Gujarat University in India, graduating with a B.E. in 1983. He then proceeded to obtain his M.S. degree in Chemical Engineering at the University of Lowell in Massachusetts in 1987. His master's thesis was a study of mass transfer of carbon dioxide through catheters used in implantable drug delivery systems.

Mr. Shah joined Radiation Monitoring Devices in 1985 as a Staff Scientist and was initially involved in investigation of low energy X-ray detectors based on HgI₂ semiconductors. Subsequently he managed a variety of compound semiconductor detector development and device characterization efforts. The semiconductor materials he has investigated in past include PbI₂, HgI₂, TlBr, TlBr_xI_{1-x}, ZnTe, CdTe, CdZnTe, InI, and BP. From 5/92 to 10/93, Mr. Shah worked as a Device Engineer at Canberra Industries, Meriden, CT. At Canberra, he was involved in investigation of high-purity germanium gamma-ray detectors and high resolution, low noise silicon X-ray detectors.

Mr. Shah rejoining Radiation Monitoring Devices in 11/93 as a Senior Scientist. He became the Director of Research at Radiation Monitoring Devices in 10/02. Recently, in 10/09 he became a Vice President (R&D) of Radiation Monitoring Devices. He has been in charge of new semiconductor and scintillator development at RMD for over ten years. His areas of research interest include development of new detector materials and investigation of high-resolution neutron, X-ray and gamma ray detectors with imaging capabilities. Mr. Shah is a member of IEEE. Mr. Shah has made several invited presentations at international conferences, reviewed papers for IEEE and MRS journals, is a site reviewer for the Department of Energy programs, and authored over 70 technical papers. He has been awarded five U.S. patents. Mr. Shah enrolled at TU Delft as a Ph.D. candidate in August, 2006. His doctoral research has focused on investigation of new scintillator and photodetection technologies for use in medical imaging, particularly positron emission tomography.

Publications & Presentations

Book Chapters:

- Squillante, M.R. and Shah, K.S., "Chapter 12: Other Materials: Status and Prospects," in Semiconductors for Room Temperature Nuclear Detector Applications, eds. T.E. Schlesinger & R.B. James, Academic Press, 1995.
- Squillante, M.R., and Shah, K.S., "Chapter VIII, Sect. 8.1.3: Photojunction Sensors," in The Measurement, Instrumentation and Sensors Handbook, ed. J.G. Webster, CRC Press, Boca Raton, FL., 1998.

SELECTED RECENT PUBLICATIONS

- M. McClish, P. Dokhale, J. Christian, E. Johnson, C. Stapels, R. Robertson, K. S. Shah, Characterization of CMOS Position Sensitive Solid-State Photomultipliers, accepted for publication in NIMA, (2010)

- M. McClish, R. Farrell, J. Glodo, K.S. Shah, "A study of low resistivity, deep diffused, silicon avalanche photodiodes coupled to $\text{LaBr}_3\text{:Ce}$ scintillator," pp. 207-209, NIMA 610 (2009).
- S. St James, Y. Yang, Y. Wu, R. Farrell, P. Dokhale, K. S. Shah and S. R Cherry, Experimental characterization and system simulations of depth of interaction PET detectors using 0.5 mm and 0.7 mm LSO arrays, *Phys. Med. Biol.* 54 4605-4619, (2009).
- E.V.D. van Loef, C.M. Wilson N.J. Cherepy, G. Hull, S.A. Payne, W- S. Choong, W.W. Moses, K.S. Shah, "Crystal Growth and Scintillation Properties of Strontium Iodide Scintillators", *IEEE Trans. Nucl. Sci.*, vol. 56, 869-72 (2009).
- E.V. van Loef, W.M. Higgins, J. Glodo, A.V. Churilov, K.S. Shah, "Crystal growth and characterization of rare earth iodides for scintillation detection", *Journal of Crystal Growth*, Vol. 310, No. 1, pp. 2090-2093 (2008).
- N.J. Cherepy, G. Hull, A. Drobshoff, S.A. Payne, E. van Loef, C. Wilson, K. Shah, U.N. Roy, A. Burger, L.A. Boatner, W-S Choong, W.W. Moses "Strontium and Barium Iodide High Light Yield Scintillators," *Appl. Phys. Lett.* vol. 92, p. 083508, (2008).
- W.M. Higgins, J. Glodo, E. Van Loef, M. Klugerman, T. Gupta, L. Cirignano, P. Wong, K.S. Shah, "Bridgman growth of $\text{LaBr}_3\text{:Ce}$ and $\text{LaCl}_3\text{:Ce}$ crystals for high-resolution gamma-ray spectrometers", *Journal of Crystal Growth* 287, pp. 239-242, (2006).
- K.S. Shah, Glodo J, W. W. Moses, *et al.* " CeBr_3 scintillators for gamma-ray spectroscopy," *IEEE TNS.* 52: pp. 3157–3159, (2005).
- K.S. Shah, J. Glodo, M. Klugerman, W. Higgins, P. Wong, W.W. Moses, S.E. Derenzo, M. Weber, and P. Dorenbos, " $\text{LuI}_3\text{:Ce}$ – A New Scintillator for Gamma Ray Spectroscopy", *IEEE Trans. Nuc. Sci.*, V(51), p. 2302, (2004).
- K. Shah, R. Grazioso, R. Farrell, J. Glodo, M. McClish, G. Entine, P. Dokhale, and S. R. Cherry, "Position Sensitive APD's for Small Animal PET Imaging," *IEEE Trans. Nucl. Sci.*, vol. 51, no. 1, p. 91, (2004).
- K.S. Shah, J. Glodo, W.W. Moses, S.E. Derenzo, M.J. Weber, " $\text{LaBr}_3\text{:Ce}$ Scintillators for γ -Ray Spectroscopy," *IEEE Trans. Nuc. Sci.*, V50(6), p. 2410, (2003).
- K. S. Shah, R. Farrell, R. Grazioso, E. S. Harmon, E. Karplus, *Position-sensitive avalanche photodiodes for gamma-ray imaging*, *IEEE Trans. Nucl. Sci.*, vol. 49, no. 4, p. 1687, (2002).
- K. S. Shah, R. Farrell, R. Grazioso, R. Myers, and L. Cirignano, *Large-area APDs and monolithic APD Arrays*, *IEEE Transactions on Nuclear Science*, vol. 48, p. 2352, (2001).

RECENT PRESENTATIONS

- K.S. Shah, *et. al.*, High Sensitivity, High Resolution Radioisotopic Detection, Invited Presentation at DND-NSF's 3rd Annual Academic Research Initiative Conference, Washington DC, April (2010).
- K.S. Shah, *et. al.*, Overview of CLYC Scintillators, Invited Presentation at DND-NSF's 3rd Annual Academic Research Initiative Conference, Washington DC, April (2010).
- K.S. Shah, *et. al.*, Advances in Thallium Bromide Gamma-Ray Spectrometer Development, Invited Presentation at SPIE Annual Meeting, San Diego, August (2009)
- K.S. Shah, *et. al.*, New Scintillators for SPECT, SPIE Annual Meeting, San Diego, August (2009)
- K.S. Shah, Solid State Photomultipliers, Presentation at DOD-DTRA Technical Review Workshop, Washington DC, December (2008).

K.S. Shah, Advances in Photodetectors for Nuclear Medicine Applications, Invited Review Lecture, IEEE NSS/MIC, Honolulu, Oct. (2007).

K.S. Shah, *et. al.*, Search of Cerium Activated Scintillators based on Rare Earth Trihalide Compositions, Invited Presentation at IEEE NSS, Honolulu, Oct. (2007).

PATENTS

K.S. Shah, W. Higgins, E.V. van Loef, J. Glodo, Cesium and lithium-containing quaternary compound scintillators, U.S. Patent # 7,655,919 (2010)

K.S. Shah, *et. al.*, Position Sensitive Solid-State Photomultipliers, Systems and Methods, U.S. Provisional Appl. No. 61/185,169, June (2009)

K.S. Shah, CeBr₃ Scintillator, U.S. Patent # 7,405,404 (2008)

K.S. Shah, Lu_{1-x}I₃:Ce_x - a scintillator for gamma ray spectroscopy and time-of-flight PET, U.S. Patent # 7,173,247, (2007).

K.S. Shah, Very fast doped LaBr₃ scintillators and time-of-flight PET, U.S. Patent # 7,129,494, 2006

E.Karplus, R.Farrell, K.S.Shah, "Position Sensitive Solid State Detector with Internal Gain," U.S. Patent # 6,998,619, Feb. 14, 2006

